The Large-scale Structure of the Universe: Probes of Cosmology and Structure Formation

By

Yookyung Noh

A dissertation submitted in partial satisfaction of the

requirements for the degree of

Doctor of Philosophy

in

Astrophysics

in the

Graduate Division

of the

University of California, Berkeley

Committee in charge:
Professor Martin White, Co-chair
Professor Eliot Quataert, Co-chair
Doctor Joanne D. Cohn
Professor Daniel Kasen
Professor Adrian T. Lee

Fall 2013

The Large-scale Structure of the Universe: Probes of Cosmology and Structure Formation

Abstract

The Large-scale Structure of the Universe: Probes of Cosmology and Structure Formation

by

Yookyung Noh

Doctor of Philosophy in Astrophysics

University of California, Berkeley

Professor Martin White, Co-chair
Professor Eliot Quataert, Co-chair

The usefulness of large-scale structure as a probe of cosmology and structure formation is increasing as large deep surveys in multi-wavelength bands are becoming possible. The observational analysis of large-scale structure guided by large volume numerical simulations are beginning to offer us complementary information and crosschecks of cosmological parameters estimated from the anisotropies in Cosmic Microwave Background (CMB) radiation. Understanding structure formation and evolution and even galaxy formation history is also being aided by observations of different redshift snapshots of the Universe, using various tracers of large-scale structure.

This dissertation work covers aspects of large-scale structure from the baryon acoustic oscillation scale, to that of large scale filaments and galaxy clusters. First, I discuss a large-scale structure use for high precision cosmology. I investigate the reconstruction of Baryon Acoustic Oscillation (BAO) peak within the context of Lagrangian perturbation theory, testing its validity in a large suite of cosmological volume N-body simulations. Then I consider galaxy clusters and the large scale filaments surrounding them in a high resolution N-body simulation. I investigate the geometrical properties of galaxy cluster neighborhoods, focusing on the filaments connected to clusters. Using mock observations of galaxy clusters, I explore the the correlations of scatter in galaxy cluster mass estimates from multi-wavelength observations and different measurement techniques. I also examine the sources of the correlated scatter by considering the intrinsic and environmental properties of clusters.

On ne voit bien qu'avec le cœur. L'essentiel est invisible pour les yeux.
–Antoine de Saint-Exuèpry, Le Petit Prince

For my parents

Contents

List of Figures

List of Tables

Acknowledgments

This dissertation means to me more than an academic achievement. Moving away from my family and home country, and living alone in a different cultural environment and a strange place to pursue my graduate study have put me in many difficult situations. The challenging years made me more mature and open another page of my life. It also led me to become more appreciative of the people who support and help me.

First, I owe my deepest gratitude to my advisor, Joanne Cohn, for working with me, giving me interesting projects and guiding me to finish them. She inspired me with her infinite energy in research and constant humbleness to learn. Her emotional support at every difficult moment – the beginning of the work with her when I was completely overwhelmed and about to quit graduate school, the days before my prelim and my qualification exams and the time of writing this thesis – was also invaluable.

I sincerely thank Matthew McQuinn, who showed his endless patience for my unintentional slow progress and who was always willing to help resolving both scientific questions and personal issues. I consider it was one of my best in Berkeley to have him as my close collaborator. I am incredibly grateful to my class shepherd advisor, Eugene Chiang, for his wise advice and honest feedback whenever I experienced difficulty. It was also helpful to work as a graduate student instructor for him because of his inspiring lectures and attitude to the students. I also would like to thank my previous advisor, Martin White, for sharing his knowledge and scientific insight with me and providing numerical simulations that were essential to my projects. I thank Nikhil Padmanabhan for his collaboration and contribution to this dissertation. My gratitude also goes to my previous advisor in Korea, Jounghun Lee, for encouraging and believing in me more than I did. I would like to acknowledge my dissertation committee members, Martin White, Eliot Quataert, Daniel Kasen and Adrian Lee for their participations.

I am indebted to Reiko Nakajima and Hee-Jong Seo whose friendship and mentorship have meant a lot to me. Working together and reading and discussing papers with them helped me grow as a cosmologist. We also shared a lot of enjoyable time and supported each other. Without them, I would have been much lonelier. I want to deeply thank Dexter Stewart, without whom all of my non-academic issues would not have been resolved. She was always friendly and kindly helped me favors even with my last minute requests.

I would like to thank you all of my fellow graduate students in the Astronomy department for their support and companionship. Further thanks to the friends of the cosmology reading

group of many different acronyms, particularly, Eric Huff, Andrew Wetzel, Reiko Nakajima, and Matt George for their insightful thoughts and ideas and strong supports. I want to deeply thank my wonderful officemates, Amber Bauermeister, Statia Luzscz-Cook and Sarah Newman, who enriched my life in Berkeley. We made trips to local restaurants, went to walk-in classes in RSF, hiked trails and celebrated eventful moments together. Without them, I would not have felt that I was a part of this society. My sincere thanks to Chris Klein, Charles Hansen, Becky Milczarek, Mai Truong, Victoria Martin for the enjoyable conversations and activities and the amazing friendships; thank you, Chris, for bringing my books and papers for me to Portland. I want to thank my mentor and mentor masters, Katie Peek, Linda Strubbe, Kristen Shapiro and Holly Maness for helping me adjusting into the department; my special thanks to Linda for her warmth and advice. I was also humbled by many of fellows whom I met on the journeys outside the department and who helped me view my life and my research in many different ways despite the short encounters.

I want to express my gratitude to my all Korean friends I made in Berkeley for making me feel as if I were living in my home country. Special thanks to Youjeong and her husband, Ji-hoon, for listening to me and taking care of me. It was truly fortunate to happen to share an apartment with her during my first year, and becoming her friend. Many thanks to Soo Mi for giving me endless encouragement, to Geena for empathic conversations, to Hyojin for bringing humor into my life, and to Kyunglim for spending many evenings studying together. I thank, my *Na-ee-tae* family – Grace, Yoonseong, Youngwook, Jung Yeon and Seung Min – for your friendship and unforgettable memories. I feel blessed to have you in my life.

I also thank my friends who have loved me and maintained our friendship no matter how far we are apart. To Eunyoung for calling me and listening to me as if we were together in person. To Soo Hyun for her touching postcards and considerate packages, which made me feel loved. To Hyo Jeong for understanding me more than anyone else – you know that I consider you as my big sister. To Moontae, Seul Gi, Jin-Hee and Ji-hoon who lived close by and let me visit whenever I wanted to have a carefree conversation in person.

Finally, my heartfelt thanks to my family. I deeply appreciate my parents-in-law for their support. My sincere thanks expand to my only sister, Sun Kyung, for her empathy and for being always on my side. She has been a special companion and a reliable friend throughout my life. I am also grateful to my sister's family – my beloved niece, Jisu, who always makes me smile and lifts my spirit, and my brother-in-law, Hosung, who was always generous and kind. I thank my husband, Seungmin, for his intellectual companionship and patience. I look forward to our future together, when we do not have to live far apart and make regular long trips to visit each other. Lastly and the most importantly, I thank my Mom and Dad for raising me to be who I am today, praying for me, giving me endless support and having confidence in me. No words can express enough how much I thank and love them. It is them who made this accomplishment possible. This thesis is dedicated to them.

This dissertation was typeset using the ucastrothesis LaTeX template.

Chapter 1

Introduction

In the past few decades, large surveys have revealed that galaxies are coherently distributed, forming structures on large scales. A recent observation by the Sloan Digital Sky Survey is shown in the left panel in fig. 1.1, as an example. This large scale structure gravitationally grew from primordial fluctuations in the matter density. As the matter density is mostly cold dark matter (CDM), which is non-relativistic and collisionless, structure formation is hierarchical. First overdensities on small scales collapse to form halos. Large halos form later via mergers or accretion. Measuring, characterizing and predicting the properties of large scale structure and its evolution in detail are of great interest but hard because gravity is non-linear. Large scale structure also provides information about the background cosmology within which it grows, motivating studies of Baryon Acoustic Oscillations (BAO) and clusters of galaxies. This dissertation studies both aspects of large scale structure features (BAO) and objects (clusters and filaments).

To put this dissertation in context, I start by summarizing the average properties of the background Universe. Observations have led to a prevailing cosmological model, the "Concordance cosmology". In this cosmology, general relativity is assumed; the geometry of the Universe is flat, about 95% of the Universe is composed of dark energy and cold dark matter (CDM); right after the Big Bang, the Universe expanded exponentially, magnifying primordial density fluctuations that are adiabatic and gaussian. Under the priors of this model, many cosmological parameters are determined with high precision from the measurements of the anisotropies in the Cosmic Microwave Background (CMB). The CMB is the relic radiation from the Big bang, which measures imprints of the initial fluctuations (which then grew to all structures mentioned above). The most recent estimates of cosmological parameters (Planck Collaboration et al. 2013a) are presented in Table 1.1.

Although the standard model of cosmology and the initial conditions of the Universe have been well constrained, many questions still remain. Questions particularly related to this dissertation include what the nature of dark energy is, and how large scale structure forms and evolves. I discuss both of these in turn below.

Understanding the nature of dark energy is one of the outstanding problems in modern

parameter		value
Physical baryon density today	$\Omega_b h^2$	0.02207 ± 0.00033
Matter density today	Ω_m	0.314 ± 0.020
Dark energy density today	Ω_Λ	0.686 ± 0.020
Optical depth due to reionization	τ	0.097 ± 0.038
Scalar spectrum index	n_s	0.9616 ± 0.0094
Primordial curvature perturbation	$\ln(10^{10} A_s)$	3.103 ± 0.072
Linear matter fluctuations today	σ_8	0.834 ± 0.027
Expansion rate today	H_0	67.4 ± 1.4km s^{-1}Mpc^{-1}

Table 1.1: Cosmological parameters that are considered to fit current observations. The values are measured by the Planck collaboration (Planck Collaboration et al. 2013a) assuming the ΛCDM model.

cosmology. Compelling evidence for dark energy arose from observations of distant Type Ia Supernovae (SNIa) (Riess et al. 1998; Perlmutter et al. 1999). The apparent brightnesses of SNIa was fainter than expected, given their redshifts, meaning their light was emitted further away from us than expected, even as would be expected for an empty universe. This observation provides evidence that the expansion of the Universe is accelerating. If general relativity is correct, then this accelerated expansion, combined with the presence of mass in the universe, implies the presence as well of a kind of energy ("dark energy") that repels gravity. The current best candidate for dark energy is the "cosmological constant" (Λ) that Einstein first introduced in his field equations. Our understanding of the nature of the dark energy is still incomplete. It is not known whether dark energy is a constant Λ, or not a constant but instead evolving with time, or whether general relativity is wrong. To answer those questions, one of the most important tasks is tightly constraining the dark energy equation of state.

As dark energy only recently started to govern the Universe's expansion, measuring the expansion rate of the late time Universe is essential for estimating the dark energy equation of state. Common probes of the Universe's expansion rate are standard candles, standard rulers, and the growth of the structure. (For more details, see the review by Weinberg et al. (2012).) The standard candle method uses sources with well known luminosity such as SNIa. As mentioned above, this method estimates the expansion rate by measuring how much the brightness of sources dims as a function of redshift. Instead of using a known luminosity, one can also use a known distance scale ("standard ruler"). Given an absolute size of an object, its apparent angular scale on the sky tells us the distance to the object. By measuring this distance at different redshifts, the expansion rate of the Universe can be determined. The current most popular standard ruler is the scale of baryon acoustic oscillations (BAO). This method is studied in this dissertation and its details are reviewed in §1.1. The accelerated expansion of the Universe also affects the growth of the structure. As the dark energy retards the growth of structure (by stretching space between matter), measurements of the growth

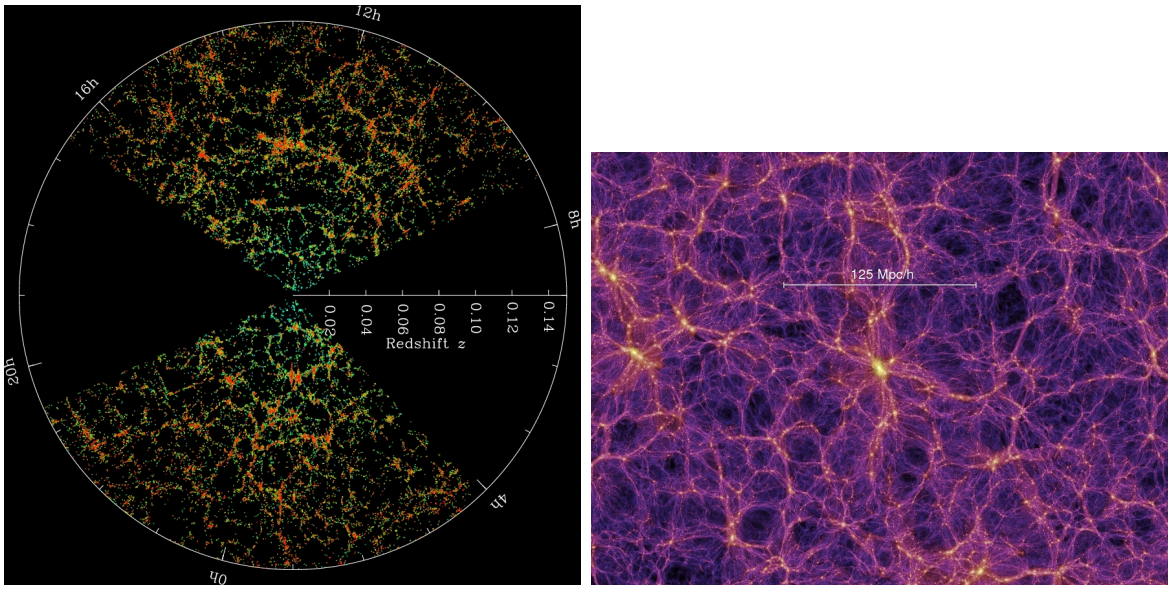

Figure 1.1: The 'cosmic web' is evident in both the observed galaxy (left) and dark matter (right) distributions. Credits: M. Blanton and the Sloan Digital Sky Survey (left) and Springel et al. (2005) (right).

rate can also probe the dark energy. The number density of galaxy clusters is one probe that is relevant to this dissertation, and a brief review of it is in §1.2.

In addition to information it can provide about the background cosmology, large scale structure itself is a topic of study. Large scale structure forms a complex network called the cosmic web, which consists of clusters, filaments, sheets and voids (Zel'dovich 1970; Bond et al. 1996). Examples in the observed galaxy and simulated dark matter distributions can be seen in fig. 1.1. These components were first characterized by Zel'dovich (1970) under the assumption of a hot dark matter universe. Here large structure forms first, and small structure forms later by fragmentation, which differs from today's hierarchical understanding. However, this characterization is still useful to describe the geometry of large scale structure in the CDM universe. Voids are vast and mostly empty regions, surrounded by two-dimensional structures, sheets, where matter is concentrated. One-dimensional structures, filaments, are even denser than sheets, bridging clusters that reside at the nodes of filaments, the densest regions. The structures are also related to the flow of matter, which moves from voids to sheets, to filaments, and finally into clusters.

Studying these structures, for example analyzing their growth from initial conditions and characterizing their physical properties, is becoming more productive due to advances in large scale numerical simulations as well as large volume surveys. These large simulations and surveys are necessary to include a range of scales, from those of galaxy formation and evolution, to those pertaining to the formation of large scale structure itself. Furthermore,

simulations that take into account in the relevant physics and what observations return allow theory and observation to be qualitatively compared. (The similarity between simulated and observed structures can be seen in fig. 1.1.) This dissertation uses cosmological volume simulations and mock observations constructed from them to study large scale structure. It focuses in particular on mass measurements of clusters and geometrical properties of filaments in cluster neighborhoods.

In the following sections, I give an overview of concepts and previous work for each of topics studied in this dissertation – BAO in §1.1, clusters in §1.2 and filaments in §1.3.

1.1 Baryon Acoustic Oscillations

Clustering of matter or galaxies on large scales shows the acoustic feature that is imprinted by baryon oscillations in the early Universe. These oscillations are a powerful tool for constraining the dark energy equation of state by providing a standard ruler. In this section, I will discuss what drives the acoustic oscillations and what modifies their imprint after their intial formation. Then I will review the BAO as a standard ruler and some current and future BAO surveys. The review is mostly based on Eisenstein et al. (2007b); Weinberg et al. (2012).

1.1.1 Theory

Before redshift $\sim$ 1000, the Universe is completely ionized, and photons and baryons are tightly coupled via Compton scattering and the Coulomb interaction. Due to tight coupling, the resulting photon and baryon plasma acts like a single phase fluid. This fluid is first compressed by the gravitational potential and then rarefied due to overpressure from the photons. (The gravitational potential is set by photons and relativistic matter before matter-radiation equality, and by CDM after matter-radiation equality.) The compression and rarefaction of the photon-baryon plasma generates acoustic oscillations with a sound speed $c_s = c/\sqrt{3(1+R)}$, where R is baryon-to-photon ratio. During tight coupling, R is given by $3\rho_b/4\rho_\gamma$ where ρ_b and ρ_γ are the baryon and photon densities, respectively. The baryon mass influences the acoustic motion by dragging, changing amplitudes for compressions vs. rarefactions. As the Universe expands, it cools, and photons no longer have sufficient energy to ionize hydrogen. Recombination occurs, and photon and baryon interactions decrease. During recombination, the oscillations are exponentially damped on small scale, due to the photon-baryon diffusion (Silk 1968). The damping scale is the mean free path at the time ($\sim$ 8 Mpc). When photons and baryons are finally decoupled, the photons travel out of the gravitational potential created by the matter perturbations and begin to freely stream, while the baryon overdensities start to gravitationally grow like dark matter overdensities. These physical processes in the photon-baryon fluid in the early Universe imprint the acoustic feature on clustering of matter or galaxies, as well as the CMB temperature anisotropies.

In the former, imprints in the matter perturbations are observed, in the latter, photon perturbations are observed.

In the matter or galaxy correlation function the BAO feature is observable as a sharp peak at the sound horizon scale at decoupling. The sound horizon is the distance the sound wave generated by acoustic motion in photon-baryon plasma propagated until decoupling,

$$\begin{aligned} s &= \int_0^{t_{dec}} c_s(1+z)dt = \int_{z_{dec}}^{\infty} \frac{c_s dz}{H(z)} \\ &= \frac{1}{\sqrt{\Omega_m H_0^2}} \frac{2c}{\sqrt{3 z_{eq} R_{eq}}} \ln \frac{\sqrt{1+R_{dec}} + \sqrt{R_{dec}+R_{eq}}}{1+\sqrt{R_{eq}}}. \end{aligned} \tag{1.1}$$

Here t is time, c_s is sound speed, z is redshift, $H(z)$ is Hubble parameter as a function of redshift, H_0 is the Hubble constant today, Ω_m is the total matter density, c is the speed of light and R is baryon-to-photon ratio. The subscripts dec and eq represent decoupling and matter-radiation equality, respectively.

To illustrate better the physics that drives the acoustic peak, it is useful to consider the evolution of an overdensity of photons, baryons, and dark matter that are initially located at the origin in configuration space as shown in fig. 1.2. The overdensities in photons and baryons evolve together, as they are tightly coupled, and the baryon-photon fluid spherically expands out due to the overpressure of the photons. At the same time, the CDM overdensity hardly moves from its initial location, but continues to grow. This growth becomes significant when matter starts to provide most of the energy density of the Universe. After decoupling, photons freely propagate and their overdensites are smoothed out. On the other hand, baryons stay at the location they reached with the photons (traveling with the sound speed c_s given above), forming a thick spherical shell. The scale of this spherical shell is equivalent to the sound horizon at that time, s, which is given in eq. 1.1.

Then baryons and CDM gravitationally attract each other and finally overdensities result at two locations – the center, where dark matter is overdense, and at s, where baryons are overdense. The overdense regions eventually tend to gravitationally collapse to form halos where galaxies form. This implies that the mean separation between halos (or galaxies) tends to be s. Therefore, a bump on the scale of s with a peak near the origin in matter and galaxy correlation functions is expected. Note that this acoustic peak in correlation function (configuration space) corresponds to wiggles in power spectrum (fourier space). The measurement of this peak can be used to constrain cosmological parameters because of the relations in eq. 1.1, as discussed in §1.1.2 below.

However, the position, amplitude and shape of the acoustic peak can be altered by non-linear effects at low redshifts, degrading the accuracy of acoustic scale measurements. The largest effect is from the non-linear gravitational growth of structure. Formation of small structures and bulk flows tend to change separations between dark matter particles on scales of about 10 h^{-1}Mpc. This broadens the sharp peak in the correlation function and can also slightly shift its position, reducing the constraining power of the measurement. To correct

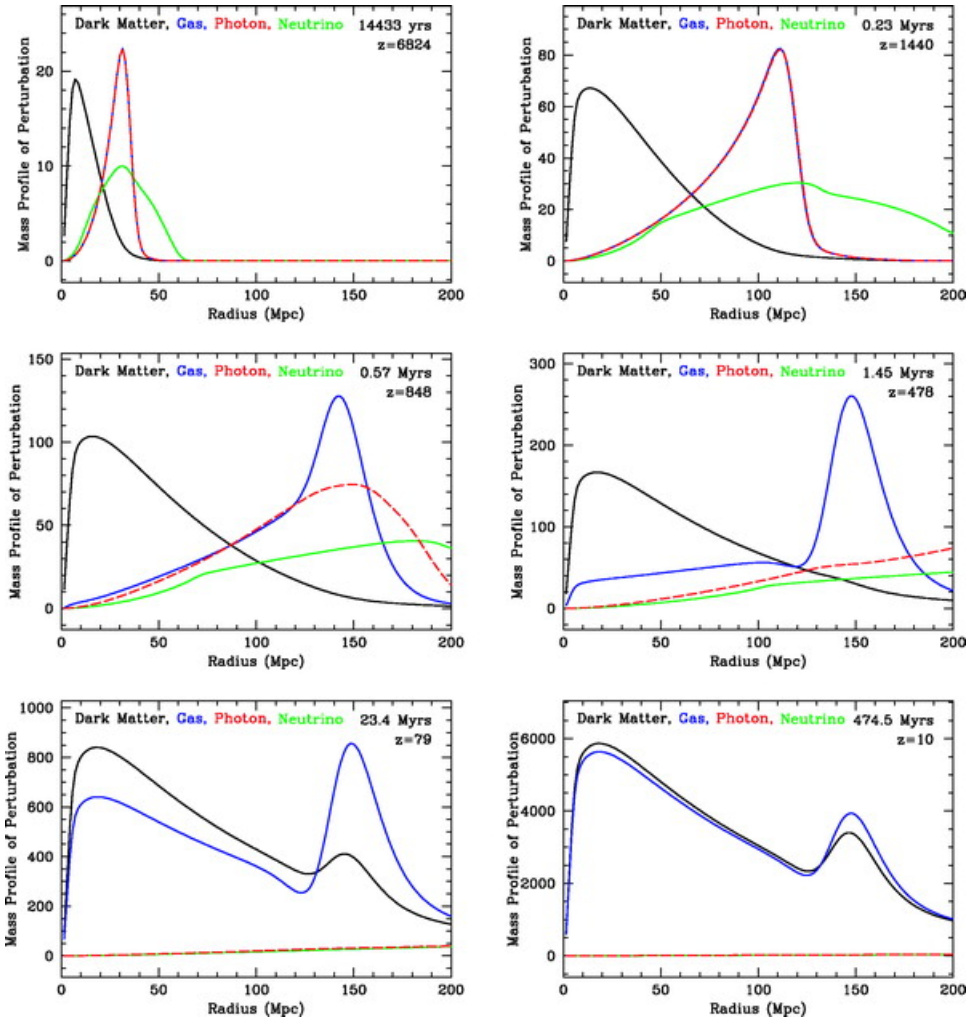

Figure 1.2: Snapshots of the radial mass profile of an initial point-like overdensity located at the origin. The lines are as follows: black (dark matter), blue (gas), red (photon), green (neutrino). The top figures are for the early time before recombination, the middle figures for soon after but close to recombination, and the bottom figures are for long after recombination. Figure credit: Eisenstein et al. (2007b).

this non-linear degradation, "reconstruction" was invented by Eisenstein et al. (2007a). This method is simple to implement but inherently non-linear and thus difficult to understand analytically. A part of this dissertation work presented in Chapter 2 aims to analytically understand this reconstruction method using Lagrangian Perturbation Theory, accompanied by a suite of large N-body simulations.

Bias is another non-linear effect affecting measurements of the acoustic peak. Galaxy formation is biased because galaxies form in overdensities, and overdensities are more clustered than the underlying matter distribution. This changes the amplitude of the correlations of galaxies relative to the correlations of matter. If that is the only significant difference, bias can be treated as a constant and thus, a linear relation between galaxy and matter overdensities or correlations can be assumed. In practice, bias can also affect the shape of the correlations or the location of the peak. In Chapter 2, along with the reconstruction using dark matter, we tested the accuracy of constant bias for dark matter halos (that represent galaxies).

A third non-linear effect that can further reduce the constraining power of BAO measurements (but is not studied in this dissertation) is redshift space distortions. These distortions occur since we actually measure positions not in real space but in redshift space, so positions measured along the line-of-sight include the peculiar motions of the objects relative to their real positions. Peculiar motion on large scales is due to coherent infall onto large-scale structure and can be reasonably handled by linear theory (Kaiser 1987). On the other hand, small scale peculiar motion is complicated to correct, and arises from the motion in virialized objects, adding scatter in measurements.

1.1.2 Standard Ruler Test

The location of the bump in the correlation functions can be used for a standard ruler test of the dark energy equation of state. As shown in eq. 1.1, the sound horizon, s, depends on $\Omega_m h^2$, the baryon-to-photon ratio, the redshift of equality, and the epoch of recombination. Precise CMB anisotropy measurements of these parameters can be used to determine the sound horizon and thus the location of the bump in the correlation function. Thus, the BAO scale can be used as a standard ruler. The current cosmology estimates the size of the ruler to be approximately 150 Mpc comoving.

The standard ruler test is observationally done through the measurement of galaxy clustering. The two point correlations of galaxies can be measured in terms of the angular separation of galaxies, i.e. the separation between galaxies projected on the sky, $\Delta\theta$. The angular scale of the location of the BAO peak corresponds to an angular diameter distance, $\Delta\theta_{peak} \propto s/d_A$. d_A in flat universe is given by

$$d_A(z) = \frac{c}{1+z}\int_0^z \frac{dz}{H(z)} \quad \text{where} \quad H(z) \propto \sqrt{\Omega_m(1+z)^3 + \Omega_{\rm DE}\exp\left(3\int_0^z \frac{1+w(z)}{1+z}dz\right)}. \tag{1.2}$$

Here, $w(z)$ is the equation of state of dark energy as a function of redshift. Thus, by measuring the angular diameter distance as a function of redshift, $w(z)$ can be constrained. The information along the line-of-sight can be also separately obtained by measuring the difference in redshifts of the galaxies. The separation in redshifts can be directly related to $H(z)$, $\Delta z \propto H(z)s$. By combining the two different orientation measurements, $H(z)$ and $d_A(z)$ can be independently estimated. This gives an internal cross check and tighter constraint on $w(z)$.

The first detection of the acoustic peak in a galaxy correlation function was done by Eisenstein et al. (2005). They used the luminous red galaxy samples of the Sloan Digital Sky Survey (SDSS) that covers 3816 deg^2 of the sky, large enough to measure correlations on the BAO scale (∼150 Mpc). Figure 1.3 shows their measurement. They estimated cosmological parameters from the measured correlation function and found the peak properties corresponded to what CMB experiments predicted. Since then, many surveys are ongoing and/or planned for constraining dark energy using BAO, with different types of objects tracing the underlying matter distribution. The WiggleZ survey targeted emission line galaxies at $0.4 < z < 1.0$ and detected the BAO with a precision of $\sim 4\%$ (Blake et al. 2011). The Baryon Oscillation Spectroscopic Survey (BOSS) is currently operating and provides luminous galaxies over 10,000 deg^2 to $z \approx 0.7$ and Lyman alpha forest measurements beyond $z \approx 2$ (Dawson et al. 2013). The most recent BAO analysis from BOSS (Anderson et al. 2013) measures $d_A(z)$ and $H(z)$ at $z = 0.57$ with a precision of a few percent and finds that dark energy is consistent with the cosmological constant model. The Dark Energy Survey is an imaging survey that is just commencing, and is expected to detect BAO at $z \approx 1$ using red galaxies. There are several future surveys that plan BAO measurements. The Hobby-Eberly Dark Energy eXperiment (HETDEX) will use ∼800,000 Lyman alpha emission line galaxies at redshift $1.8 < z < 3.7$ (Hill et al. 2006). EUCLID and WFIRST will use near-IR spectroscopy (Laureijs et al. 2011; Green et al. 2012). CHIME aims to use 21cm intensity mapping at $0.8 < z < 2.5$ (Peterson et al. 2006). These are expected to provide information about dark energy evolution in the redshift range $1 - 3$.

1.2 Galaxy clusters

Galaxy clusters are the most massive virialized objects in the Universe. They lie at the nodes of the cosmic web, corresponding to rare peaks of the initial matter density fluctuations. These most dense regions naturally form large gravitational potential wells, and thus most matter and halos accreted or merged into them are likely to be retained. (A summary of some properties of clusters are in table 1.2.)

In this section, I will briefly introduce some main topics of cluster studies and review what a cluster of galaxies is. I will start with a simple theoretical model of cluster formation and then discuss how clusters and their masses are determined in simulations and in observations. This review is primarily based on Voit (2005); Allen et al. (2011); Kravtsov & Borgani (2012).

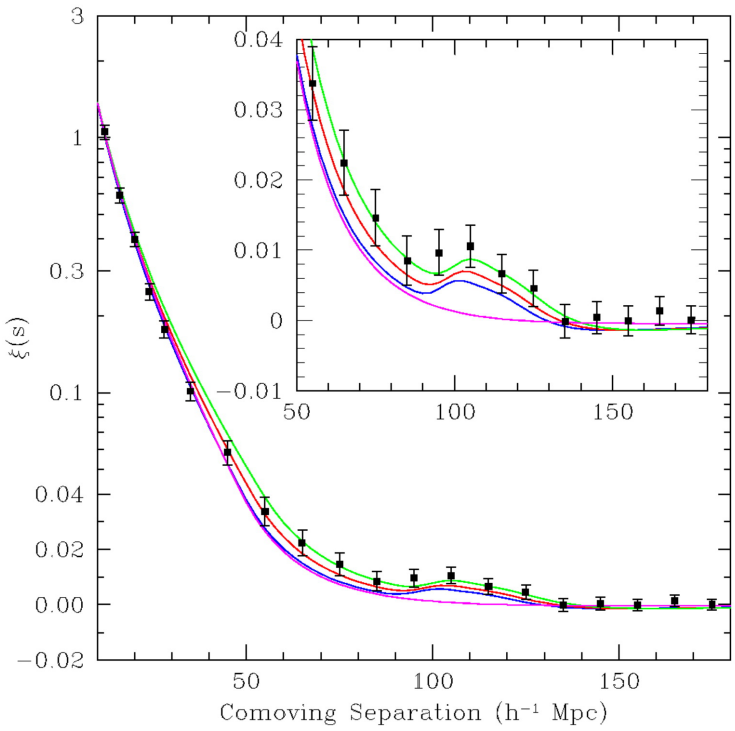

Figure 1.3: The correlation function in redshift-space measured by (Eisenstein et al. 2005) from the luminous red galaxy samples of the Sloan Digital Sky Survey. The observed correlation function is shown by points, with error bars estimated from a mock catalog. The inset is the zoom in for the acoustic peak. The solid lines represent model predictions with $\Omega_m h^2 = 0.12$ (green), 0.13 (red) and 0.14 (blue), respectively. All are taken to have the same $\Omega_b h^2 = 0.024$ and $n = 0.98$. For comparison, a model is shown (magenta line) with no baryons and $\Omega_m h^2 = 0.105$, which barely shows the acoustic peak. Figure credit: Eisenstein et al. (2005)

Mass range	$\sim 10^{14} - 10^{15}\ h^{-1} M_{\odot}$
Radius	$1 - 2h^{-1}$Mpc
The scale of the corresponding initial density fluctuation	$\sim 10h^{-1}$Mpc
Crossing time [1]	$\sim 9.8h^{-1}$ Gyr
Fraction of gas mass to total mass	~ 0.1
Fraction of baryon mass to total mass	$\sim 0.1 - 0.15$ [2]
Gas number density at the core	10^{-3} atoms per cm^3
Intracluster gas temperature	$3 - 10$ keV
X-ray luminosity	$10^{43} - 10^{45}$ erg/s
SZ parameter (y)	10^{-4}

Table 1.2: Representative numbers for cluster properties. Each quantity is explained in more detail in the main text.

1.2.1 A crossroads of cosmology and astrophysics

The characteristics described above in Table 1.2 allow a broad use of galaxy clusters in cosmology and astrophysics. Due to their large mass, they are rare and their number density drops quickly as their mass increases. As a result, statistical measures of cluster populations depend upon the growth rate of structure and the expansion history of the universe, which in turn are sensitive to cosmological parameters. Thus, clusters are used as probes of cosmology. Additionally, as clusters are recently formed objects, details of their internal structure and surrounding regions can elucidate how halos grow and filamentary structures form. Galaxy evolution also can be studied using cluster galaxies. In particular, the hot intra cluster medium (ICM), heated by adiabatic compression and shocks, provides a special environment for galaxies within. Many interesting astrophysical phenomena occur in cluster regions, including radiative cooling and energetic feedback from supernovae or active galactic nuclei (AGN). Another example is shock heating driven by vigorous baryonic inflows into clusters, due to their large gravitational potentials. As an example of one use of cluster studies, below I briefly summarize the use of cluster abundances as a cosmological probe.

Cluster Cosmology

As mentioned earlier, cosmological parameters can be constrained by observationally measuring structure growth and comparing with theoretical predictions. One popular method uses the evolution of cluster abundances. First, the comoving number density of halos as a

[1] Crossing time is calculated approximately by dividing the radius by the velocity dispersion.

[2] The baryon budget in cluster is quite different from the cosmic budget; the hot gas fraction is about 82% ($51 - 100\%$), the fraction of other baryons (probably WHIM) is about 12% ($0 - 45\%$) and stars and intracluster light which are relatively cold consist of 6% ($3 - 10\%$) of cluster baryonic mass (Ettori 2003; Ettori et al. 2009).

function of mass is theoretically predicted. This is the mass function

$$\frac{dn(M,z)}{dM} = f(\sigma(M,z))\frac{\bar{\rho}}{M}\frac{d\ln\sigma(M,z)^{-1}}{dM}, \tag{1.3}$$

(e.g. Jenkins et al. 2001). Here $\bar{\rho}$ is the background matter density proportional to Ω_m, and σ is the rms of the density fluctuations, depending on the matter power spectrum and the growth rate. σ basically contains the cosmological information. (Recall that the most recent estimated cosmological parameters are shown in Table 1.1.) $f(\sigma)$ is a differential mass function, which is considered nearly universal, independent of redshift and cosmology (e.g Lukić et al. 2007) though Tinker et al. (2008) pointed out that the amplitude of $f(\sigma)$ changes when changing the definition of halo mass. The theory prediction of the mass function can be analytically calculated (e.g. Press & Schechter 1974) or taken from fits to simulation data (e.g. Sheth & Tormen 1999; Lukić et al. 2007; Tinker et al. 2008). The mass function exponentially drops at the cluster mass scale and thus, cluster abundance sensitively changes as cosmological parameters vary. This is a key to using observed cluster abundances as a cosmological probe. Predicting the mass function for different redshifts and cosmologies is crucial for interpreting observed cluster abundances.

The mass function Eq. 1.3 is not directly measurable observationally, however. The observed number density of clusters selected by an observable O, in a given survey volume, is

$$\frac{d^2N(z)}{d\Omega dz} = \frac{\chi^2(z)}{H(z)}\int_0^\infty f_s(O,z)dO\int_0^\infty p(O|M,z)\frac{dn(z)}{dM}dM. \tag{1.4}$$

The total cluster number $N(z)$ depends on the comoving halo abundances, dn/dM, given in eq. 1.3. $N(z)$ also depends on the comoving distance, $\chi(z)$, the Hubble constant (i.e. expansion rate), $H(z)$, the selection function at the observed redshift, $f_s(O,z)$, and a probability function connecting observables O to a halo of mass M at a redshift z, $p(O|M,z)$ (e.g Frieman et al. 2008). Once the ingredients f_s and p are properly calibrated, and the correctly estimated theoretical mass function, dn/dM, is used, one can determine cosmological parameters from $\chi(z)$ and $H(z)$. The expansion rate can be further constrained when abundances are measured in different redshift bins. This in turn constrains the dark energy equation of state. A simple method is first to fit a theoretical mass function with low redshift data, assuming a cosmological model. Then one tests if the theoretical mass function extrapolated to higher redshifts with the same parameters agrees with high redshift data (e.g. Vikhlinin et al. 2009). The correct cosmological model will match with every redshift bin. One example of such a measurement is shown in fig. 1.4.

There are several additional ways to use clusters to constrain cosmological parameters. Clustering of clusters is a measurement which also depends upon the growth rate (a recent measurement using this method is given in Mana et al. (2013)). In principle, one might also use the Baryon Acoustic Oscillation (BAO, more details are in §1.1) feature in the cluster correlation function or power spectrum, but for clusters such measurements are not statistically significant enough to determine cosmological parameters (Estrada et al. 2009;

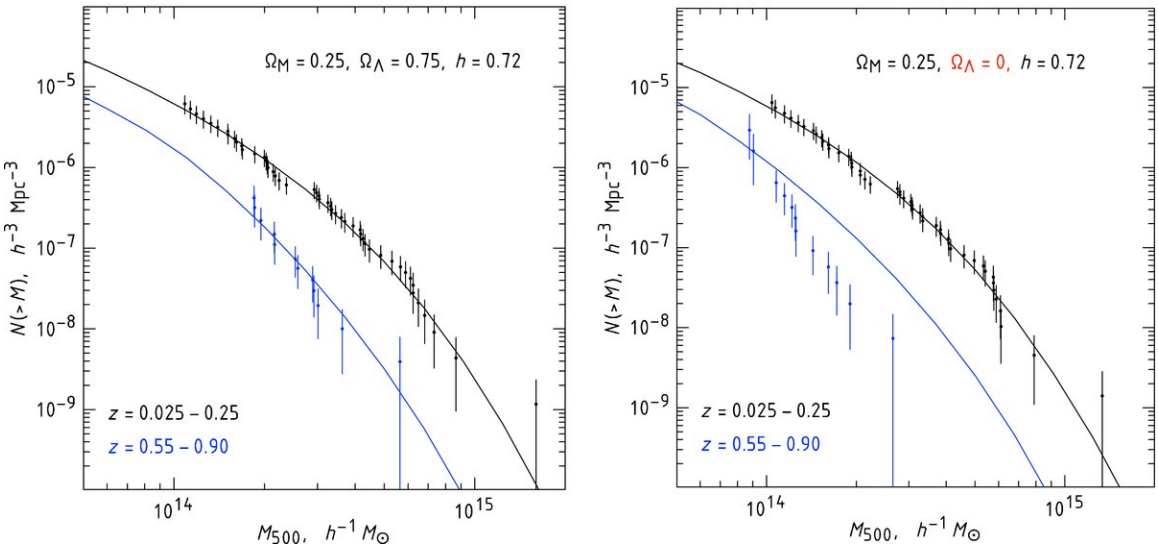

Figure 1.4: The measured mass functions at two different redshift ranges, $z = 0.025 - 0.25$ (black points) and $z = 0.55 - 0.9$ (blue points). Also shown are smooth curves of theoretically predicted mass functions, using different cosmology assumptions. At left is the ΛCDMmodel and at right a flat cosmology without Ω_Λ. The overall normalization that corresponds to the amplitude of density fluctuations is taken to match the measured and the theoretical mass functions at $z \approx 0$ under the assumption of the cosmological model. Assuming a set of different cosmological parameters changes both the observed and the theoretical predicted mass functions (i.e. the data points with error bars and solid theory curves in left panel are plotted differently from those in right panel though the observed data are the same and the same universal mass functions are taken.) The difference in the observed mass function is caused by the conversion from redshift to distance. The theoretical mass function changes due to differences in the growth rate and mean matter density. The data and the theory prediction in the left panel are in agreement in both redshift bins. This suggests that the assumed cosmology is right. In the right panel, the theoretically predicted mass function fails to match the higher redshift data with the prediction, even though they agree at low redshift. Figure credit: Vikhlinin et al. (2009).

Balaguera-Antolínez et al. 2011). The mass of the most massive cluster is another probe since the more efficiently growth occurs, the more massive clusters are. Growth is set by cosmological parameters. In addition, some studies suggested that the gas fraction of clusters can be used like a standard ruler method to obtain cosmological information (Allen et al. 2008), but this is still controversial.

For studies such as mentioned above, identifying clusters and determining their masses is essential. For example, as can be seen in fig. 1.4, poorly determined or biased cluster masses can cause large errors in cluster abundance measurements, because of the sharp drop in the mass function at the cluster mass scale. These measurements would then result in mistaken estimates of cosmological parameters.

However, determining cluster mass is not straightforward. In part this is because there is no easily determined sharp boundary distinguishing a cluster. With no unique definition of what a cluster is, different definitions give different cluster masses. More importantly, direct mass measurement is impossible observationally. Some mass related observables are measured instead.

1.2.2 Theoretical Model

First, in theory, what is a cluster of galaxies? A galaxy cluster is a massive dark matter dominated halo (which is a gravitationally bound object). To understand the theoretical view of a galaxy cluster, it is instructive to discuss a very approximate description of halo formation, called the 'spherical collapse model'. This model requires only one parameter, overdensity, $\delta = (\rho - \bar{\rho})/\bar{\rho}$, where $\bar{\rho}$ is the mean mass density of the Universe. (This model neglects many complicated processes such as merging and triaxial collapse.) Collapse in this model occurs in a spherically symmetric way, under the assumption that a density peak is a sphere of uniform overdensity, δ. The collapse of this overdense region can be considered to be equivalent to the evolution of a matter only universe with the same overdensity (Birkhoff's theorem): A sphere of overdensity δ initially expands with the same rate as the background. Then its expansion slows down because the gravity from the overdensity inside causes it to detach from the smooth background and "turn around". After turn around, it keeps collapsing until virialization, which happens at one half of the turn-around radius (Gunn & Gott 1972). The region that can turn around and collapse has overdensity $\delta \gtrsim \delta_L^{col}$. Here, $\delta_L^{col} = 1.686$ is estimated by linearly evolving the density field. The final non-linear overdensity at virialization is $\Delta_b(z) = 18\pi^2 \simeq 178$ in the Einstein-de Sitter universe, and $\Delta_b \approx 18\pi^2 + 82[\Omega_m(z) - 1] - 39[\Omega_m(z) - 1]^2$ for a flat universe with a nonzero cosmological constant ($w = -1$) (Bryan & Norman 1998). Note that $\Delta_b \simeq 180$ is often adopted in finding halos in N-body simulations. Thus, a halo refers to an object with the non-linear overdensity, Δ_b. Massive halos (typically more massive than $10^{14}h^{-1}M_\odot$) are considered to be clusters.

1.2.3 Simulations

The simple analytic description of halos overviewed above is extremely approximate. In order to more accurately capture details of halo formation and other properties, numerical simulations are used. Cosmological dark matter only simulations (N-body simulations) are often used for studies of clusters [1]. Two methods are usually employed to identify halos in simulations. One uses spherical overdensities, and the other is based upon the Friends-of-Friends algorithm. Each method is briefly reviewed in below.

The spherical overdensity (SO) method is an adaptation of the idea of the spherical collapse model. In this model, a halo corresponds to a peak of the density field computed from the simulated particles. The boundary of a halo is the radius R of a spherical region, centered on the peak, with average overdensity Δ. Different values of Δ correspond to different SO masses, generally Δ is fixed for the whole catalogue. For example, a common value is $\Delta = 200$ relative to the critical density (the total energy density of a flat universe), which is close to that within virialized objects if $\Omega_m = 1$. This overdensity is almost independent of cosmology (White 2001) and changes the mass function ($f(\sigma)$) less as a function of redshift (Tinker et al. 2008). Some studies use Δ relative to the background density, which is the value of the critical density multiplied by $\Omega_m(z)$ at a given redshift. The mass is then $M_\Delta = \frac{4\pi}{3}\Delta\rho_\Delta R^3$ where ρ_Δ is the reference density of Δ, e.g. the critical density or the background density. This method is also often used to assign masses of clusters in observations, particularly in X-ray observations.

Another way to define halos is the Friends-of-Friends (FoF) algorithm (Davis et al. 1985). A pair of particles are friends if the distance between them is shorter than a given linking length, b; the particle's other friends also become its friends. The linking length, b, defined in units of the mean inter-particle spacing, is the only parameter. All friend particles are then considered to be in the same halo and the halo mass is the sum of the mass of the halo particles. The shape of halos determined by this method is not fixed to be spherical, unlike the halos identified by SO. Typical choices of the linking length are $b = 0.1,\ 0.15$ and 0.2. Note that this halo definition tends to connect particles in regions with overdensity $\Omega_m b^{-3}$ relative to critical (White 2001). $b = 0.2$, which corresponds to $\Delta = 200$ in SO, is often favored as resulting halos are likely to possess a universal mass function (Jenkins et al. 2001; White 2001). This method is simple to adapt to simulations since it finds halos directly from particle positions. In contrast, interpreting the outcomes of this method is difficult with analytic models as the FoF algorithm and analytic models define clusters in different ways.

[1] Hydrodynamic simulations are also beginning to be used to study details of astrophysical processes in clusters. Running cosmological size simulations with hydrodynamics is still limited as it is numerically extremely expensive, and in addition several different implementations of gas physics are still being investigated.

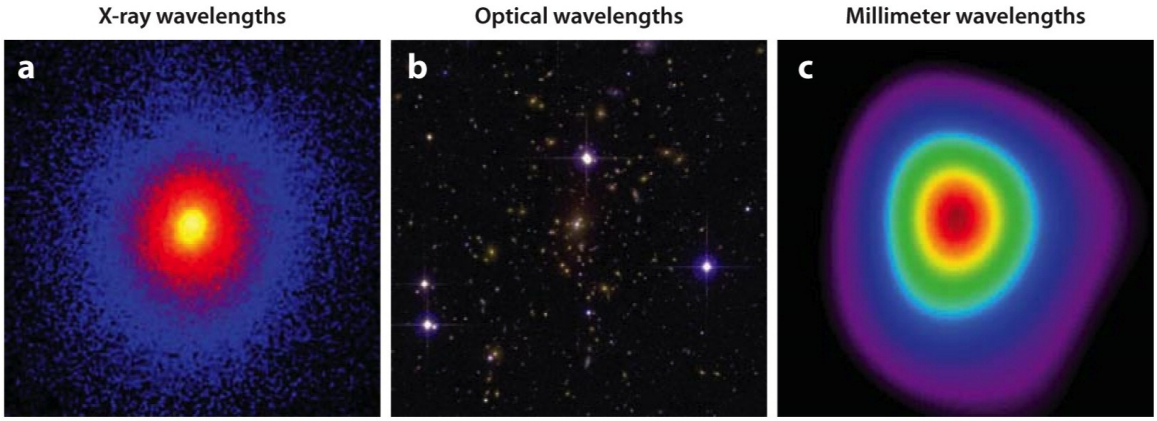

Figure 1.5: Images of a relaxed cluster, Abell 1835 at three different wavelengths: (a) X-ray, (b) optical, (c) millimeter. All three images are centered on X-ray peak position with the same spatial scale on a side (5.2 arcmin or 1.2 Mpc). Figure credits: X-ray: Chandra X-ray Observatory/A. Mantz; optical: Canada-France-Hawaii Telescope/A. von der Linden et al.; millimeter: Sunyaev Zel'dovich Array/D. Marrone. From Allen et al. (2011).

1.2.4 Multi-wavelength Observations

The measurements in observations are not the same as those directly provided by dark matter simulations. In simulations, cluster (halos above a certain mass) masses are directly measured, from the matter density or the sum of the halo dark matter particle masses. Dark matter halos are not directly observable through telescopes. Other components of or near clusters that emit or scatter radiation are observed. Many of the observables are correlated with the underlying dark matter halos and so are used to compute the total mass of clusters. Understanding how these observables are connected with the mass (the variable in eq. 1.4) is one of the key ingredients in cluster studies as discussed in section 1.2.1.

In observations, different components of a cluster are revealed depending on the observational wavelength used (an example is shown in fig. 1.5). Thus, multi-wavelength observations can provide a variety of observables, many of which can be used to estimate cluster masses. As these observables are correlated with the total mass in different ways, they can be complementary. In below, I review some mass observables that are generally used in X-ray, optical and microwave.

X-ray

A cluster is a very luminous and spatially resolved object in X-ray. Its X-ray radiation is caused by the collisions (in gas) in the hot Intracluster Medium (ICM). The ICM is heated by the large gravitational potential of the dark matter halo. As most atoms in ICM are ionized, the dominant source of this radiation is thermal bremsstrahlung (free-free) emission. The

total luminosity density emitted by bremsstrahlung is proportional to $T_X^{\frac{1}{2}} n_e n_i$ where T_X is the X-ray temperature, and n_e and n_i are the number densities of ions and electrons, respectively. This X-ray luminosity can be used as a mass proxy. Other X-ray observables for cluster mass are the X-ray temperature, the integrated X-ray pressure Y_X (motivated by the integrated Compton decrement below), and ICM metal abundances(Voit 2005). When converting X-ray observables to mass, an important assumption is often hydrostatic equilibrium in the ICM. This can lead some biases in mass estimates, especially for the case of unrelaxed clusters (e.g. Allen et al. 2011). It also should be considered that X-ray mostly observes the cores, at least when clusters are relaxed, (as gas tends to be settled toward the minimum of the gravitational potential and the luminosity depends upon the gas density as $\propto n^2$).

Optical

Optical cluster studies include looking for large populations of galaxies, the most traditional way to observe clusters (Abell 1958). Galaxy clusters contain many red galaxies (or early type galaxies), tens to hundreds, depending on the galaxy luminosity cut. The number of cluster galaxies is one optical mass proxy. For example, the empirical relation between red galaxy richness (N_{gal}) and the radius (R_{200}[2]) of a cluster in the maxBCG cluster sample (Koester et al. 2007) is taken to be $R_{200} = 0.156 N_{gal}^{0.6} h^{-1}$Mpc (Hansen et al. 2005). R_{200} then determines a mass estimate. The integrated luminosity of galaxies in a cluster is also often used for mass. These optical mass proxies assume that the luminosity distribution traces the underlying mass distribution, which can be a source of errors. Also, the uncertainty in determining which galaxies are in the cluster is considered to be a major source of errors.

Once a cluster of galaxies is identified, the velocity dispersions of galaxies can be measured, which can be another mass proxy. For typical clusters, the velocity dispersion measurements are in order of 1000 km/s. Note that the velocity dispersion measurement of Coma cluster was the first evidence of dark matter (Zwicky 1937). Zwicky found that the total mass implied by the velocity dispersions of cluster galaxies was larger than the mass estimated from the total luminosity. The velocity dispersion mass estimate uses the Jeans equation (Binney & Tremaine 1987) and assumes dynamical equilibrium and spherical symmetry. Thus, the actual long relaxation time of galaxies in a cluster potential and their anisotropic velocity dispersions can cause errors in this mass estimate (e.g White et al. 2010).

Instead of using galaxies in a cluster, background galaxies at higher redshifts can be used to determine the mass of an intervening cluster via gravitational lensing. In general relativity, gravitational lensing is a natural consequence of mass concentration. It magnifies the brightness or distorts the shape of background galaxies. As clusters are massive, they can act as significant gravitational lenses. By measuring changes of magnification or shear of background galaxies, a cluster's mass can be estimated. Often measurements from many clusters are stacked together to enhance weak gravitational lensing signals (e.g, Rykoff et al. 2008). Strong lensing is also beginning to be combined with weak lensing for more precise

[2]the radius at which the average overdensity of a halo becomes $\Delta = 200$.

measurements. An advantage of estimating cluster mass by lensing is that it requires no assumptions of dynamical or thermal state of clusters or of galaxies as mass tracers. However, projection effects due to the cluster shape and the intervening large-scale structure between lens and observer add uncertainty to this method, as lensing measures a weighted sum of all mass along the line of sight. Other sources of contamination for weak gravitational lensing are the weak signal and lack of the redshift information of galaxies (e.g Hoekstra 2007).

Microwave

At microwave wavelengths, clusters can be observed through the Compton decrement or increment of the CMB. This is known as the thermal Sunayaev-Zeldovich (tSZ) effect (Sunyaev & Zeldovich 1972). The tSZ effect occurs because CMB photons are scattered via Inverse Compton scattering by the hot gas within galaxy clusters. This effect and the radio dusty infrared emitting galaxies that contaminate the SZ signal dominate CMB anisotropies on the $\sim$ arc minute scales. The tSZ scattering shifts the CMB spectrum (i.e. the Planck black body spectrum) observed through the cluster to higher frequencies by $\Delta\nu/\nu \sim kT_e/mc^2$. As a result, in the presence of clusters, at low frequency ($\nu < 217$ GHz), the flux of CMB photons decreases, while the flux increases at high frequency ($\nu > 217$ GHz). There is no change at $\nu = 217$ GHz.

A typical tSZ measurement quantity is the Compton y parameter, the energy change in the CMB photons due to scattering. The y parameter depends on the cluster temperature and electron number density. To obtain better SZ measurements for clusters which are not well resolved, one often uses the y parameter integrated over the size of the cluster. This is related to the total thermal energy in electrons, which can be converted to cluster mass assuming that gas mass is proportional to total mass. One weakness of this mass estimate, similar to X-ray, arises from the assumption of hydrostatic equilibrium. In addition, all intervening structures to the last scattering surface ($z \sim 1000$) can distort the CMB spectrum. This contaminates the signal from a target cluster. Also, as CMB distortions are what is observed, the cluster redshift is not accessible. Other follow-up observations are necessary to obtain the cluster redshift. Nevertheless, the tSZ is useful to identify distant clusters, because tSZ flux gets dimmed much less as a function of redshift relative to optical or X-ray flux. Another advantage of tSZ measurements are their relatively weak dependence on the gas density ($\propto n$) compared to X-ray luminosity ($\propto n^2$). This can give more information about the outskirts of the ICM and even better constraints on cluster gas density profiles, by combining with X-ray measurements, which can help to produce better gas mass and ultimately total mass estimates.

As discussed above, different cluster mass observables have different advantages and disadvantages and use different assumptions, depending on measurement technique and wavelength band. Thus, different cluster observables are often combined to understand cluster mass measurement systematics. However, the correlations of the errors in different measure-

ments can decrease the usefulness of combining measurements. In addition, these correlations can even lead to biased measurements or incorrect error estimates (Rykoff et al. 2008; Cohn & White 2009; Stanek et al. 2010; White et al. 2010). Thus, in order to fully use complementary multiwavelength information, and to best measure cluster mass, it is important to improve our understanding of the mass scatter correlations. A part of this dissertation concerns these correlations, particularly in understanding the physical origins of the correlated scatter (Chapter 4).

1.3 Large scale filaments

Filaments play a vital role as channels for matter as structure forms and evolves. For instance, galaxies and gas are fed to clusters through filaments. Filaments also influence cluster observations such as those mentioned earlier (§1.2.4). Uncertainties in observed cluster properties can be generated via projection effects including filaments. A filament elongated along the line of sight can look like a cluster. A filament can also interfere with accurately identifying properties of a cluster upon which it ends. A part of this dissertation tackles the understanding the properties of filaments and their effect on cluster observations by considering filaments in cluster neighborhoods (Chapter 3).

There are many other interesting aspects of filaments in addition to their relation to galaxy clusters and effects on cluster measurements. Halos and galaxies in filaments are sometimes studied to see how galaxies evolve in lower density regions before accreting or merging onto clusters. For instance, investigations have tried to determine whether being in a filamentary region affects galaxy morphology or color (e.g Gay et al. 2010; Wang et al. 2011). Alignment between galaxies and their host filaments, or between galaxies in the same filament has been also studied (e.g Lee 2004; Altay et al. 2006; Zhang et al. 2009). In addition, filaments are used in searches for the Warm Hot Intergalactic Medium (WHIM). Hydrodynamic simulations have indicated that half of the baryonic mass at low redshift ($z < 2$) is within the WHIM (Cen & Ostriker 1999). Some observational measurements have been made, but detections are still preliminary (e.g Werner et al. 2008).

In the studies above, the identification of filaments plays an essential role. The complexity of filamentary structures has resulted in numerous techniques to find filaments. In this section, I will review several popular filament finders, starting with a theoretical argument for the existence of the filamentary structure. Then I will discuss some results from previous numerical, observational, and analytic studies related to this dissertation.

1.3.1 Filament Finders

How does filamentary structure appear? A theoretical argument is found in Bond et al. (1996), which is now widely accepted. They argue that the cosmic web in a CDM universe

is caused by the spatial coherence of the large scale tidal field, induced by the rare peaks in the initial density field. They verified this idea by finding coherent structures in the initial conditions and comparing them to the final cosmic network, in dark matter only (N-body) simulations. Note that filaments can also be found in different quantities such as halos, galaxies and gas since their densities trace that of dark matter. The idea in theory seems simple but identifying filamentary structure is difficult due to the large range in scales of filaments and connectivity with clusters and themselves. This has led to the development of many filament finders, which is one of the active research areas in filament studies. Many finders fall into one of two categories: using the smoothed density field, or using the discrete objects directly.

Finding filaments based on the smoothed density field primarily use the tidal field information. Structures lying along a principal axis of the tidal field, in observations or in simulations, are taken as filaments (e.g., Hahn et al. 2007b; Bond et al. 2010a,b; Choi et al. 2010). In order to use this method, one first constructs the density field from the distribution of discrete objects such as galaxies (in observation) or dark matter halos or dark matter particles (in simulations) by assigning these objects to grids. Common schemes for grid assignments are the Nearest Grid Point (NGP), the Cloud In Cell (CIC), or the Triangular Shaped Cloud (TSC) methods (for more details, see Binney & Tremaine (1987)). Voronoi and Delaunay tessellation methods can also be used to avoid introducing free parameters such as the grid size (Schaap & van de Weygaert 2000). The density field is then smoothed and the Hessian of its fluctuations or gravitational potential is calculated. For instance, $\partial_i\partial_j\delta_S$ or $\partial_i\partial_j\phi_S$, where δ_S and ϕ_S represent the overdensity and the gravitational potential of the smoothed field, respectively. Finally, the eigenvalues of the Hessian are used to classify regions into voids, sheets, filaments and clusters. Structures are voids if all eigenvalues are negative, sheets if only one eigenvalue is positive, filaments if only one eigenvalue is negative and clusters if all eigenvalues are positive. Note that the signs of the eigenvalues depend on the convention used. More sophisticated methods modify this approach, such as the Multiscale Morphology Filter (Aragón-Calvo et al. 2007b), the Skeleton method (Novikov et al. 2006a; Sousbie et al. 2008a) and so on. The pros of these methods are that they are mathematically robust and need few free parameters, as they are based on the underlying physics of filaments. Practically, however, these method require constructing a smooth and continuous density field from discrete objects, which is not straightforward.

Instead of constructing a smooth density field, one can identify filamentary structure directly from the discrete objects of interest. The basic idea is to join halos or galaxies into structures. Several versions exist and details of each can be considerably different. One example is the "minimal spanning tree" (Barrow et al. 1985; Colberg 2007). This mathematically motivated method determines a unique connection between a set of discrete points. The Candy model (Stoica et al. 2005) is another example, which adopts a marked point process to simulate random networks of segments. One can also find filaments simply by looking for one dimensional objects connecting two clusters (Colberg et al. 2005). A main disadvantage of these types of methods is that they often require many free parameters that

need to be tuned and the findings of filaments can be changed depending on the choice of parameters.

There are also other methods which don't fall directly into either of these classes, for example, the methods using the information of the alignment of galaxies (Plionis et al. 2003; Pimbblet 2005b; Struble & Peebles 1985) or the velocity field (Shandarin 2011). Another example is by Murphy et al. (2011), who modified the Friends-of-Friends group finder (Davis et al. 1985, briefly described in §1.2) to find filaments in observed galaxy distributions.

The filament finder we used to study filaments around galaxy clusters is based on connecting discrete objects, as described above. Further details can be found in Chapter 3.

1.3.2 Filament Properties

As computational and observational techniques advance, the number of studies on filaments has increased, and more diverse properties of filaments are being studied. On the numerical side, particularly, cosmological simulation volumes now allow capturing many statistical characteristics such as the number statistics of filaments, the filament distribution at different redshifts, etc. These simulations are mostly done with dark matter, but studies using hydrodynamic simulations are also in progress. Observationally, filaments are notable structures in optical galaxy surveys, with which statistical analysis is now becoming possible. In X-ray and microwave bands, filament searches in gas distributions are just beginning. Searching for filaments in multi-wavelength bands is difficult, because compared to clusters, they are unbound and less dense, but more complicated in shape. There are only a few analytic studies due to the challenges of defining filaments.

Numerically, employing many filament finders, many questions have been investigated including the relation of filaments to clusters. One question is whether the majority of matter which falls onto clusters is from filaments. One of the earliest studies on this is Colberg et al. (1999). They observed that the majority of matter infall into a cluster is along filamentary structures around the cluster, which can be interpreted as evidence of filaments feeding clusters. Colberg et al. (2005) investigated filaments connecting massive neighboring halos. They found that the number of cluster filaments increases as cluster mass increases, that filaments connecting two clusters tend to be more straight when clusters are closer, that the density of filaments increases closer to their cluster endpoints and that the radial density profile of cylinder-like filaments drops as r^{-2} toward larger radius. Chapter 3 is partly an extension of Colberg et al. (2005), looking at some of properties of filaments they studied in cluster neighborhoods, and analyze particularly their geometry.

Another interesting question that has been asked is how filamentary structure evolves. Recently, for example, Bond et al. (2010a,b) showed that filamentary structure was in place at high redshift ($z > 3$), and that filaments are transients on the way to the formation of clumps that form at nodes. These results are consistent with the (Bond et al. 1996) picture of the cosmic web mentioned above.

Observationally, filaments have been analyzed statistically using large galaxy surveys.

As with simulations, the role of filaments as a bridge between clusters has been studied. For example, Pimbblet et al. (2004) found in the 2dF Galaxy Redshift Survey catalog that intercluster filaments tend to be straight if they are short in length ($\lesssim$ 5Mpc), but warped or irregular if longer. This can be seen as observational evidence that filaments are induced by the tidal field of nearby clusters. They showed that the majority of clusters tend to be connected by filaments, and that more than 70% of filaments are shorter than 10 h^{-1}Mpc. Bond et al. (2010a,b) applied the Hessian of the smoothed density method to the Sloan Digital Sky Survey (SDSS) galaxies. They found that filaments dominate with $\sim 10h^{-1}$Mpc to $\sim 25h^{-1}$Mpc smoothing, and that the average filament thickness is between $\sim 5.5h^{-1}$Mpc and $\sim 8.5h^{-1}$Mpc.

In relation to Chapter 3, the observational length scales of Pimbblet et al. (2004) above are encouraging for our choice of a 10 h^{-1}Mpc maximum length for filaments around a cluster, but those of Bond et al. (2010a,b) are bigger than the initial choices of free parameters of our filament finder. The latter are $3h^{-1}$Mpc and $10h^{-1}$Mpc for the maximum thickness and length, respectively. As the methods used in our simulation and in their observations are not directly comparable, an exact agreement in scales is not necessarily expected. (Also, note that our initial filaments were also adjusted by growing width and merging, making them thicker than the initial parameterizations (Chapter 3).)

Observationally the length of the longest filament has also been sought. This was not considered in this dissertation (the finder had a restricted filament length), but is worth mentioning because this length is expected to be related to the growth of structure and ultimately, cosmological parameters. Recently, in the Las Campanas Redshift Survey [3], (Bharadwaj et al. 2000, 2004) used Shapefinders to find a longest filament length between $50h^{-1}$Mpc and $70h^{-1}$Mpc. As a comparison to results in simulations, González & Padilla (2010) found that the length scale of filaments increases up to $150h^{-1}$Mpc.

Filament measurements using other observational tracers besides galaxies have begun. There are many efforts to find filaments in X-ray observations, in part to search for missing baryons, the WHIM, as mentioned above. Now, weak lensing and the thermal Sunyzev-Zeldovich (tSZ) effect are also starting to be used [4]. However, observing filaments with these methods is hard, as mentioned in the beginning of this section. In X-ray, the density of filaments is considerably lower relative to that of clusters, and X-ray flux is sensitive to gas density. Both weak lensing and tSZ suffer from projection effects. These can be worse for filaments relative to clusters since the signals from filaments are weaker. Some filament observations have been made nonetheless. These mostly focus on detection of filaments in systems of a few clusters, analyzing individual filaments. For example, Werner et al. (2008) observed soft X-ray emission along the segment connecting two clusters in the Abell 222/223 supercluster system. The gas temperature they estimated agrees with the prediction by hydrodynamic simulations, possibly giving evidence that filaments are the reservoir of missing

[3]The survey observations were carried out at the Carnegie Institution's Las Campanas Observatory in Chile

[4]More details of multi-wavelength observations are described in §1.2.

baryons (WHIM). The same system was also observed through weak gravitational lensing (Dietrich et al. 2012). The mass distribution they found by weak lensing measurements was consistent with the Werner et al. (2008) gas distribution. Planck Collaboration et al. (2013b) made the first attempt to detect filaments through tSZ using pairs of clusters. Further progress in multi-wavelength observations of filaments would help to understand the effect of filament structures on cluster observations, (which is studied in Chapter 3 and Chapter 4 using a simulation) as well as multi-component (e.g. warm gas, galaxies) of filaments.

I close by describing some analytic studies of filaments. A core utility of analytic study is simplification, but the multi-scale nature of filaments is difficult to approximate. As a consequence, only a few attempts have been made since the initial work by Zel'dovich (1970). One analytic description of filaments is based on the ellipsoidal collapse model (White & Silk 1979) and excursion set theory (Bond et al. 1991). Based on this description, Shen et al. (2006) constructed a model, and predicted some filament properties, including abundances. Although their model can reproduce statistics for filamentary physical properties such as the filament mass function, their specific numbers are difficult to compare with numerical or observational results, due to e.g. differences in filament definitions. Song & Lee (2011) estimated a merging rate of low mass halos ($10^6 M_\odot$) onto filaments or more massive halos at high redshift ($z > 3$) based on the same analytic description.

1.4 Dissertation Outline

First, the study of the large scale structure as a standard ruler is presented in Chapter 2, where we investigate the BAO "reconstruction" method in N-body simulations within the context of Lagrangian Perturbational Theory. Then I turn to objects comprising large scale structure. In Chapter 3, the properties of filaments around galaxy clusters in a high resolution N-body simulation are discussed. The effect of filaments on galaxy cluster mass measurements is also examined. In Chapter 4, correlations between cluster mass scatters from different measurement techniques are analyzed in the same simulation used for the study in Chapter 3. The physical causes of the correlations are also discussed, extending the results found in Chapter 3.

Chapter 2

Reconstructing baryon oscillations

The baryon acoustic oscillation (BAO) method for constraining the expansion history is adversely affected by non-linear structure formation, which washes out the correlation function peak created at decoupling. To increase the constraining power of low z BAO experiments, it has been proposed that one use the observed distribution of galaxies to "reconstruct" the acoustic peak. Recently Padmanabhan, White & Cohn provided an analytic formalism for understanding how reconstruction works within the context of Lagrangian perturbation theory. We extend that formalism to include the case of biased tracers of the mass in real space and, because the quantitative validity of LPT is questionable, we investigate reconstruction in N-body simulations. We find that LPT does a good job of explaining the trends seen in simulations for both the mass and for biased tracers in real space and comment upon the implications this has for reconstruction. [1]

2.1 Reconstructing baryon oscillations: Introduction

It has been known for many years that the coupling of photons and baryons in the early universe results in significant features in the matter power spectrum (Peebles & Yu 1970; Sunyaev & Zeldovich 1970; Doroshkevich et al. 1978). Prior to recombination, photons and baryons are tightly coupled and are well approximated by a fluid. Perturbations during this epoch do not grow, but instead excite sound waves which get frozen at recombination and manifest themselves as an almost harmonic series of peaks in the power spectrum, $P(k)$, or equivalently a narrow feature in the correlation function, $\xi(r)$ (see Eisenstein & Hu (1998); Meiksin et al. (1999) for a detailed description of the physics in modern cosmologies and Eisenstein et al. (2007b) for a comparison of Fourier and configuration space pictures). These so-called "baryon acoustic oscillations" (BAO) can be used as a standard ruler to measure the expansion rate of the Universe, making the method an integral part of current

[1] This chapter has been previously published as Noh et al. (2009), and is reproduced with the permission of all coauthors and the copyright holder. Copyright 2009 American Physical Society.

and next-generation dark energy experiments.

While the early Universe physics is linear and well understood, the low redshift observations are complicated by the non-linear evolution of matter, galaxy bias and redshift space distortions. The non-linear evolution leads to a coupling of k-modes and damping of the oscillations on small scales (Meiksin et al. 1999) and a small shift in their positions (Eisenstein et al. 2007b; Crocce & Scoccimarro 2008; Matsubara 2008a; Seo et al. 2008; Padmanabhan & White 2009). The damping of the linear power spectrum (or equivalently the smoothing of the correlation function) reduces the contrast of the feature and the precision with which the size of ruler may be measured.

In Eisenstein et al. (2007b) it was pointed out that much of the modification to the power spectrum comes from bulk flows and super-cluster formation. Since these large-scale flows are reasonably well measured by the survey, their effects can, in principle, be corrected. In Eisenstein et al. (2007a) a method was introduced for removing the non-linear degradation of the acoustic signature, sharpening the feature in configuration space or restoring/correcting the higher k oscillations in Fourier space; this method has been tested on simulations by a number of groups (Eisenstein et al. 2007a; Huff et al. 2007; Wagner et al. 2008). However, this method is inherently non-linear and therefore difficult to understand analytically. A study of this problem for the matter density using Lagrangian perturbation theory (Padmanabhan et al. 2009) explained how the method "reconstructed" the BAO feature, but also pointed out that it did not reconstruct the linear density field. We extend these results here - (i) generalizing the analytic theory to biased tracers, including explicit expressions for the reconstructed power spectrum to second order in the linear power spectrum, and (ii) testing the validity of the analytic expressions with a suite of N-body simulations. Throughout we shall work in real, as opposed to redshift, space in order to highlight the physics. The generalization to redshift space is in principle possible within the context of Lagrangian perturbation theory, but would require further development, and models for treating e.g. fingers of god.

We compare the analytic theory to a set of 1024^3 particle simulations run in periodic, cubical boxes of side length $2\,h^{-1}$Gpc with a *TreePM* code (White 2002). The simulations were initialized at $z = 100$ using second order Lagrangian perturbation theory, and the phase space information for all of the particles was dumped at $z = 0$, 0.3, 0.7 and 1.0. Multiple realizations, with different initial density fields, were run for each cosmology to reduce sampling effects (more details can be found in Carlson et al. (2009); Padmanabhan & White (2009)). In addition to the dark matter particle data, halo catalogs were produced for each output using the friends-of-friends method (Davis et al. 1985) with a linking length of 0.168 times the mean inter-particle spacing. We work with halos above $10^{13}\,h^{-1}M_\odot$, i.e. containing more than 20 particles.

We investigate one of the cosmologies considered in Carlson et al. (2009); Padmanabhan & White (2009): ΛCDM, with $\Omega_M = 0.25$, $\Omega_B = 0.04$, $h = 0.72$, $n = 0.97$ and $\sigma_8 = 0.8$. This is close to the current "best fit" cosmology and will serve as a realistic model to explore. Within this cosmology the acoustic peak in the correlation function is at $\sim 110\,h^{-1}$Mpc,

with an intrinsic width set by the diffusion (Silk) damping scale of $\sim 10\,h^{-1}$Mpc.

2.2 Reconstruction I: Matter

We begin our investigation of reconstruction by considering the most conceptually simple case: reconstruction of the acoustic peak in the matter 2-point function. We start by reviewing the reconstruction algorithm of Eisenstein et al. (2007a) and its interpretation within Lagrangian perturbation theory (Padmanabhan et al. 2009), and then compare its predictions with simulations. The following section extends this analysis to biased tracers.

2.2.1 Algorithm

The algorithm devised by Eisenstein et al. (2007a) is straightforward to apply to a simulation and consists of the following steps:

- Smooth the density field to filter out high k modes, which are difficult to model.
- Compute the negative Zel'dovich displacement, $\mathbf{s}$, from the smoothed density field: $\mathbf{s}(\mathbf{k}) = -i(\mathbf{k}/k^2)\delta(\mathbf{k})\mathcal{S}(k)$, where $\mathcal{S}$ is the smoothing kernel (see below).
- Move the original particles by $\mathbf{s}$ and compute the "displaced" density field, δ_d.
- Shift an initially spatially uniform distribution of particles by $\mathbf{s}$ to form the "shifted" density field, δ_s.
- The reconstructed density field is defined as $\delta_r \equiv \delta_d - \delta_s$ with power spectrum $P_r(k) \propto \langle|\delta_r^2|\rangle$.

Following Eisenstein et al. (2007a) we use a Gaussian smoothing of scale R, specifically

$$\mathcal{S}(k) = e^{-(kR)^2/2} \quad . \tag{2.1}$$

We take advantage of the periodicity of the simulations to perform all of these steps using fast Fourier transforms. The density fields are constructed from the particle positions using a CIC assignment (Hockney & Eastwood 1988).

Fig. 2.1 shows an example of reconstruction, for the ΛCDM model. By $z = 0$ non-linear evolution has partially washed out the peak in the matter correlation function (solid line). However applying reconstruction with $R = 5$ or $10\,h^{-1}$Mpc restores much of the original signal. Fig. 2.2 shows reconstruction at the level of the density fields, for a thin slice through a piece of one of our simulations centered on a halo of mass $4 \times 10^{14}\,h^{-1}M_\odot$. We see that reconstruction has 'reversed' the formation of collapsed structures, and yields a field that is visually similar to the initial density field. Note the final field has sharper, more pronounced peaks than either the initial or reconstructed density fields, though the reconstructed field still has more prominent peaks than the initial field.

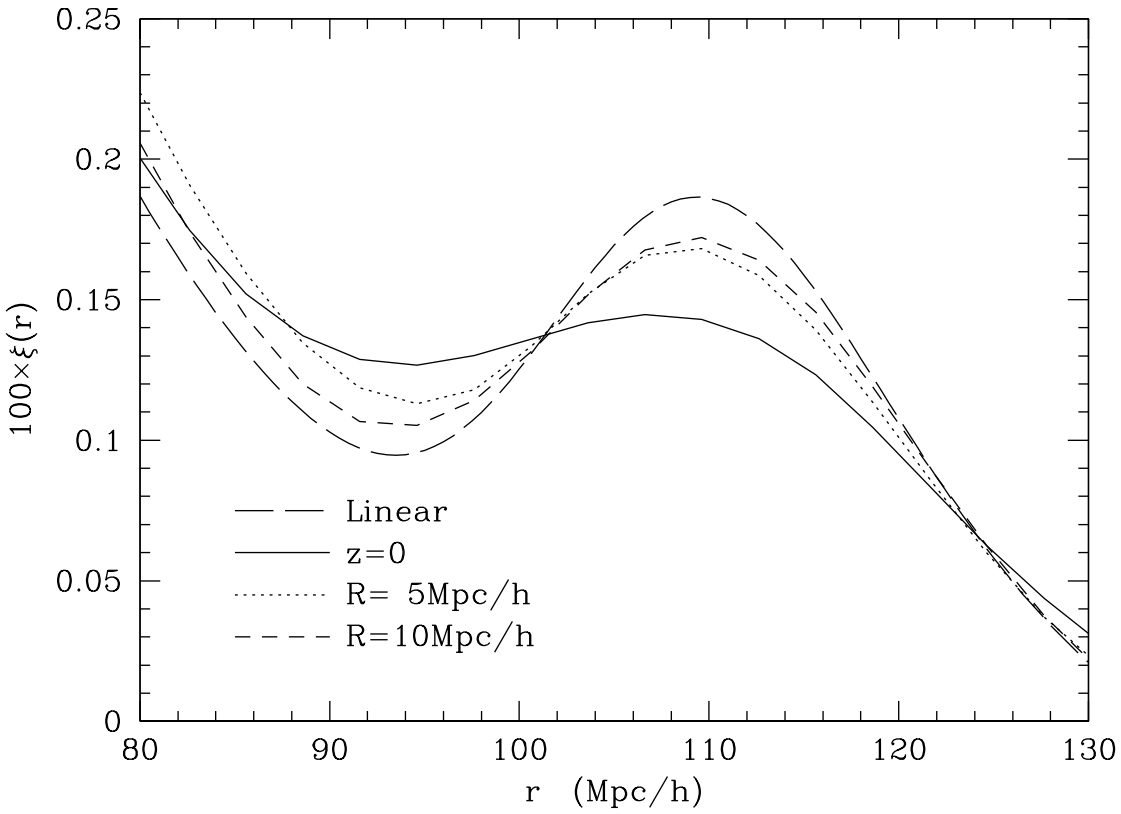

Figure 2.1: The mass correlation function for our ΛCDM model at $z = 0$ before (solid) and after reconstruction using a smoothing of $R = 5\,h^{-1}$Mpc (dotted) and $R = 10\,h^{-1}$Mpc (short dashed). Non-linear evolution has partially erased the peak in the initial conditions (long-dashed) by $z = 0$, but it is somewhat restored by reconstruction.

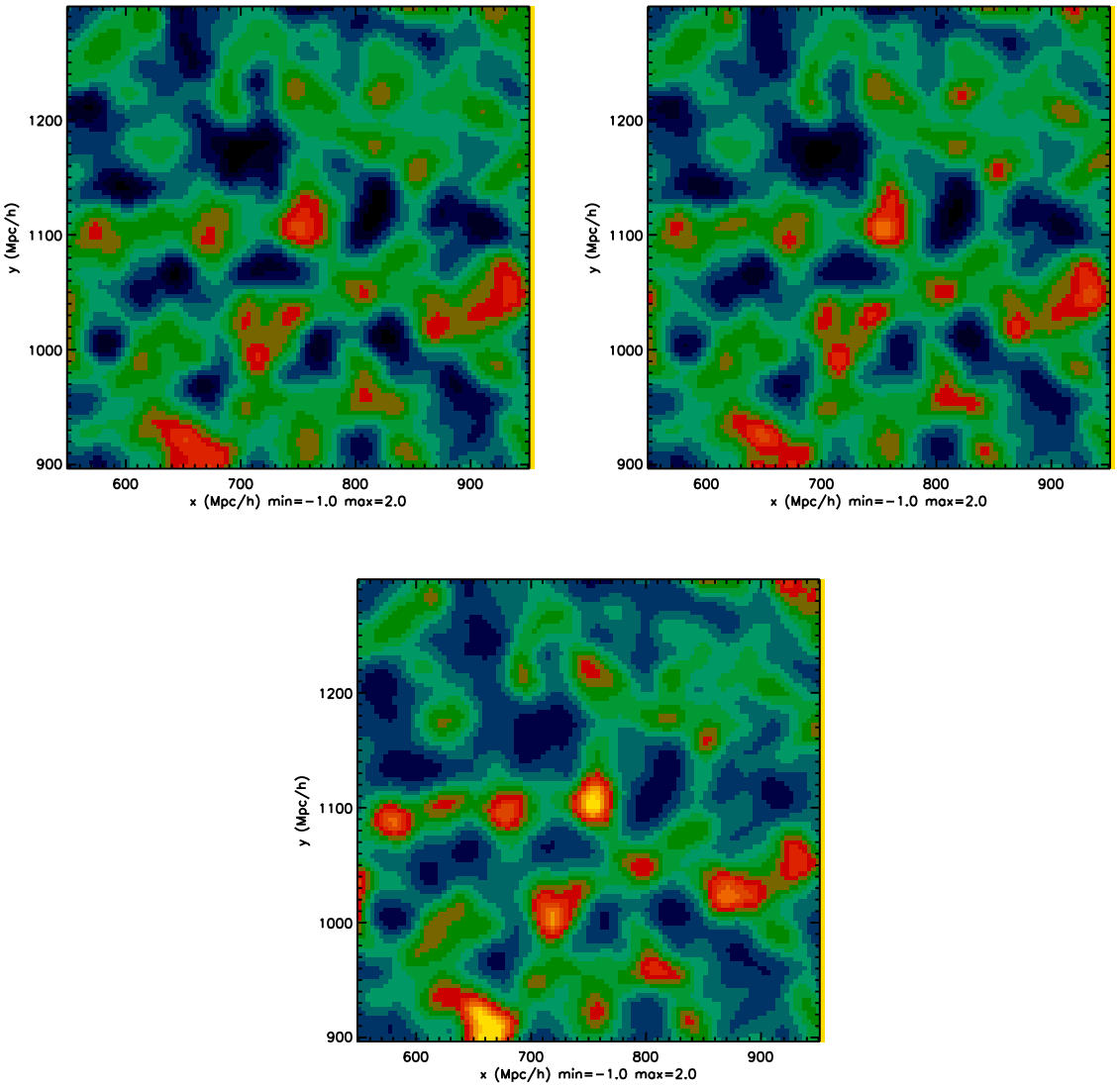

Figure 2.2: A thin slice through a simulation showing the initial (top), reconstructed (middle) and final (bottom) density fields all smoothed with a Gaussian of $10\,h^{-1}$Mpc. Each slice is centered on the (final) position of a halo of mass $4 \times 10^{14}\,h^{-1}M_{\odot}$. Note the final field has sharper, more pronounced peaks than either the initial or reconstructed density fields, though the reconstructed field still has more prominent peaks than the initial field.

	$z=0$				$z=1$			
	Shifted		Displaced		Shifted		Displaced	
R	Sim	1LPT	Sim	1LPT	Sim	1LPT	Sim	1LPT
5	5.82	5.39	3.35	1.95	3.76	3.41	2.16	1.23
10	4.92	4.80	3.40	2.80	3.20	3.04	2.19	1.77
15	4.39	4.34	3.72	3.36	2.85	2.75	2.38	2.13
20	3.99	3.97	4.00	3.77	2.59	2.52	2.56	2.38
25	3.67	3.67	4.24	4.07	2.39	2.32	2.71	2.58
30	3.40	3.41	4.45	4.32	2.21	2.16	2.84	2.73

Table 2.1: The rms displacements of the "shifted" and "displaced" particles at $z = 0$ and $z = 1$ as a function of the smoothing scale R. First order LPT correctly predicts the observed displacements (at the 10% level), with the agreement improving as the smoothing scale increases.

2.2.2 Lagrangian perturbation theory

Reconstruction naturally lends itself to a description in term of Lagrangian perturbation theory, which we briefly review here. The Lagrangian description of structure formation (Buchert 1989; Moutarde et al. 1991; Hivon et al. 1995) relates the current (or Eulerian) position of a mass element, $\mathbf{x}$, to its initial (or Lagrangian) position, $\mathbf{q}$, through a displacement vector field $\mathbf{\Psi}(\mathbf{q})$,

$$\mathbf{x} = \mathbf{q} + \mathbf{\Psi}(\mathbf{q}) \,. \tag{2.2}$$

The displacements can be related to overdensities by Taylor & Hamilton (1996)

$$\delta(\mathbf{k}) = \int d^3q \; e^{-i\mathbf{k}\cdot\mathbf{q}} \left(e^{-i\mathbf{k}\cdot\mathbf{\Psi}(\mathbf{q})} - 1\right) \quad . \tag{2.3}$$

Analogous to Eulerian perturbation theory, LPT expands the displacement in powers of the linear density field, δ_L,

$$\mathbf{\Psi} = \mathbf{\Psi}^{(1)} + \mathbf{\Psi}^{(2)} + \cdots \,, \tag{2.4}$$

with $\mathbf{\Psi}^{(n)}$ being $n^{\rm th}$ order in δ_L. First order in LPT is equivalent to the well-known Zel'dovich approximation.

In the simulations the rms ($1D$) displacement goes from 6.1 h^{-1}Mpc at $z = 0$ to 3.9 h^{-1}Mpc at $z = 1$, in excellent agreement with the expectations of the Zel'dovich approximation. In fact the Zel'dovich rms displacements match those measured in the simulations at the percent level, better than we would expect given the size of the second order corrections.

Using Eq. (2.3) the power spectrum is

$$P(k) = \int d^3q \; e^{-i\mathbf{k}\cdot\mathbf{q}} \left(\left\langle e^{-ik_i\Delta\Psi_i(\mathbf{q})}\right\rangle - 1\right) \,, \tag{2.5}$$

where $\mathbf{q} = \mathbf{q}_1 - \mathbf{q}_2$, and $\Delta\mathbf{\Psi} = \mathbf{\Psi}(\mathbf{q}_1) - \mathbf{\Psi}(\mathbf{q}_2)$. Expanding the exponential in powers of $\mathbf{\Psi}$ and using Eq. (2.19) reproduces the results of "standard" perturbation theory. However, following Matsubara (2008a), if we use the cumulant expansion theorem to expand the exponential and expand the resulting powers of $\mathbf{k} \cdot \Delta\mathbf{\Psi}$ using the binomial theorem we have two types of terms: those where the $\mathbf{\Psi}$ are all evaluated at the same point (which we can take to be the origin) and the rest. Leaving the first set of terms exponentiated while expanding the second set of terms in powers of $\mathbf{\Psi}$, we find

$$P(k) = e^{-k^2\Sigma^2/2} \{P_L(k) + \cdots\} \tag{2.6}$$

where $P_L(k)$ is the linear theory power spectrum, Σ is proportional to the rms Zel'dovich displacement (i.e. final minus initial particle positions to linear order)

$$\Sigma^2 = \frac{1}{3\pi^2} \int dq \; P_L(p) \tag{2.7}$$

and explicit expressions for the higher order terms may be found in Matsubara (2008a) and Appendix 2.A. The exponential prefactor describes the broadening of the acoustic peak seen in Fig. 2.1, some of the additional terms lead to a slight change in the peak position (Crocce & Scoccimarro 2008; Padmanabhan et al. 2009; Padmanabhan & White 2009). The rms displacement of an individual particle is $\Sigma/\sqrt{2}$.

The effects of the exponential prefactor are most easily seen by considering the correlation function. Furthermore, Lagrangian perturbation theory, like several other perturbation theory schemes, performs better at predicting the large-scale correlation function than the power spectrum, since it fails to accurately predict broad-band power which contributes at small r (Matsubara 2008a; Padmanabhan & White 2009). For these reasons, we shall present most of our comparisons between theory and simulation in configuration space, i.e. we shall present

$$\xi(r) = \int \frac{d^3k}{(2\pi)^3} \; P(k) j_0(kr) = \int \frac{dk}{k} \; \Delta^2(k) j_0(kr) \tag{2.8}$$

with $j_0(x) = \sin(x)/x$ the spherical Bessel function of order zero. This comparison also has the advantage of more clearly emphasizing the acoustic feature, which can be easily seen as a single peak in $\xi(r)$ at $r \sim 110\,h^{-1}$Mpc. For presentation purposes we have smoothed all of the correlation functions by $3\,h^{-1}$Mpc before plotting them – this reduces high frequency noise in the N-body simulations but has a minimal impact on the shape of the curves since this smoothing adds in quadrature to the $\sim 10\,h^{-1}$Mpc intrinsic width of the features. Observationally one could achieve similar effects by using broad but overlapping r bins.

A second interesting statistic is the cross-spectrum between the linearly evolved initial field, δ_L and the fully evolved final field, δ_f,

$$G_f(k) \equiv \frac{\langle \delta_L(k) \delta_f^\star(k) \rangle}{P_L} \quad , \tag{2.9}$$

sometimes referred to as the propagator (Crocce & Scoccimarro 2008). The relevant physics in this case is more cleanly visualized in Fourier space, since it shows the decorrelation between the initial field and the processed field which becomes a convolution in configuration space. Fits to numerical simulations (Eisenstein et al. 2007b) and a variety of analytic arguments (Bharadwaj 1996; Eisenstein et al. 2007b; Crocce & Scoccimarro 2008; Matsubara 2008a; Seo et al. 2008; Padmanabhan et al. 2009; Padmanabhan & White 2009), including Lagrangian perturbation theory, suggest that

$$G_f(k) \simeq e^{-(k\Sigma)^2/4} + \cdots \tag{2.10}$$

i.e. that the damping is half as strong as in the power spectrum (see Appendix 2.A for expressions beyond leading order).

It is straightforward to repeat these steps for the reconstructed field (Padmanabhan et al. 2009). We assume that the density field is smoothed on a large enough scale that $\mathbf{s}$ can be approximated as $\mathbf{s} = -i(\mathbf{k}/k^2)\delta_L(\mathbf{k})\mathcal{S}(k)$. We can then compare the three contributions to the power spectrum (P_{ss}, P_{dd} and P_{sd}) to get the reconstructed power spectrum (Padmanabhan et al. 2009)

$$\begin{aligned} P_r(k) &= \Big\{ e^{-k^2\Sigma_{ss}^2/2}\mathcal{S}^2(k) \\ &\quad +2e^{-k^2\Sigma_{sd}^2/2}\mathcal{S}(k)\bar{\mathcal{S}}(k) \\ &\quad + e^{-k^2\Sigma_{dd}^2/2}\bar{\mathcal{S}}^2(k)\Big\} P_L(k) + \ldots \end{aligned} \tag{2.11}$$

where $\bar{\mathcal{S}} \equiv 1 - \mathcal{S}$, and as before, the higher order terms are Appendix 2.A. There are now three smoothing terms, (Σ_{ss}, Σ_{dd} and Σ_{sd}) defined by

$$\Sigma_{ss}^2 \equiv \frac{1}{3\pi^2}\int dq\ P_L(p)\mathcal{S}^2(p)\,, \tag{2.12}$$

$$\Sigma_{dd}^2 \equiv \frac{1}{3\pi^2}\int dq\ P_L(p)\bar{\mathcal{S}}^2(p)\,, \tag{2.13}$$

and $\Sigma_{sd}^2 = (\Sigma_{ss}^2 + \Sigma_{sd}^2)/2$ (see Table 2.1). As pointed out in Padmanabhan et al. (2009), all of these smoothing scales are smaller than the nonlinear smoothing Σ, explaining why the acoustic feature is sharpened after reconstruction. A related calculation (see Appendix 2.A) yields the propagators

$$G_f = e^{-k^2\Sigma^2/4} + \ldots \tag{2.14}$$

$$G_d = e^{-k^2\Sigma_{dd}^2/4}\ \bar{\mathcal{S}} + \ldots \tag{2.15}$$

$$G_s = e^{-k^2\Sigma_{ss}^2/4}\ [-\mathcal{S}] + \ldots \tag{2.16}$$

$$G_r \equiv G_d - G_s \quad , \tag{2.17}$$

with the higher order terms in the Appendix.

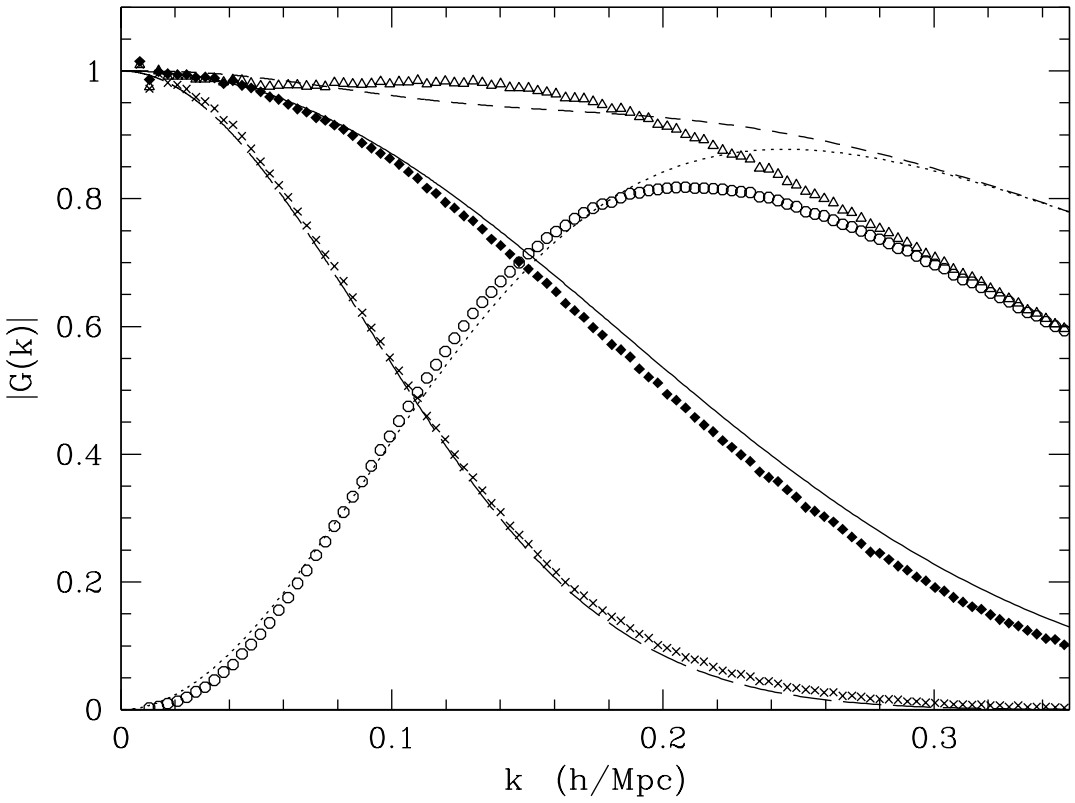

Figure 2.3: The cross-correlation between the linearly evolved initial field and the fully evolved final field, displaced field, shifted field and the reconstructed field for ΛCDM at $z = 0$ (see text). The points show the results of N-body simulations while the lines show the predictions from Lagrangian perturbation theory (Padmanabhan et al. 2009). The solid line and diamonds represent $G_f(k)$, the dotted line and circles represent $G_d(k)$, long-dashed line and crosses represent $G_s(k)$ and short-dashed line and triangles represent $G_r(k)$. We have used a smoothing of $R = 10\,h^{-1}\,\mathrm{Mpc}$.

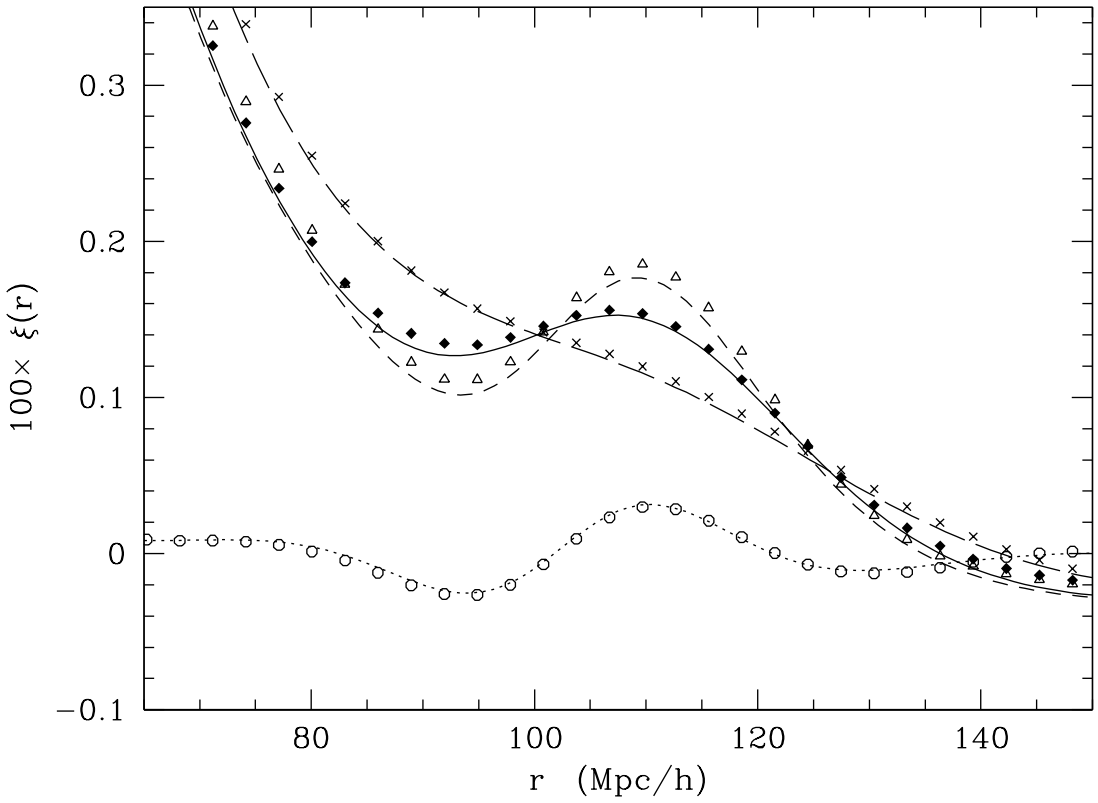

Figure 2.4: The correlation functions of the fully evolved final, displaced, shifted, and reconstructed mass fields for ΛCDM at $z = 0$ (see text). As in Fig. 2.3 the points show the results of N-body simulations while the lines show the predictions from Lagrangian perturbation theory (Padmanabhan et al. 2009). Solid line and diamonds represent ξ_f, dotted line and circles represent ξ_d, long-dashed line and crosses represent ξ_s, and short-dashed line and triangles represent ξ_r. We have used a smoothing of $R = 10\,h^{-1}\,\mathrm{Mpc}$.

2.2.3 Comparison with simulations

To begin we compare the predictions of perturbation theory for the propagator to calculations of the same quantity in N-body simulations. This isolates the damping behavior from the mode-coupling (Padmanabhan & White 2009). Fig. 2.3 shows the different contributions to the reconstructed propagator. The theoretical predictions for G_f are in reasonably good agreement with the results, with the theory showing slightly weaker damping than the simulations. (Small changes to the theoretically predicted Σ can bring the results into much better agreement, but we will not make such *ad hoc* changes here.) The agreement is similar for the pieces of the reconstructed propagator. For $k < 0.15\,h\,\mathrm{Mpc}^{-1}$, with $\Delta^2 \simeq 0.5$, the simulation and theory agree to better than 4% for G_f, G_d, G_s and G_r. The simulations show that the reconstructed field retains better memory of its initial conditions ($G_r \approx 1$) at intermediate scales than LPT predicts, with perturbation theory giving too much power at high k. The over-prediction at high k is not of particular concern, since at these scales the dimensionless power exceeds unity and we would expect perturbation theory to be breaking down. Out to $k \simeq 0.2\,h\,\mathrm{Mpc}^{-1}$, where $\Delta^2 \sim 1$, perturbation theory agrees with the simulations at the better than 10% level! We emphasize that this level of agreement comes from the inclusion of the 2$^{\mathrm{nd}}$ order contributions, with the dominant correction coming from the R_1 term (see Appendix 2.A).

Fig. 2.4 shows the corresponding figure for the correlation functions, broken down into the same components. Note the excellent agreement for the displaced and shifted fields, and good agreement for the final and reconstructed fields. At $r \simeq 110\,h^{-1}\mathrm{Mpc}$ the simulated and theoretical ξ agree to about 5% for all components, with the agreement on ξ_f being 2%. In this figure the level of agreement between ξ_f and the theory appears worse than the comparable figure in Matsubara (2008b). This is most likely due to the lower redshift and different cosmology we have chosen (see also Carlson et al. (2009)). The sense of the disagreement in both ξ_f and ξ_r is the same however, indicating that the Lagrangian perturbation theory of reconstruction is working better in a differential than absolute sense. As above, a small change in the relevant Σ could slightly improve the agreement with simulations, which may argue for leaving Σ as a free parameter when fitting to data. We will not pursue such modifications further here.

2.3 Reconstruction II: Biased tracers

Unfortunately we don't directly measure the mass field in galaxy surveys, we measure the distribution of biased tracers. Here we investigate how the biasing of the tracers affects reconstruction. Rather than attempt a 'realistic' galaxy model, we shall concentrate on mass limited samples of halos when comparing LPT to the simulations. None of the essential aspects are lost with this simplification.

Reconstruction assumes that we can estimate the appropriate shifts from our smoothed, biased, density field. This requires that the smoothed halo field be a multiple of the smoothed

mass field with known constant of proportionality (the bias). In the simulations we estimate the bias from the $k \approx 0$ limit of the propagator, in observations it would need to be determined in a different manner.

If we keep the denominator in Eq. (2.9) as the linear mass power spectrum, the lowest order modification to the propagator is to multiply by the linear bias of the tracer. The gross shape of $G(k)$ is unaltered, since the exponential damping is unchanged, being generated by the velocities which are sourced by the mass field not the halo field. At higher order, the cross terms between the linear and nth order terms are modified and introduce an additional dependence on the bias (Matsubara 2008b), as shown in Fig. 2.5. LPT predicts that the halo propagator falls slightly more slowly to high k than the mass propagator and the decline is slower the higher the mass threshold. This means that the halo propagator departs more from the Gaussian form than the mass propagator. It is possible that this is related to the special locations in the velocity field that rare, highly biased peaks occupy (e.g. Bardeen et al. (1986); Percival & Schäfer (2008)). However, the difference is small, as shown explicitly in Fig. 2.5.

Fig. 2.6 shows the different propagators for halos more massive than $10^{13}\,h^{-1}M_\odot$ in the simulations and in theory. As was the case for the mass, the asymptote at high k is not well determined by the theory but the agreement at low k is quite good. G_s is the same as for the mass, and again the agreement between simulation and theory is good. The match between simulations and theory for G_f is quite good. Perturbation theory is correctly predicting the low k asymptote of G_d, which is no longer zero but $b-1$, though it doesn't match the shape as well as for the mass. Once more the N-body simulations predict a G_r which increases slightly at intermediate k and is above the theory for $k \simeq 0.1 - 0.2\,h\,\mathrm{Mpc}^{-1}$.

To lowest order (see Appendix 2.A for 2nd order contributions) the reconstructed field has

$$\begin{aligned} P_r^{(0)}(k) &= P_L(k)\Big\{e^{-k^2\Sigma_{ss}^2/2}\mathcal{S}^2(k) \\ &\quad +2e^{-k^2\Sigma_{sd}^2/2}\left[\mathcal{S}(k)\bar{\mathcal{S}}(k)+(b-1)\mathcal{S}(k)\right] \\ &\quad +e^{-k^2\Sigma_{dd}^2/2}\left[\bar{\mathcal{S}}^2(k)+2(b-1)\bar{\mathcal{S}}(k)+(b-1)^2\right]\Big\} \end{aligned} \tag{2.18}$$

which reduces to Eq. (2.11) in the limit $b \to 1$. Note that $P_r^{(0)}(k) \to b^2 P_L(k)$ as $k \to 0$, as expected, and $P_r^{(0)}(k) \to b^2 P_L(k)\exp[-k^2\Sigma^2/2]$ in the limit that $\Sigma_{ss} = \Sigma_{dd} = \Sigma_{sd}$.

Fig. 2.7 shows how well this expression, plus the 2nd order contributions, matches the simulations. As with Fig. 2.4, the agreement is overall quite good, slightly better than for the mass in the case of ξ_f and ξ_r. As in that case, a slight increase in the Σ can improve the agreement somewhat, but we have left the theoretical predictions unchanged. For ξ_f the agreement near the acoustic peak is better than 2%, for ξ_r it is better than 1% and for ξ_s and ξ_d it is 5% and 2% respectively.

Just as with the matter field, the smearing of the acoustic peak is reduced by reconstruction. In fact there is relatively little difference between the biased and unbiased tracers in this respect.

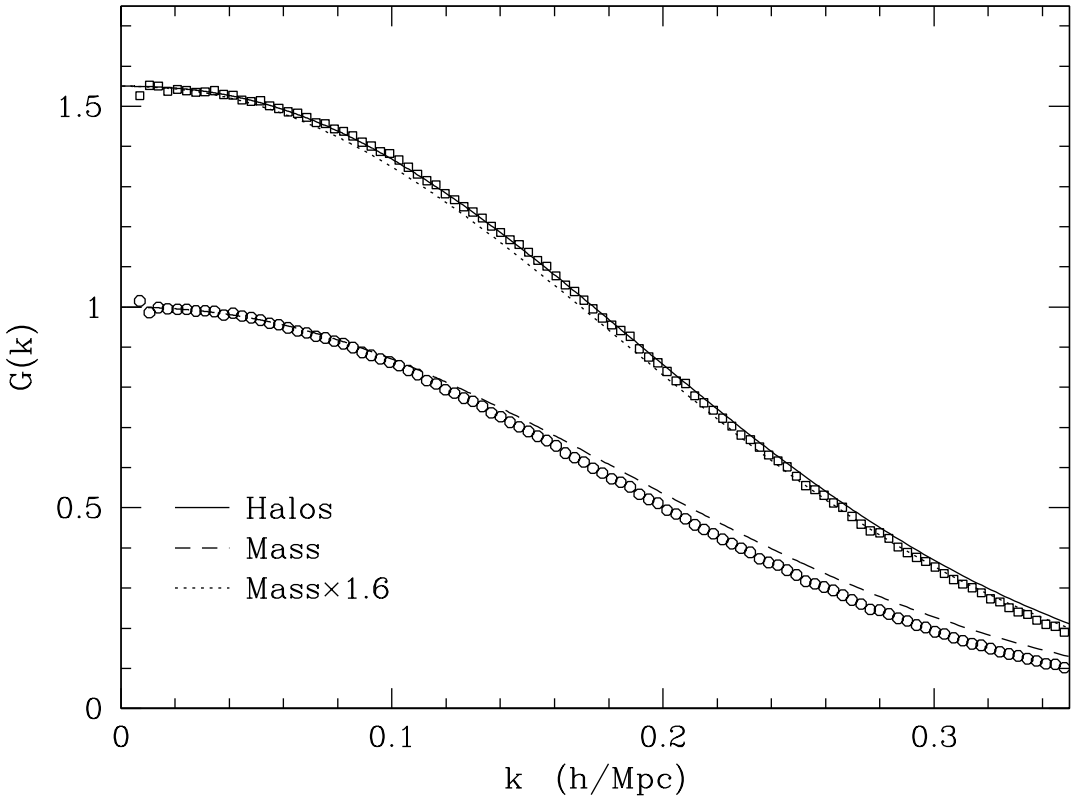

Figure 2.5: The cross-correlation between the linearly evolved initial field and the fully evolved final field for the mass (dashed line and circles) and for halos above $10^{13}\,h^{-1}M_\odot$ (solid line and squares) in ΛCDM at $z = 0$. The dotted line shows the mass propagator multiplied by $b \simeq 1.6$.

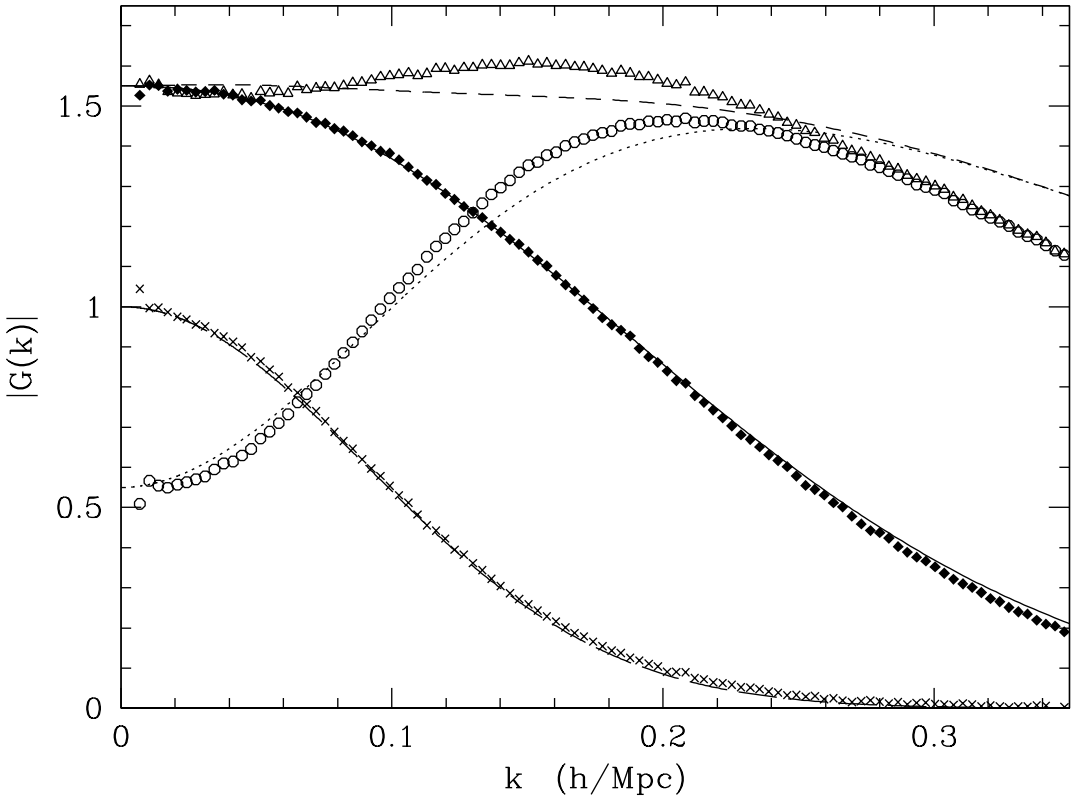

Figure 2.6: The cross-correlation between the linearly evolved initial field and the evolved, displaced, shifted and reconstructed fields for halos above $10^{13}\,h^{-1}M_{\odot}$. Diamonds and the solid line show the final field, crosses and the long-dashed line the shifted field, circles and the dotted line the displaced field and the triangles and short-dashed line the reconstructed field.

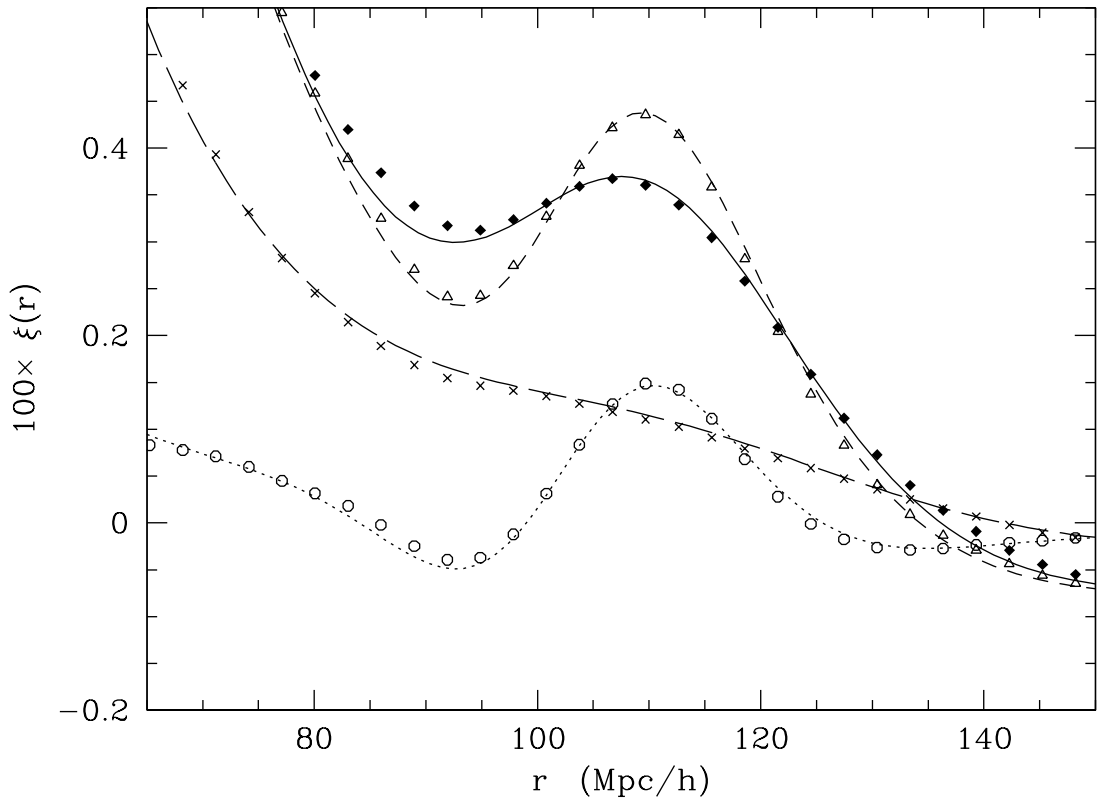

Figure 2.7: The correlation functions for the evolved, displaced, shifted and reconstructed fields for halos above $10^{13}\,h^{-1}M_{\odot}$. Diamonds and the solid line show the final field, crosses and the long-dashed line the shifted field, circles and the dotted line the displaced field and the triangles and short-dashed line the reconstructed field.

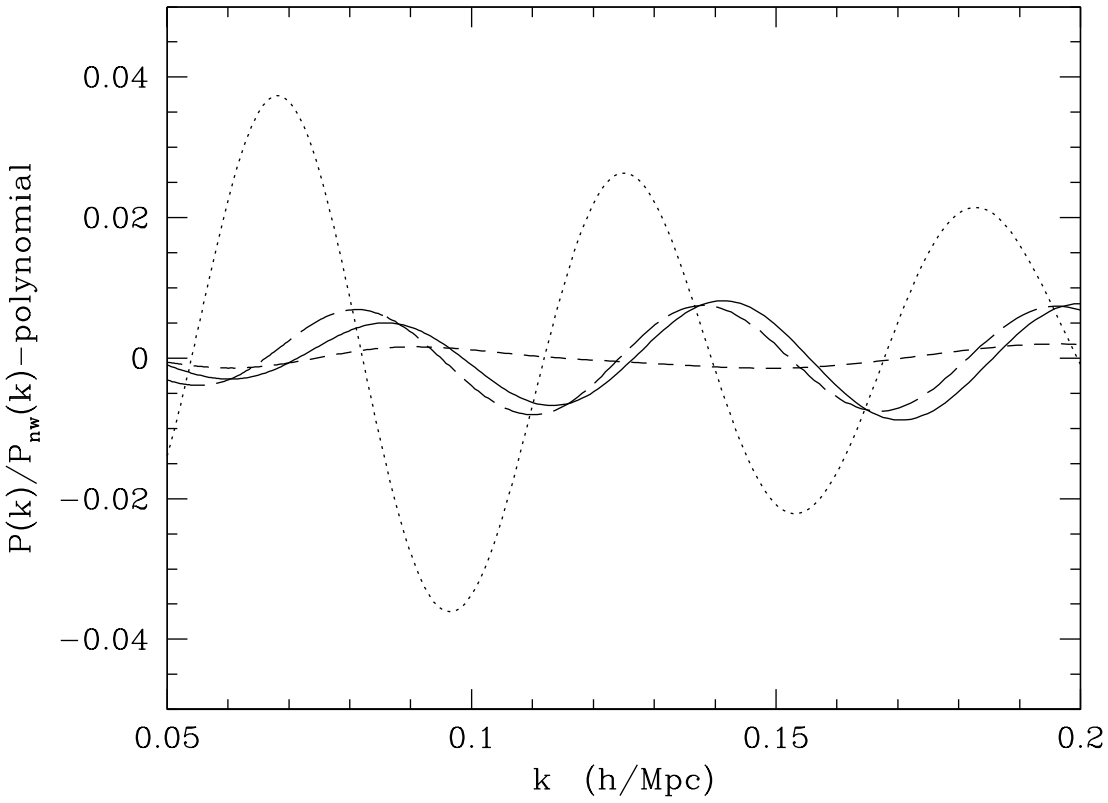

Figure 2.8: The out-of-phase pieces of the power spectrum of halos more massive than $10^{13}\,h^{-1}M_\odot$ as predicted by perturbation theory. To emphasize the oscillations, each spectrum has been divided by the "no wiggle" form of Eisenstein & Hu (1998) and has had a $4^{\rm th}$ order polynomial (in k) subtracted. The dotted line shows the linear theory (divided by 2). The solid line is the out-of-phase or mode-coupling pieces of P_f, which can be compared to $dP_L/d\ln k$ (long-dashed line) (Padmanabhan & White 2009). The short-dashed line shows that reconstruction reduces the amplitude of the out-of-phase terms and hence the change in the location of the acoustic peak in $\xi(r)$.

2.4 Change in the peak location

The above sections demonstrate that the LPT provides a good description of how reconstruction reduces the smoothing of the acoustic feature, both for the dark matter and halos. Recent simulations (Seo et al. 2008) have also found that reconstruction corrects the $\sim 0.5\%$ change in the acoustic scale caused by nonlinear evolution. It is therefore interesting to see how this is manifest within Lagrangian perturbation theory.

In perturbation theory the change in the acoustic peak location comes about because there are second-order corrections to $P(k)$ which are out-of-phase with the linear theory oscillations (Eisenstein et al. 2007b; Crocce & Scoccimarro 2008; Matsubara 2008a; Seo et al. 2008; Padmanabhan et al. 2009). The out-of-phase component is quite similar to the derivative of P_L so, by Taylor's theorem, this addition is akin to a change in the characteristic frequency of the oscillation. We consider the analogous terms for the reconstructed power spectrum below, in order to explain how reconstruction suppresses such changes.

These out-of-phase components come about because of the structure of the mode-coupling terms (the Q_n in the notation of Appendix 2.A and Matsubara (2008b)), and this structure is modified by reconstruction in such a way as to reduce the amplitude of the out-of-phase contribution (Padmanabhan et al. 2009). Figure 2.8 shows the out-of-phase terms, with the broad-band shape removed to focus on the oscillatory structure, compared to the in-phase acoustic signature in the linear theory. Note that the modification of the mode-coupling terms detailed in the Appendix drastically reduces the amplitude of the out-of-phase terms in the reconstructed spectrum, and hence the change in the acoustic scale. This explains why the change in the peak location seen in simulations is reduced by reconstruction.

2.5 Reconstructing baryon oscillations: Discussion

Acoustic oscillations in the photon-baryon fluid prior to decoupling leave an imprint both in the cosmic microwave background anisotropy power spectrum and the matter power spectrum. A comparison of these features at different redshifts provides one of the most promising routes to constraining the expansion history of the Universe. Unfortunately at low redshift, where the accelerated expansion of the Universe is strongest, non-linearities wash out much of the acoustic information.

Recently the authors of Eisenstein et al. (2007a) proposed a method for recovering much of the lost information, or reconstructing the acoustic peak. Unfortunately, the method is inherently non-linear and therefore difficult to understand analytically. A study of this problem in Lagrangian perturbation theory (Padmanabhan et al. 2009), for the mass field, shed some light on how the algorithm resulted in tighter constraints on the acoustic scale, but the quantitative validity of Lagrangian perturbation theory is questionable (see e.g. Carlson et al. (2009) for a recent survey) and we typically study biased tracers of the mass.

We have validated and extended the analytic insights developed in Padmanabhan et al. (2009), computing a variety of statistics of both the mass density field and the dark matter

halo density field using Lagrangian perturbation theory which we then we then compare to the same quantities measured in a large suite of N-body simulations. We work throughout in real space.

As emphasized in Padmanabhan et al. (2009), reconstruction does not generate the initial power spectrum or correlation function, but it does serve to sharpen the peak and reduce the change in the peak location associated with non-linearity. We demonstrate explicitly that both of these points remain true for biased tracers. The amount by which the non-linear smearing is reduced is comparable for biased tracers and for the mass, since it is generated by bulk flows which are sourced by the mass density independent of the form of the tracer. The fact that peaks form in special locations in the density field appears to have a very small effect. The reduction in the peak location change due to reconstruction is at least as dramatic for biased tracers as for the mass, with the out-of-phase component responsible for the change being reduced in amplitude by the process of reconstruction. A discussion of by how much the peak position changes depends on a detailed description of the fitting methodology and the sample under consideration, but if we model the observed spectra as in Padmanabhan & White (2009) we find that reconstruction reduces the position change by a factor of $2-4$ for moderately biased tracers like those investigated here. Since in the relevant range of redshift and bias the shift in the peak was already below the level of uncertainty of upcoming measurements and only of relevance for next-generation experiments, this further reduction renders the shift essentially irrelevant.

We conclude that Lagrangian perturbation theory, while not perfect, provides a good framework for thinking about reconstruction. It explains in a natural way how reconstruction works, and how it achieves a reduction in the smearing and position of the acoustic peak generated by non-linear evolution. The predictions of LPT agree to within several percent with the results of N-body simulations on the large scales most relevant to acoustic oscillations, for both biased and unbiased tracers. While not shown explicitly in figures here, perturbation theory becomes an increasingly good description of the simulations at higher redshift, though the need for reconstruction beyond $z \simeq 1$ is greatly reduced.

2.A Appendix: Beyond leading order

Lagrangian perturbation theory allows us to compute corrections to the lowest order expressions for $P(k)$ and $G(k)$ listed in the text. Here we give the $2^{\rm nd}$ order contributions, following Matsubara (2008a,b) and Padmanabhan & White (2009). The notation and procedure is borrowed heavily from these works, to which we refer the reader for more details.

Recall that the displacement is expanded in powers of the linear density contrast, δ_L, as

Bouchet et al. (1995)

$$\begin{aligned}\boldsymbol{\Psi}^{(n)}(\mathbf{k}) &= \frac{i}{n!}\int\prod_{i=1}^{n}\left[\frac{d^3k_i}{(2\pi)^3}\right] \\ &\times \quad (2\pi)^3\delta^{(D)}\left(\sum_i \mathbf{k}_i - \mathbf{k}\right) \\ &\times \quad \mathbf{L}^{(n)}(\mathbf{k}_1,\cdots,\mathbf{k}_n,\mathbf{k})\delta_L(\mathbf{k}_1)\cdots\delta_L(\mathbf{k}_n)\ . \end{aligned} \tag{2.19}$$

where the $\mathbf{L}^{(n)}$ have closed form expressions, generated by recurrence relations. For example,

$$\mathbf{L}^{(1)} = \frac{\mathbf{k}}{k^2} \tag{2.20}$$

is the well known Zel'dovich displacement, which is 1st order LPT.

The density field for a biased tracer can be defined by the displacement field $\boldsymbol{\Psi}(\mathbf{q})$ and a function of the smoothed initial density field in Lagrangian space, $F[\delta_L(\mathbf{q})]$, as

$$\delta_{\rm obj}(\mathbf{x}) = \int d^3q F[\delta_L(\mathbf{q})]\delta_D^{(3)}(\mathbf{x}-\mathbf{q}-\boldsymbol{\Psi})\ , \tag{2.21}$$

where $\mathbf{x}$ and $\mathbf{q}$ are the Eulerian and Lagrangian positions and $\delta_D^{(3)}$ is the 3D Dirac δ function. The power spectrum for such tracers can then be written as Matsubara (2008a,b)

$$\begin{aligned}P(k) = \int d^3q e^{-i\mathbf{kq}}\Bigg[\int_{-\infty}^{\infty}\frac{d\lambda_1}{2\pi}\frac{d\lambda_2}{2\pi}\widetilde{F}(\lambda_1)\widetilde{F}(\lambda_2)\times \\ \left\langle e^{i(\lambda_1\delta_L(\mathbf{q}_1)+\lambda_2\delta_L(\mathbf{q}_2))+i\mathbf{k}[\boldsymbol{\Psi}(\mathbf{q}_1)-\boldsymbol{\Psi}(\mathbf{q}_2)]}\right\rangle - 1\Bigg]\ ,\end{aligned} \tag{2.22}$$

where $\mathbf{q}=\mathbf{q}_1-\mathbf{q}_2$ and $\widetilde{F}$ is the Fourier transform of F. The distribution-averaged derivatives of $F(\lambda)$, $\langle F'\rangle$ and $\langle F''\rangle$, characterize the bias of the sample under consideration. Expressions for the case of peaks in the initial density field (i.e. peaks bias) can be found in Matsubara (2008b). For the halos considered in the text ($M \geq 10^{13}\,h^{-1}M_\odot$) we have $\langle F'\rangle = 0.55$ and $\langle F''\rangle = -0.37$, with large-scale bias 1.55.

To obtain the propagator we cross-correlate Eq. (2.21) with a field defined by $\exp(i\lambda\delta_L)$; δ_L^n is then simply obtained by taking the n-th derivative with respect to λ and setting λ to zero Padmanabhan & White (2009). This allows us to follow a procedure similar to that in Eq. (2.22).

The algebra now follows through as in Matsubara (2008a,b) using the cumulant expansion theorem, and collecting all zero-lag correlators to yield, e.g.

$$\begin{aligned}\langle\delta_L\delta_{\rm obj}\rangle &\propto \int d^3q\ e^{-i\mathbf{kq}} \\ &\times \quad \left[B_{01}^{10} + \frac{i}{2}B_{02}^{10} + \langle F'\rangle\left(B_{01}^{11} - i\xi\right)\right]\end{aligned} \tag{2.23}$$

where we have omitted the exponential damping terms for brevity and defined Matsubara (2008b)

$$B^{n_1 n_2}_{m_1 m_2} \equiv (-1)^{m_1} \times \langle [\delta_L(\mathbf{q}_1)]^{n_1} [\delta_L(\mathbf{q}_1)]^{n_2} [\mathbf{k}\mathbf{\Psi}(\mathbf{q}_1)]^{m_1} [\mathbf{k}\mathbf{\Psi}(\mathbf{q}_2)]^{m_2} \rangle_c \ , \tag{2.24}$$

with $\langle \cdots \rangle_c$ denoting the connected moments.

Straightforward algebra then yields

$$\begin{aligned} \langle \delta_L \delta_{\rm obj} \rangle &\propto P_L + \frac{5}{21} R_1 + \frac{3}{7} R_2 \\ &+ \langle F' \rangle \left(P_L + \frac{3}{7} \{ R_1 + R_2 \} \right) \end{aligned} \tag{2.25}$$

where Matsubara (2008b)

$$R_n(k) \equiv \frac{k^3}{(2\pi)^2} P_L \int_0^\infty dr \ P_L(kr) \widetilde{R}_n(r) \tag{2.26}$$

and

$$\widetilde{R}_1 = \int_{-1}^{1} d\mu \ \frac{r^2 (1-\mu^2)^2}{1 + r^2 - 2r\mu} \tag{2.27}$$

$$\widetilde{R}_2 = \int_{-1}^{1} d\mu \ \frac{(1-\mu^2) r\mu (1 - r\mu)}{1 + r^2 - 2r\mu} \tag{2.28}$$

while for the power spectrum, omitting the damping terms, Matsubara (2008b)

$$\begin{aligned} P_{\rm obj} &\propto (1 + \langle F' \rangle)^2 P_L + \frac{9}{98} Q_1 + \frac{3}{7} Q_2 + \frac{1}{2} Q_3 \\ &+ \langle F' \rangle \left[\frac{6}{7} Q_5 + 2 Q_7 \right] + \langle F'' \rangle \left[\frac{3}{7} Q_8 + Q_9 \right] \\ &+ \langle F' \rangle^2 [Q_9 + Q_{11}] + 2 \langle F' \rangle \langle F'' \rangle Q_{12} \\ &+ \frac{1}{2} \langle F'' \rangle^2 Q_{13} + \frac{6}{7} (1 + \langle F' \rangle)^2 [R_1 + R_2] \\ &- \frac{8}{21} (1 + \langle F' \rangle) R_1 \end{aligned} \tag{2.29}$$

with

$$\begin{aligned} Q_n(k) &\equiv \frac{k^3}{(2\pi)^2} \int_0^\infty dr \ P_L(kr) \int_{-1}^{+1} d\mu \\ &\quad P_L \left[k \sqrt{1 + r^2 - 2r\mu} \right] \widetilde{Q}_n(r, \mu) \end{aligned} \tag{2.30}$$

and expressions for the $\widetilde{Q}_n$ can be found in Matsubara (2008b).

Extending these results to reconstruction is now relatively straightforward, assuming that the smoothed density field can be well approximated by the linear field. The shifted field has $\mathbf{\Psi} = \mathbf{\Psi}^{(1)}\mathcal{S}$ and no higher order contributions, while the displaced field can be obtained from $\mathbf{\Psi}$ with the replacement $\mathbf{\Psi}^{(1)} \rightarrow \mathbf{\Psi}^{(1)}\left[1-\mathcal{S}\right]$ with $\mathbf{\Psi}^{(n\geq 2)}$ unchanged. This yields

$$\begin{aligned} \langle \delta_L \delta_s \rangle &\propto -P_L \mathcal{S} && (2.31) \\ \langle \delta_L \delta_d \rangle &\propto P_L \bar{\mathcal{S}} + \frac{5}{21} R_1 + \frac{3}{7} R_2^{(d)} \\ &+ \langle F' \rangle \left(P_L + \frac{3}{7} \left\{ R_1 + R_2 \right\} \right) && (2.32) \end{aligned}$$

where $\bar{\mathcal{S}} \equiv (1-\mathcal{S})$ and $R_2^{(d)}$ is evaluated using $P_L \bar{\mathcal{S}}$ inside the integral Eq. (2.26).

The power spectrum can be evaluated in a similar fashion, with the three contributions being

$$P^{ss} \propto P_L \mathcal{S}^2 + \frac{1}{2} Q_3^{(ssss)} \qquad (2.33)$$

and

$$\begin{aligned} P^{sd} + P^{ds} &\propto -2 P_L \mathcal{S} \bar{\mathcal{S}} + \frac{3}{7} Q_2^{(1s1s)} + Q_3^{(sdsd)} \\ &- \mathcal{S} \left[\frac{10}{21} R_1 + \frac{6}{7} R_2^{(d)} \right] \\ &+ \langle F' \rangle \left[-2 S P_L + 2 Q_7^{(1sds)} \right. \\ &- \left. \frac{6}{7} \mathcal{S} (R_1 + R_2) \right] \\ &+ \langle F'' \rangle Q_9^{(1s1s)} && (2.34) \end{aligned}$$

and

$$\begin{aligned}
P^{dd} &\propto P_L\bar{\mathcal{S}}^2 + \frac{9}{98}Q_1 + \frac{3}{7}Q_2^{(1d1d)} + \frac{1}{2}Q_3^{(dddd)} \\
&+ \bar{\mathcal{S}}\left[\frac{10}{21}R_1 + \frac{6}{7}R_2^{(d)}\right] \\
&+ \langle F'\rangle\left[2P_L\bar{\mathcal{S}} + \frac{6}{7}Q_5^{(1d11)} + 2Q_7^{(1ddd)} + \right. \\
&\left. \frac{10}{21}R_1 + \frac{6}{7}R_2^{(d)} + \frac{6}{7}\bar{\mathcal{S}}(R_1+R_2)\right] \\
&+ \langle F''\rangle\left[\frac{3}{7}Q_8 + Q_9^{(1d1d)}\right] \\
&+ \langle F'\rangle^2\left[P_L + \frac{6}{7}(R_1+R_2) + Q_9^{(1d1d)} + Q_{11}^{(11dd)}\right] \\
&+ 2\langle F'\rangle\langle F''\rangle Q_{12}^{(111d)} + \frac{1}{2}\langle F''\rangle^2 Q_{13}
\end{aligned} \tag{2.35}$$

where we have again omitted the damping terms and the superscripts indicate which P_L are to be replaced with $P_L\mathcal{S}$, $P_L\bar{\mathcal{S}}$ etc. For the Q_n there are 4 possible smoothing terms, and we have indicated no smoothing with a 1, $\mathcal{S}$ with an s and $\bar{\mathcal{S}}$ with a d. The first two terms have argument kr and the second have argument $k\sqrt{1+r^2-2r\mu}$ in Eq. (2.30). Thus for example

$$\begin{aligned}
Q_7^{(1sds)}(k) &= \frac{k^3}{(2\pi)^2}\int_0^\infty dr\ P_L(kr)\mathcal{S}(kr) \\
&\times \int_{-1}^{+1} d\mu\ P_L(ky)\mathcal{S}(ky)\bar{\mathcal{S}}(ky) \\
&\times \widetilde{Q}_7(r,\mu)
\end{aligned} \tag{2.36}$$

with $y = \sqrt{1+r^2-2r\mu}$.

Chapter 3

The geometry of the filamentary environment of galaxy clusters

We construct a filament catalogue using an extension of the halo based filament finder of Zhang et al. (2009), in a 250 Mpc h^{-1} side N-body simulation, and study the properties of filaments ending upon or in the proximity of galaxy clusters (within 10 Mpc h^{-1}). In this region, the majority of filamentary mass, halo mass, and galaxy richness centered upon the cluster tends to lie in sheets, which are not always coincident. Fixing a sheet width of 3 Mpc h^{-1} for definiteness, we find the sheet orientations and (connected) filamentary mass, halo mass and richness fractions relative to the surrounding sphere. Filaments usually have one or more endpoints outside the sheet determined by filament or halo mass or richness, with at least one having a large probability to be aligned with the perpendicular of the plane. Scatter in mock cluster mass measurements, for several observables, is often correlated with the observational direction relative to these local sheets, most often for richness and weak lensing, somewhat less for Compton decrement, and least often for velocity dispersions. The long axis of the cluster also tends to lie in the sheets and its orientation relative to line of sight also correlates with mass scatter. [1]

3.1 The geometry of the filamentary environment of galaxy clusters: Introduction

Large scale structure in the Universe forms a cosmic web (Zeldovich et al. 1982; Shandarin & Zeldovich 1983; Einasto et al. 1984; Bond et al. 1996), evident in the Universe's dark matter, halo, galaxy, and gas distributions. The richness of the cosmic web is evident when one has sufficient statistics and resolution (numerically) or sensitivity (observationally) to see beyond the densest structures, correspondingly there has been a wealth of study of its prop-

[1] This chapter has been previously published as Noh & Cohn (2011), and is reproduced with the permission of all coauthors and the copyright holder.

erties. Examples include characterization of average properties (e.g. see Schmalzing (1998) for one early review, Shandarin (2004); van de Weygaert et al. (2010); Shandarin (2011) for some more recent papers and references within), identifying the web in observations and simulations (e.g., Bharadwaj et al. (2000); Pimbblet et al. (2004); Porter & Raychaudhury (2007); Feix et al. (2008); Porter et al. (2008); Sousbie et al. (2008b); Bond et al. (2010a); Way et al. (2011); Bond et al. (2010b); Choi et al. (2010); Mead et al. (2010); Murphy et al. (2011); Sousbie et al. (2011), tracing its relation to initial conditions (e.g., Shandarin et al. (2012)) and comparing filamentary environments and properties of galaxies within them (spin, shapes, alignments and more: Lee (2004); Lee et al. (2008); Altay et al. (2006); Aragón-Calvo et al. (2007b); Dolag et al. (2006); Pandey & Bharadwaj (2006); Faltenbacher et al. (2007); Ragone-Figueroa & Plionis (2007); Hahn et al. (2007b,a); Paz et al. (2008); Betancort-Rijo & Trujillo (2009); Gay et al. (2010); Schäfer (2009); Zhang et al. (2009); Hahn et al. (2010); Jones et al. (2010); Wang et al. (2011)). Cluster alignments and formation, presumably or explicitly along filaments, have also been studied, e.g. van de Weygaert & Bertschinger (1996); Splinter et al. (1997); Colberg et al. (1999); Chambers et al. (2000); Onuora & Thomas (2000); Faltenbacher et al. (2002); van de Weygaert (2002); Hopkins et al. (2005); Bailin & Steinmetz (2005); Faltenbacher et al. (2005); Kasun & Evrard (2005); Lee & Evrard (2007); Lee et al. (2008); Pereira et al. (2008); Costa-Duarte et al. (2011), and several observed systems with filaments have been analyzed in detail, some examples are found in Porter & Raychaudhury (2005); Gal et al. (2008); Kartaltepe et al. (2008); Tanaka et al. (2009). Numerous methods for identifying filaments, suitable for different applications, have been proposed (for example Barrow et al. (1985); Mecke et al. (1994); Sahni et al. (1998); Schmalzing et al. (1999); Colombi et al. (2000); Sheth et al. (2003); Pimbblet (2005a,b); Stoica et al. (2005); Novikov et al. (2006b); Aragón-Calvo et al. (2007a); Colberg (2007); van de Weygaert & Schaap (2007); Sousbie et al. (2008a); Stoica et al. (2010); Forero-Romero et al. (2009); González & Padilla (2010); Pogosyan et al. (2009); Sousbie et al. (2009); Stoica et al. (2010); Wu et al. (2009); Genovese et al. (2010); Murphy et al. (2011); Shandarin (2011); Sousbie (2011); Way et al. (2011)), see Zhang et al. (2009); Aragón-Calvo et al. (2010) for some comparisons of these. Analytic studies of filaments include estimates of their multiplicity (Shen et al. 2006), anisotropy (e.g.Lee & Springel (2010)), the merger rates of halos into them (Song & Lee 2011) and properties in non-Gaussian theories (de Simone et al. 2011).

Galaxy clusters (dark matter halos with mass $M \geq 10^{14}h^{-1}M_{\odot}$) are of great interest for many reasons, in part because of their sensitivity to cosmological parameters, but also as hosts of the most massive galaxies in the Universe, as environments for galaxy evolution more generally, and as the largest virialized objects in the Universe with correspondingly special astrophysical processes and histories (for a review see e.g. Voit (2005)). Galaxy clusters tend to lie at nodes of the cosmic web, with matter streaming into them from filaments (e.g. van Haarlem & van de Weygaert (1993); Diaferio & Geller (1997); Colberg et al. (1999)). Although the Universe is isotropic and homogeneous on large scales, around any individual cluster there will be directionally dependent density fluctuations due to the condensation of filamentary and sheetlike matter around it. Our interest here is in characterizing this nearby

(within 10 Mpc h^{-1}) filamentary environment of galaxy clusters. This environment feeds galaxy clusters and is also unavoidably included for many observations of the cluster at its center. This correlated environment is one source of the observationally well known "projection effects," which have plagued optical cluster finding starting with Abell (1958) and later (e.g. Dalton et al. (1992); Lumsden et al. (1992); van Haarlem et al. (1997); White et al. (1999)), cluster weak lensing, e.g., Reblinsky & Bartelmann (1999); Metzler et al. (2001); Hoekstra (2001); de Putter & White (2005); Meneghetti et al. (2010); Becker & Kravtsov (2011), cluster Sunyaev-Zel'dovich (Sunyaev & Zeldovich 1972, 1980) (SZ) flux measurements, e.g., White et al. (2002); Holder et al. (2007); Hallman et al. (2007); Shaw et al. (2008) and cluster velocity dispersions, e.g., Cen (1997); Tormen (1997); Kasun & Evrard (2005); Biviano et al. (2006). The environments of clusters have been studied within several contexts and using several methods, e.g. galaxy and dark matter density around clusters (Wang et al. 2009; Poggianti et al. 2010), filamentary growth (e.g. van de Weygaert (2006)) around clusters, filamentary counts (Pimbblet et al. 2004; Colberg et al. 2005; Aragón-Calvo et al. 2010; Aragon-Calvo et al. 2010), in particular the geometry and properties of superclusters, e.g., Shandarin et al. (2004); Basilakos et al. (2006); Wray et al. (2006); Costa-Duarte et al. (2011), and the cluster alignment studies such as mentioned above.

Here we describe our findings on local cluster environments obtained by implementing the halo-based filament finder of Zhang et al. (2009) in a high resolution N-body simulation. After refining the finder slightly for our purposes, we obtain a filament catalogue, and consider those filaments connected to or in the vicinity of galaxy clusters. Our work is most closely related to that of Colberg et al. (2005); Aragón-Calvo et al. (2010). They used simulations to measure counts of filaments (found via different algorithms) ending upon clusters and average filamentary profiles and curvature (observationally counts were found for the 2dFGRS dataset in Pimbblet et al. (2004)). We go beyond these to measure the statistics of the local geometry of filaments around their cluster endpoints. Related studies of filament geometry, particularly for superclusters, are found in e.g., Aragón-Calvo et al. (2010); Aragon-Calvo et al. (2010), the former also discuss the tendency of filaments around voids and clusters to lie in sheets. We find that most of the filamentary (and halo) material in a 10 Mpc h^{-1} sphere around clusters lies in a plane, presumably the one from which the filaments collapsed, and investigate different ways of defining such a plane's orientation. Many measures of cluster masses include the cluster environment and as a result scatter the mass from its true value. In mock observations on simulations, we find that line of sight dependent scatter in measured cluster masses, for several methods, is often correlated with the angle between the line of sight and these locally defined planes.

In §2 we describe the simulations, mock observations, and filament finder. In §3 we describe the statistical properties of the filaments and matter distribution around clusters, in §4 we consider the geometry of the filament, mass and richness distributions within 10 Mpc h^{-1} of each cluster, focussing particularly on planes maximizing these quantities, in §5 we compare scatter in cluster masses to orientation of observations with these planes, and in §6 we conclude.

3.2 The geometry of the filamentary environment of galaxy clusters: Simulations and Methods

3.2.1 Simulation

We use a dark matter only simulation, in a periodic box of side 250 Mpc h^{-1} with 2048^3 particles evolved using the TREEPM (White 2002) code, and provided to us by Martin White. It is the same simulation as used in White et al. (2010) (hereafter WCS), which can be consulted for details beyond those found below. The background cosmological parameters are $h = 0.7$, $n = 0.95$, $\Omega_m = 0.274$, and $\sigma_8 = 0.8$, in accord with a large number of cosmological observations. The simulation has outputs at 45 times equally spaced in $\ln(a)$ from $z = 10$ to 0. We focussed on $z = 0.1$, in part to allow comparison with observational quantities in §5. Halos are found using a Friends of Friends (FoF) halo finder (Davis et al. 1985), with linking length $b = 0.168$ times the mean interparticle spacing. Masses quoted below are FoF masses.

Resolved subhalos in this high resolution simulation are of importance for the observational comparisons in §5, and for measurements of galaxy properties around and in the clusters. Subhalos are found via FoF6d (Diemand et al. 2006), with the specific implementation as described in the appendix of WCS. The subhalos correspond to galaxies with luminosities $\geq 0.2L^*$ at $z = 0.1$[2], and match observations as described in WCS. The halo and subhalo catalogues and dark matter particles can be combined to produce mock observations for six cluster mass measures. These are (see WCS for specifics and tests of the catalogue): two richnesses (one using the Koester et al. (2007) MaxBCG algorithm based upon colours[3], and one based upon spectroscopy, with cluster membership assigned via the criteria of Yang et al. (2008)), SZ flux or Compton decrement (flux within an annulus of radius r_{180b}, the radius within which the average mass is greater than or equal to 180 times background density), weak lensing (using an SIS or NFW model to assume a cluster lens profile and then fitting for a velocity dispersion and then mass), and two velocity dispersions (one based on a simple $3-\sigma$ clipping, the other on a more complex method using phase space information to reject outliers and calculating mass using a measured harmonic radius as well, based on methods of den Hartog & Katgert (1996); Biviano et al. (2006); Wojtak et al. (2007)); more detail is in WCS. We will use the mass measurements by WCS via these methods, taking cylinders of radius r_{180b} when a radius choice is required. Just as in that work, lines of sights for clusters are removed when a more massive cluster has its center within this radius along the observational line of sight.

[2]Approximately -18.5 in r band, see WCS for more discussion.

[3]Colour assignments are estimated using the prescription of Skibba & Sheth (2009) with evolution of Conroy et al. (2009, 2010); Conroy & Gunn (2010). Galaxies are taken to be "red" if they have $g-r$ within 0.05 of the peak of the red galaxy $g-r$ distribution specified by Skibba & Sheth (2009), for their observed M_r, again see WCS for more detail.

3.2.2 Filament finder

We find filaments using an extension of the method described in Zhang et al. (2009). They identify filaments as bridges in dark matter halos above a threshold halo mass overdensity, of length up to 10 Mpc h^{-1}. It is analogous to the spherical overdensity finder for clusters, where the cluster radius is taken to be that where the average density around the central point drops below some threshold; here the filament radius is where the average density along the cylinder axis drops below some threshold. Just as there are many different halo finders, there is no unique filament finder or definition. This finder is but one of many different ones present in the literature, which are not only based upon such bridge-like definitions, but also include finders constructed around filtering procedures, potential or density gradients, dynamical information, and more (see Zhang et al. (2009) for some comparisons between their finder and others). Even for a given filament finder, catalogues often must be specified by the finder parameters as well (e.g. smoothing length for density or potential based finders, unbinding criteria for dynamically based finders, etc.). We use the parameters as given in Zhang et al. (2009).

The algorithm of Zhang et al. (2009) is as follows: halos are ordered most to least massive. All halos with mass $\geq 3 \times 10^{10} h^{-1} M_{\odot}$ are included[4], mass in the following only refers to that in halos with this mass or above. Starting with the most massive halo ("node"), all halos within 10 Mpc h^{-1} but at least 3 Mpc h^{-1} away in radius (or r_{200c}, if greater, which did not occur in our sample) are considered as potential endpoints. For each potential endpoint, the cylinder radius is varied, up to 3 Mpc h^{-1}, to get the highest overdensity of halo matter in the cylinder between the node and potential endpoint.[5] This maximum density is then compared to a minimum overdensity (5 times background matter density in halos), and if over this minimum, this endpoint and its radius are kept. If no potential endpoints have a halo mass density for their filament greater than the minimum overdensity then the algorithm moves to the next node. Once all such maximal filaments are found for a given node, the filament with the largest density is kept. The filament is then truncated: its new endpoint is the most massive halo within it which has at least 3 other halos between in and the central node, and which is at least 3 Mpc h^{-1} away from the central node. All filament members are then removed from the list of potential future filament members or endpoints around any node. The endpoints are not removed from the list of possible endpoints for other nodes, but are removed from the list of possible endpoints associated with this node. This procedure is repeated until no more new filaments are found around the node.

As this procedure frequently produces many more filaments than were evident by eye around clusters (sometimes over thirty around a single cluster), we incorporate a growing and merging procedure as well. After finding the filaments of maximum density around a given node, we grow out the filament radii until the average mass density in halos within

[4]This is the minimum mass used by Zhang et al. (2009) converted (see White (2001)) to our FoF definition.

[5]This radius scale is slightly smaller than that found for galaxy filaments in the 2dGFRS survey (Porter & Raychaudhury 2007; Porter et al. 2008). We thank the referee for pointing this out to us.

the cylinder stretching to the filament endpoint drops to less than the minimum overdensity, or the maximum 3 Mpc h^{-1} radius is reached. Halos lying in two or more such extended filaments are assigned to the one whose axis is closest. Filament endpoints with length ℓ and a perpendicular distance $d_\perp$ to another (longer) filament's axis such that $d_\perp/\ell < 3/10$ (the maximum width/maximum length in the algorithm) are merged into the longer filament, unless the shorter filament's endpoint has other filaments extending out of it. (This allows filament radii >3 Mpc h^{-1}.) These new filaments are then given a central axis determined by the center of mass of the filament; filaments whose endpoints do not have additional filaments extending out of them and whose endpoints are within 25 degrees of each other are merged. This is done in order of closest to most distant pairs; if > 2 filaments are within this range, the two closest are merged, then centers of mass are recalculated to see if the remaining filaments are within the minimum distance, and so on. As an example, the two most massive filaments extending from a cluster of mass $2.7 \times 10^{14} h^{-1} M_\odot$ are shown in Fig. 3.1.

The resulting filaments are regions connecting halos with halo mass overdensity at least 5 times the background halo mass density, and which are less than 10 Mpc h^{-1} long. The full catalogue at $z = 0.1$ has $\sim 30,000$ filaments and $\sim 44,000$ endpoints, with 45% of the halo mass fraction in filaments and 36% of the halos (in number fraction) in filaments. 60% of the $\sim 1.2 \times 10^6$ halos above the minimum mass cut are not either endpoints or in filaments, with the most massive of these having $M = 2.6 \times 10^{12} h^{-1} M_\odot$. [6]

Several of the other finders produce filaments which can extend well beyond our 10 Mpc h^{-1} cutoff (e.g. Colberg et al. (2005) found filaments out to 50 Mpc h^{-1}, even longer ones have been found by e.g, González & Padilla (2010)), some have restrictions on filament nodes (e.g. Colberg et al. (2005) filaments end only on clusters). Our catalogue has straight filament segments $\leq$ 10 Mpc h^{-1} in length, built out of dark matter halos above some minimum overdensity which emanate from clusters and other endpoints. Longer filaments could presumably be constructed as chains of our shorter ones, augmented by a condition on how much a filament can bend before it is considered instead to be two separate filaments meeting at a node. The length restriction of our finder also affects breakdowns into mass fraction in filaments, nodes, and so on, as some of our nodes will instead be filament members if the filaments are extended this way.

The work most similar to ours in focus, studying clusters as filament endpoints, is in Colberg et al. (2005), some related results are also found and compared in Aragón-Calvo et al. (2010) (see also Sousbie et al. (2011), who found a cluster as an intersection of filaments in observational data). Colberg et al. (2005) found filaments by looking for matter overdensities by eye between cluster endpoints and measured a wide range of filament statistics, including the number of filaments per cluster as a function of mass, stacked filament profiles, length distributions, and the fractions of cluster pairs connected by filaments. Aragón-Calvo et al.

[6] Analytic estimates of filamentary mass fractions mentioned above (which use other filament definitions) are not directly comparable because the latter are based upon total mass; mass in halos above our minimum is only 40% of the mass in the box at $z = 0.1$.

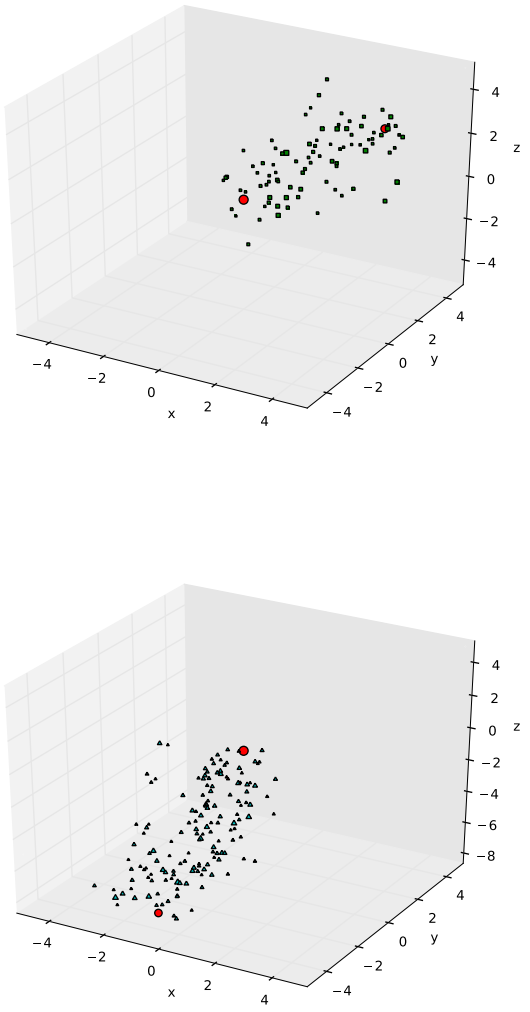

Figure 3.1: The two largest filaments around a cluster of mass $2.7 \times 10^{14} h^{-1} M_{\odot}$ cluster, after the merging procedure. The central cluster and the two filament endpoints are shown as large filled circles, other points are other halos in the filaments. Shown at left are the halos in the most massive filament ($4.3 \times 10^{13} h^{-1} M_{\odot}$), with a halo of mass $2.4 \times 10^{13} h^{-1} M_{\odot}$ as its endpoint. At right are the halos in the second most massive filament ($4.1 \times 10^{13} h^{-1} M_{\odot}$) and the $1.1 \times 10^{13} h^{-1} M_{\odot}$ endpoint. The units are Mpc h^{-1}. The full distribution of filamentary mass around this cluster is shown in Fig. 3.4.

(2010) found filaments using a Multiscale Morphology Filter (see their paper for details) and considered similar quantities to Colberg et al. (2005), and in addition introduced a classification for filaments.

3.3 Statistics of filaments around clusters

Our finder is well suited to characterize the local environment of clusters, our target of study here. Of the 242 clusters ($M \geq 10^{14}h^{-1}M_{\odot}$) in our box, 226 are also nodes, with ~ 1700 filaments. We restrict to these clusters below. Their characteristic radii r_{200c} (radius within which the average enclosed density is 200 times the critical density) range between 0.6 Mpc h^{-1} and 1.9 Mpc h^{-1}, i.e. these are not only the extremely rich and massive clusters. The 7% (16) of the clusters which are not nodes are within a filament extending from a more massive cluster, 15 of the clusters have a cluster within a filament. There are also 41 pairs of clusters within 10 Mpc h^{-1} of each other. We use the term "connected" filamentary mass to refer to halo mass within a filament connected directly to a cluster, up to and including its other endpoint. [7] In addition to connected filaments around a cluster, within the 10 Mpc h^{-1} sphere we will also consider all filaments and their endpoints, all halos above our minimum mass of $3 \times 10^{10}h^{-1}M_{\odot}$, and all galaxies.

In the 10 Mpc h^{-1} spheres surrounding clusters, connected filaments constitute $\sim 70\%$ of the halo mass on average, but with a very broad distribution of values for individual clusters. A line passing through the 10 Mpc h^{-1} shell centered on a cluster will hit one of the original connected filament cores (from the first step of our algorithm) about 10% of the time on average, and one of the grown and merged filaments closer to $\sim 30\%$ of the time, with a wide spread as well. All (not only connected) filaments in this sphere contain closer to $\sim 90\%$ of the halo mass, with much less cluster to cluster scatter. (The unconnected filaments for this cluster go between two other nodes. These other nodes themselves may or may not lie within the 10 Mpc h^{-1} sphere.) In 10 Mpc h^{-1} spheres around 10,000 random points, in comparison, the filaments have a halo mass fraction ranging from 60% to 95%.

The distribution of number of connected filaments around clusters, with our finder, is shown at the top of Fig. 3.2, clusters tend to have 7-9 filaments. We find more massive halos have more filaments ending upon them, shown in Fig. 3.2, bottom, just as found by Colberg et al. (2005); Aragón-Calvo et al. (2010) with their different finders. In addition, connected filaments around clusters tend to be shorter than their counterparts for the much less massive nodes.

[7] The finder, even with modifications, still produced some configurations which we modified with post-processing. For example, sometimes a filament would be found with a large "gap" in the center, where the gap is due to a previously found filament between two other clusters which crosses the region. Even with this gap, the new filament is above our overdensity threshold. As the previous and new filaments seem joined and perhaps one object, we added all the mass (within 10 Mpc h^{-1}) of any previously found filament which came within 3Mpc h^{-1} to the connected filamentary mass of the cluster, this happened for < 10 of our $\sim$7000 filaments.

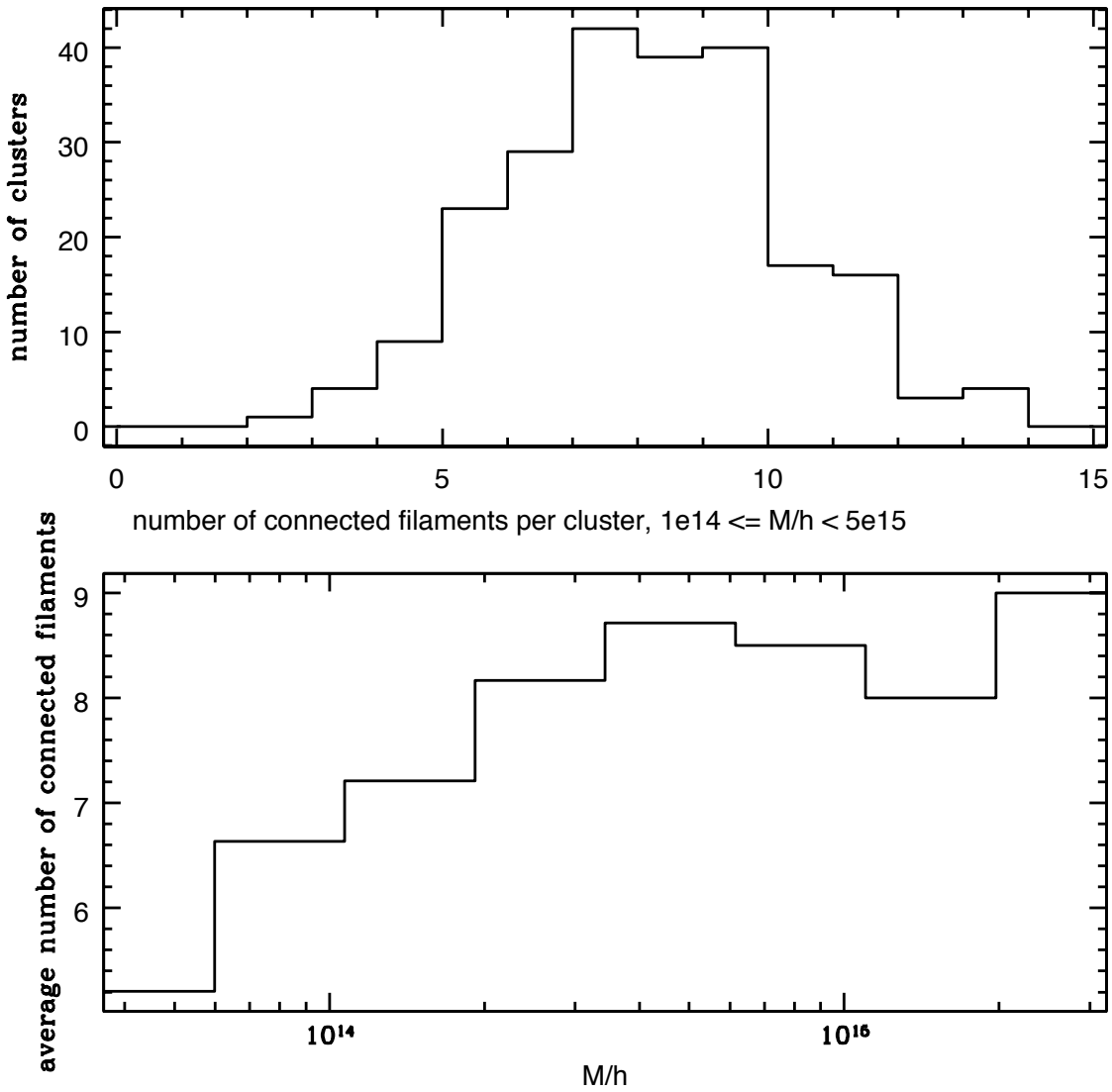

Figure 3.2: Top: distribution of number of filaments per cluster (halos with $M \geq 10^{14}h^{-1}M_{\odot}$). Bottom: number of filaments as a function of mass for all halos which are filament endpoints.

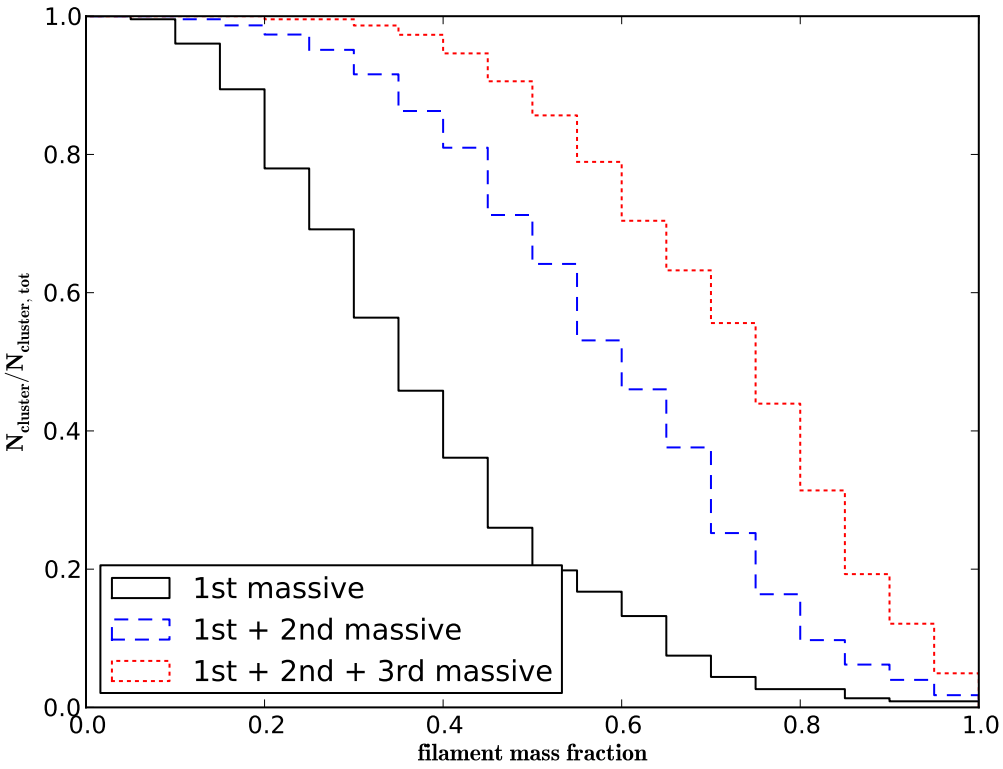

Figure 3.3: Cumulative fraction of filamentary mass in 1 (solid line), 2 (dashed line) and 3 (dotted line) most massive cluster filaments, as fraction of the number of clusters. For example, about half of the clusters have at least 60% of their connected filament mass in their two largest filaments and at least $\sim 75\%$ of their mass in their three largest filaments.

The large number of filaments found by the algorithm can be compared to a simplified picture where nodes are fed by a small number of filaments (e.g. 3 or fewer, Kereš et al. (2005, 2009); Dekel et al. (2009)). The mass fraction in the largest 2 or 3 filaments is substantial, leading to a partial reconciliation of these pictures, as seen in Fig. 3.3, that is about half of the clusters have at least $\sim 75\%$ of their mass in their three largest filaments.

More massive halos have more filaments around them, more matter in filaments, and more matter around them generally, and although the number of filaments for clusters can be quite large, a significant fraction of the filamentary mass is found within the three largest filaments.

3.4 Planar Geometry around clusters

Filaments provide an anisotropic environment for galaxy clusters. Some approximate trends in the filamentary distribution are accessible via the inertia tensor of its mass, even though filaments are not expected to fill out an ellipsoid. For connected filaments attached to our clusters, the middle eigenvalue of the inertia tensor tends to be smaller than that for the clusters, so that the filament distribution is "flatter" than the cluster it surrounds.[8] For reference, the cluster moment of inertia tensors tend to have two relatively large eigenvalues and one smaller one (corresponding to axis ratios $a > b \sim c$, the classic prolate cluster shape; there are many studies of cluster ellipticities, see e.g. Jing & Suto (2002)). The long axis of the cluster has a tendency to lie within the "flat" directions of the filamentary distribution, and the eigenvector of the cluster's inertia tensor that is perpendicular to the long and middle axes of the cluster (i.e. corresponding to the largest eigenvalue) tends to align with the corresponding direction of the filamentary inertia tensor. (See also van de Weygaert (2006); Hahn et al. (2007a); Aragón-Calvo et al. (2007b); Paz et al. (2008); Aragón-Calvo et al. (2010); as our nodes will sometimes be members of filaments in other finders, some of these alignments are relevant filament member alignment discussed therein.)

Visual inspection of many of our clusters suggests that the majority of their filamentary mass lies within sheetlike regions, presumably those from which they condensed (see for example some cases illustrated in Aragon-Calvo et al. (2010), and discussion of different filament types in Aragón-Calvo et al. (2010) and their "grid" and "star" configurations).

To quantify this planarity, we consider four definitions of planes, regions extending ± 1.5 Mpc h^{-1} above and below the central cluster and out to the edge of the local 10 Mpc h^{-1} sphere. We choose their orientations (normals) so the planes contain the maximum of either 1) connected filament mass, with extra constraints described below, 2) all filamentary mass including endpoints, 3) total halo mass, or 4) number of galaxies, within the 10 Mpc h^{-1} sphere. The connected filament mass plane has its normal chosen to be perpendicular to the axes constructed out of a pair of filament endpoints; this definition has stronger correlations with observables (discussed later) than using pairs of connected filaments without their endpoints, or using the plane maximizing connected filament mass with no other constraints. The mass in the plane (or richness, when using galaxies) does not include that of the central cluster, as our interest is in the cluster's environment. In Fig. 3.4 the objects used for these four choices of plane are shown for a cluster of mass $2.7 \times 10^{14} M_\odot/h$. It has about 84% of its mass in the connected filament plane.

These four planes tend to have similar orientations, with the all filament and halo mass planes are most often aligned (over 96% clusters have these two normals within 30 degrees).

[8] The connected filament distribution becomes more and more cylindrical with decreasing (well below $10^{14} h^{-1} M_\odot$) central halo mass, with the two largest eigenvalues tending to become equal, and the third becoming smaller and smaller. One reason is that lower mass halos are expected to be within filaments, rather than to serve as endpoints; the algorithm used here will tend to break these longer filaments up into more segments as mentioned earlier.

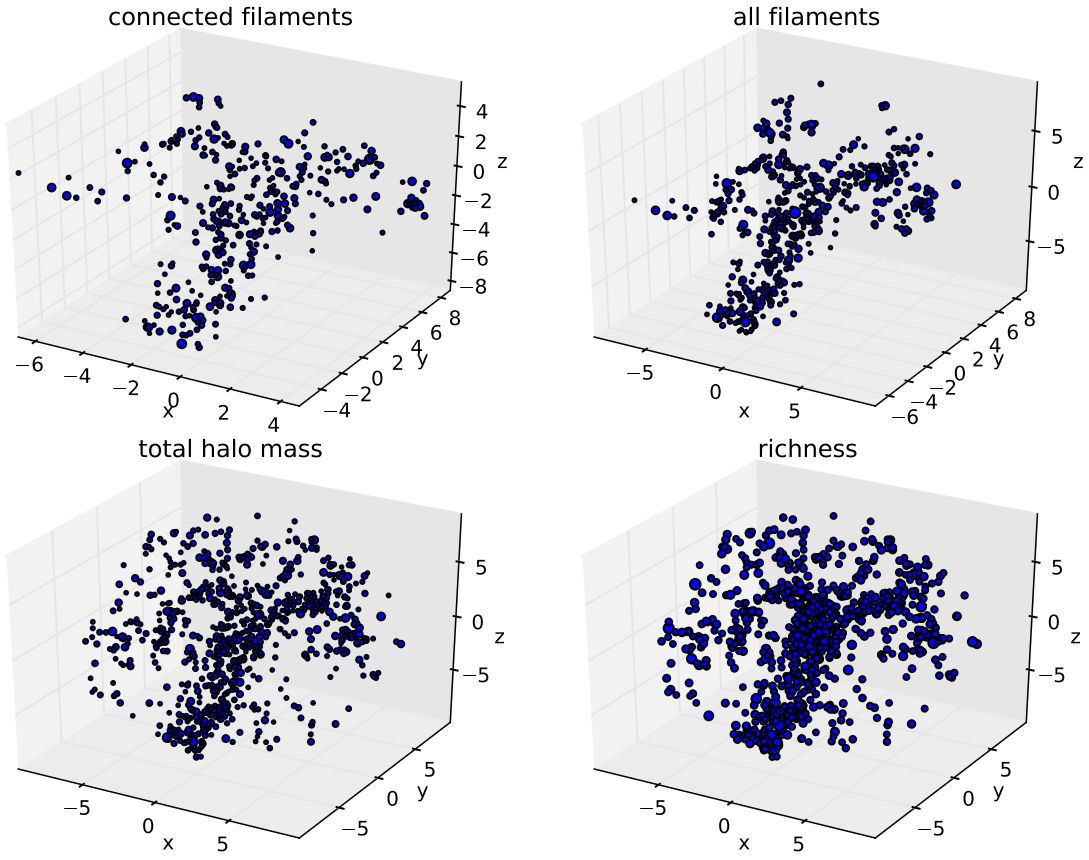

Figure 3.4: Four types of objects used in constructing planes in a 10 Mpc h^{-1} radius sphere centered on a $2.7 \times 10^{14} h^{-1} M_{\odot}$ cluster. Left to right, top to bottom are halos in connected filaments, halos in all filaments, all halos above $3 \times 10^{10} h^{-1} M_{\odot}$ mass cut, and galaxies above $0.2L^*$ cut (galaxies in cluster are not shown). Point size is proportional to halo mass or, for richness, halo infall mass (which determines luminosity, see WCS). About 84% of the cluster's connected filament mass is in the connected filament plane.

This is not surprising given the dominance of filamentary mass in the 10 Mpc h^{-1} sphere around the cluster noted earlier. For a given cluster, the largest misalignment between any pairs of planes tends to be between its connected filament plane and one of the other planes, which for 15% of the clusters differs by another plane by more than 60 degrees. For most clusters it thus seems that the connected filaments are not as closely aligned with the other planes, which extend further out into the sphere. Plane pairs besides the closely aligned all filament and halo mass plane have on average $5-10\%$ of the clusters mismatching by >60 degrees.

The mass or richness fractions in these planes is significantly higher than the fraction ($\sim$1/5) of volume which the plane occupies in the sphere. The distribution of connected and total filament mass fractions, in the corresponding planes, for our clusters is shown at top in Fig. 3.5, at bottom is the distribution for the total halo mass plane. Also shown at bottom is the mass fraction for halo mass planes constructed around 10,000 random points (rescaled to have the same area under the curve), which is smaller on average than around the clusters. The richness fraction, not shown, peaks slightly more sharply than the halo mass fraction, but at a lower fraction ($\sim 60\%$). For all plane definitions, 80% of the clusters have more than 60% of their mass (or 55% of their richness) in these planes; about a quarter of the clusters fell below this fraction for at least one plane definition. Our choice of plane height, $\pm$ 1.5 Mpc h^{-1} to give 3 Mpc h^{-1} in total, was motivated by the characteristic scale of cluster radii. We explored mass plane heights from 1-3 Mpc h^{-1} (total plane widths 2-6 Mpc h^{-1}), and found that the total halo mass fraction scaled as $M_{\rm plane}/M_{\rm sphere} \sim {\rm height}^{1/4}$. It would be interesting to understand this scaling in terms of intrinsic filament profiles.

The clusters with large plane misalignments (by >60 degrees) have low mass or richness fractions, or larger mass within 3 Mpc h^{-1} of the normal of the connected filament plane (but outside of it) almost twice as often as in the full sample (i.e. in $\sim$2/3 of the clusters with mismatched planes). The misaligned plane clusters have only slightly more often a recent[9] merger or a larger intrinsic cluster flatness (as measured by its inertia tensor), they were equally likely to have other clusters within 10 Mpc h^{-1} as in the full sample.

The connected filament plane's normal, similar to its counterpart for the connected filament's inertia tensor, tends to be aligned with its counterpart for the cluster's mass inertia tensor, and the cluster's long axis is likely to lie in the filament plane. The cluster galaxy positions, have an inertia tensor (setting mass to one) which appears uncorrelated with this plane. However, restricting to more luminous ($> 0.4L_*$, see WCS for detail) galaxies gives an inertia tensor whose "most flat" (perpendicular to eigenvector for largest eigenvalue) direction prefers alignment with the normal to the connected filamentary plane, and whose "long" axis tends to be within the filament plane. The cluster galaxy velocity dispersions can also be given an "inertia tensor" after subtracting off the average velocity. The alignments of this tensor are more correlated (e.g. Kasun & Evrard (2005); White et al. (2010)) with the inertia tensor of the cluster itself than with that of the plane.

[9]Specifically, a satellite which has fallen into the cluster within the last time step, $\sim 600 Myrs$, which had at the earlier time at least 1/10 of the cluster's final mass at $z = 0.1$.

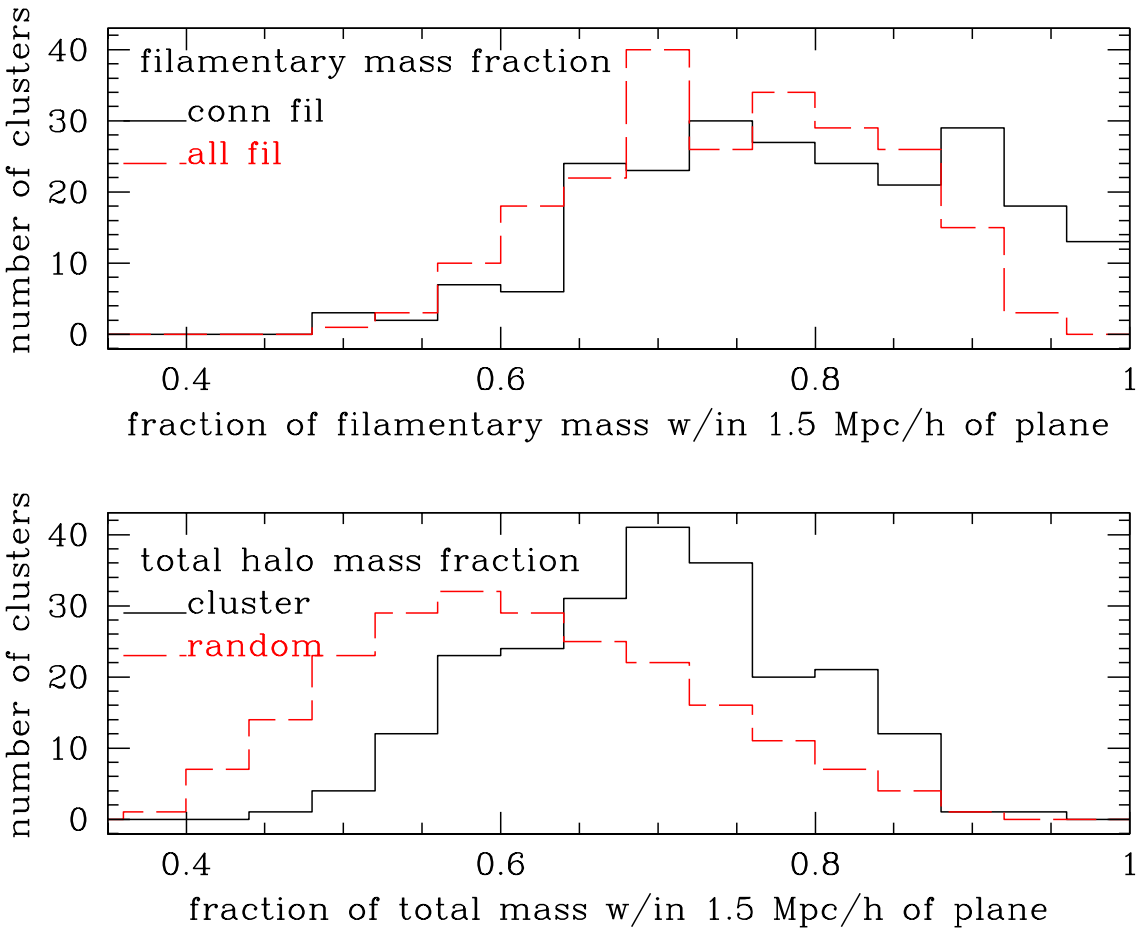

Figure 3.5: Top: Fraction of connected filament mass in connected filament plane (solid) and fraction of all filamentary mass within all filament plane (dashed), both in the fiducial 10 Mpc h^{-1} sphere around clusters. The normals to these planes are within 30 degrees for ∼80% of the clusters. Bottom: The fraction of total halo mass (above our $3 \times 10^{10} M_{\odot}/h$ cutoff) in the mass plane around clusters (solid), and its counterpart around 10,000 random points (dashed, rescaled to have the same number volume as cluster histograms). A large fraction of the filamentary mass and total halo mass in 10 Mpc h^{-1} spheres around clusters resides within this planar region containing ∼20% of the volume.

Not all filaments lie in these planes. Filamentary mass can extend outside of the plane, as mentioned earlier, as can filament endpoints. The fraction of filament endpoints lying outside the connected filament plane is shown in Fig. 3.6, note that this does not preclude a significant amount of the filament's mass lying within the plane.

There is also an increased likelihood for at least one endpoint to lie perpendicular to the connected plane, as shown in Fig. 3.6 bottom.The distributions in Fig. 3.6 are similar for the other plane choices. About 1/10 of the clusters have more than ∼3% of their connected filamentary mass within a 3 Mpc h^{-1} radius of the normal to their plane but above or below the plane itself, which we refer to as perpendicular filaments below. In addition 10 clusters have over 15% of their mass in a region within 6 Mpc h^{-1} radius of the normal, but outside the connected plane.

As noted earlier (Fig. 3.3), the two most massive connected filaments often do possess a large fraction of the connected filament mass. The plane defined by these two filaments coincides with the connected filamentary mass plane almost half of the time.[10]For 1/3 of the clusters, however, less than half of the connected filament planar mass comes from these two most massive segments. So although the two most massive segments have a preponderance of filamentary mass (Fig. 3.3), their large mass is not wholly responsible for the dominance of planar structure.

The persistence of the locally defined planes to larger radii can be studied by fixing the plane height and orientation, and extending the plane out into a region of 20 Mpc h^{-1} in radius, and calculating the fractional mass in this larger plane within the larger sphere. The plane volume fraction of the sphere volume drops by about one half compared to its value in the 10 Mpc h^{-1} sphere, but the (all) filamentary mass, halo mass and richness fractions in their respective planes drop by even more, by a factor of $\sim 40\%$. There are filamentary, mass or richness planes in this larger sphere of the same ± 1.5 Mpc h^{-1} width which have more of the filamentary, mass or richness in them (and usually more than 1/2 the mass fraction of those defined within 10 Mpc h^{-1}). These 20 Mpc h^{-1} filament and mass planes differ from their counterparts at 10 Mpc h^{-1} by over 30 (60) degrees one half (one quarter) of the time, with slightly smaller fractions for the corresponding richness plane.

We did not find a more useful measure of isotropy in the plane (i.e. in the angular direction), although the moment of inertia tensor can indicate how much the planar geometry tends to cylindrical (related questions have been explored when classifying filaments, e.g.(Aragón-Calvo et al. 2010) note a "star" geometry for sets of filaments). One possible consequence of isotropy, or its lack, in the plane will be discussed in the next section on mass measurements.

In summary, as has been known, the mass around clusters tends to lie in filaments, which themselves tend to lie within sheets. We have taken a set sheet width centered on the cluster and maximized different quantities (filament mass, connected filament mass, total halo mass and galaxy richness) within a 10 Mpc h^{-1} sphere around each cluster. The resulting planes

[10]We thank G. Jungman for asking us to measure this.

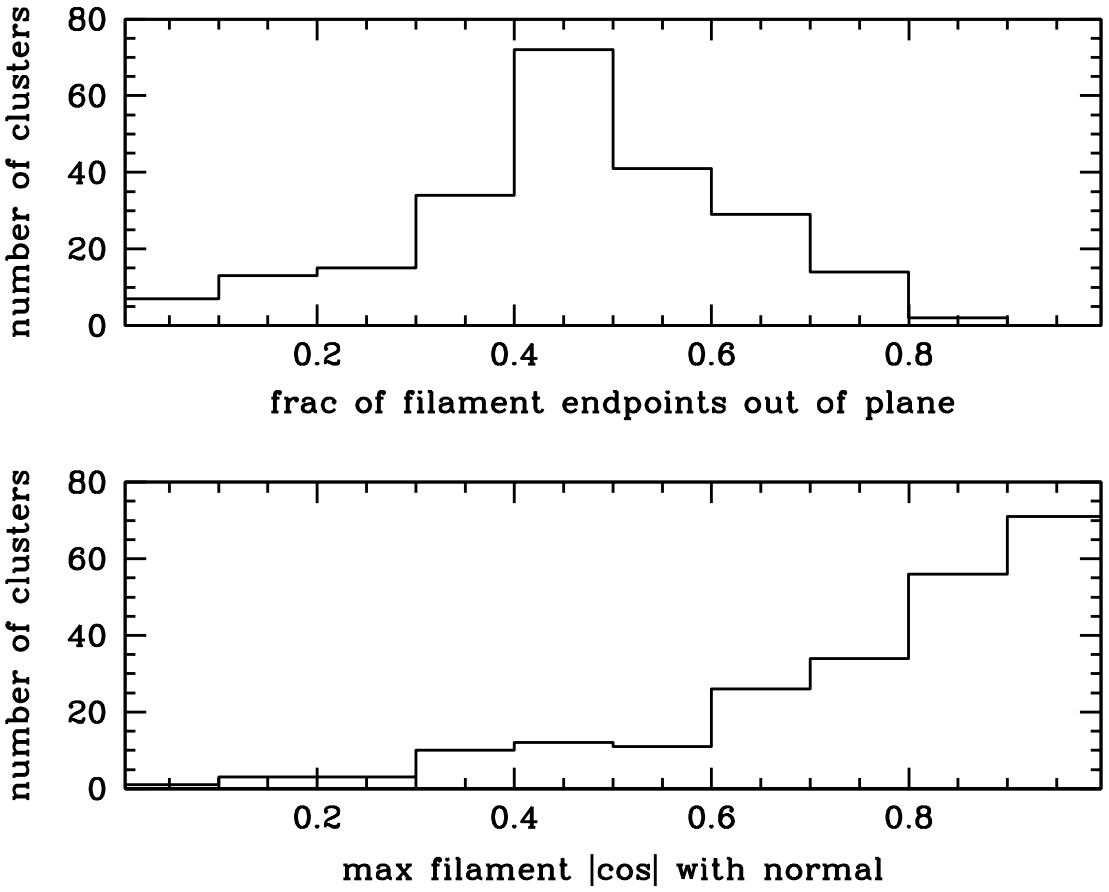

Figure 3.6: Top: fraction of filament endpoints lying outside of connected filament plane- many filaments do not have their endpoints in this plane, even though a large fraction of mass is in this plane (see Fig. 3.5). Bottom: angle to normal of connected mass plane, for filament closest to the normal; at least one filament tends to be perpendicular to this plane. The corresponding distributions for other planes are similar.

are not always aligned: the all filament plane and all halo mass plane are most likely to be aligned, and the largest disagreement between planes for any cluster is most likely to be between the connected filament plane and another plane. The long axis of the cluster tends to lie in the plane as well. Often a perpendicular filament is also present relative to the plane, with others also partially extending out of the sheet. The rough cartoon of the filament shape around clusters is a planar structure with a few filaments sticking out, with a tendency for at least one filament to be close to the plane's normal direction.

3.5 Correlated mass scatter with local filamentary planes

There are observable consequences of the filaments surrounding galaxy clusters: most cluster observations, aside from X-ray [11], will tend to include some of the cluster environment as well as the cluster itself. We saw above that the majority of the clusters have a preferred direction in their local (10 Mpc h^{-1} radius) environments, with a large fraction of their surrounding (connected or all filamentary, or total halo) mass or richness lying in a 3 Mpc h^{-1} sheet. The relation of this local structure to observables can be studied by using the mock observations described in WCS. In that work, cluster masses were measured along 96 lines of sight, using six methods mentioned earlier: two richnesses, Compton decrement, weak lensing, and two velocity dispersions. For individual clusters, WCS found correlated outliers in the mass-observable relation along different lines of sight. (It should be noted that Compton decrement and weak lensing both can have significant contamination from beyond the 250 Mpc h^{-1} path measured within the box, so correlation with the local environment is likely smaller than found in WCS and below.) Some connection with environment or intrinsic properties is seen: for the 8% of cases where at least two observables had a large ($\geq 50\%$) deviation in mass from that predicted by the mean relation, an excess of nearby galaxies from massive or less massive halos and/or substructure (as detected by the Dressler-Shectman (Dressler & Shectman 1988) test[12] were found relative to the population without these outliers. ("Nearby" in this context was taken to be within $3\sigma_{\rm kin}$ along the line of sight, where $\sigma_{\rm kin}$ was the velocity dispersion calculated via the prescription described in WCS to remove interlopers, following den Hartog & Katgert (1996); Biviano et al. (2006); Wojtak et al. (2007).)

The filamentary structures and mass planes, and the mass fraction in them, provide an additional characterization of individual cluster environments. The WCS mock observations along the 96 lines of sight of each cluster can now be compared to $|\cos\theta|$, where θ is the angle between the line of sight and the normal to these planes. In addition to the normal to four of the planes mentioned above (connected filament mass, filamentary mass, halo mass, and galaxy richness above $0.2L_*$), we also consider a fifth preferred direction, the angle to

[11] X-ray structure might have some correlation as well, inasmuch as X-ray substructure is related to filaments which provide the cluster's infalling material.

[12] within a radius r_{180b}, i.e. within which the average overdensity is 180 times the background density

the nearest filament, and in this case use $|\sin\theta_{\rm fil}|$ of this angle (i.e. $|\cos\theta|$ of the associated normal to the nearest filament).

The rough expectation is that a cluster's measured mass along the sheet with the most filamentary mass or total halo mass ($|\cos\theta| \sim 0$) will be larger than that along the plane's normal vector. This correlation is not expected to be perfect, as there is often a filament close to the normal, and the fraction and distribution of mass in the plane can vary. In particular, the planes aren't necessarily completely filled, and some directions through this plane might not intersect large amounts of mass (i.e. there might be a lack of isotropy in the plane as mentioned earlier). For planes which are not isotropically filled, one might thus expect a triangular distribution of mass prediction (on the x-axis) vs. $|\cos\theta|$ (on the y-axis): with low mass values for all $|\cos\theta|$, and high mass values for small $|\cos\theta|$ (along the plane). In addition, planes were defined only within 10 Mpc h^{-1} of the cluster, or less: for mass measurements, interlopers sometimes at 10 times or more of that distance can induce scatter. These factors suggest that the alignment of an observational direction with a sheet may not be highly noticeable in observations, even if most of the local (filamentary and/or halo) mass lies within this sheet.

Even with these contraindications, for many clusters we found a strong correlation for many mass measures with the angle between the line of sight and the locally defined planes. These strong correlations are seen not only for both measures of richness, which in principle are closely localized to the cluster, but also for weak lensing, and to a lesser extent, SZ. Correlations are both less frequent and less strong for velocity dispersions. We show an example of one cluster's mass scatter for the six observables in Fig. 3.7. The measured mass is calculated using scaling from the mean mass-observable relation for clusters in the simulation with $M \geq 10^{14}h^{-1}M_\odot$, and its value is shown versus $|\cos\theta|$, where θ is the angle between the observational direction and the connected filament plane's normal. The six panels show two richnesses, SZ, weak lensing, and two velocity dispersions. This $2.7 \times 10^{14}h^{-1}M_\odot$ cluster, with 9 filaments, exhibits strong correlations for all six measurements. It has 84% of its connected filament mass and 72% of its halo mass in the connected filament plane.

Given the noisiness of the data, we are mostly interested in general qualitative trends for the full set of 226 cluster nodes. We estimate correlations for each cluster in two ways. One is to use the correlation coefficient for $(\log M, |\cos\theta|)$, or the truncated set of points by the procedure described below, if that gives a lower absolute value (i.e. weaker value) for the correlation coefficient. These are shown for our example in Fig. 3.7 above. By eye, a correlation of < -0.25 appears to be a strong correlation, between -0.25 and 0.25 is often (not always) extremely noisy, and a correlation > 0.25 indicates an (unexpectedly) positive correlation. We use this division hereon. A positive correlation is unexpected as this means that measured cluster mass increases as the line of sight intersects less of the preferred plane.

The distributions of these correlation coefficients, for the respective mass measurements in Fig. 3.7 and the connected filament plane, are shown in Fig. 3.8 for all 226 cluster nodes. Also printed are the number of clusters with strong (negative), noisy and positive correlations for each measurement. The results are similar for all 5 choices of plane within the

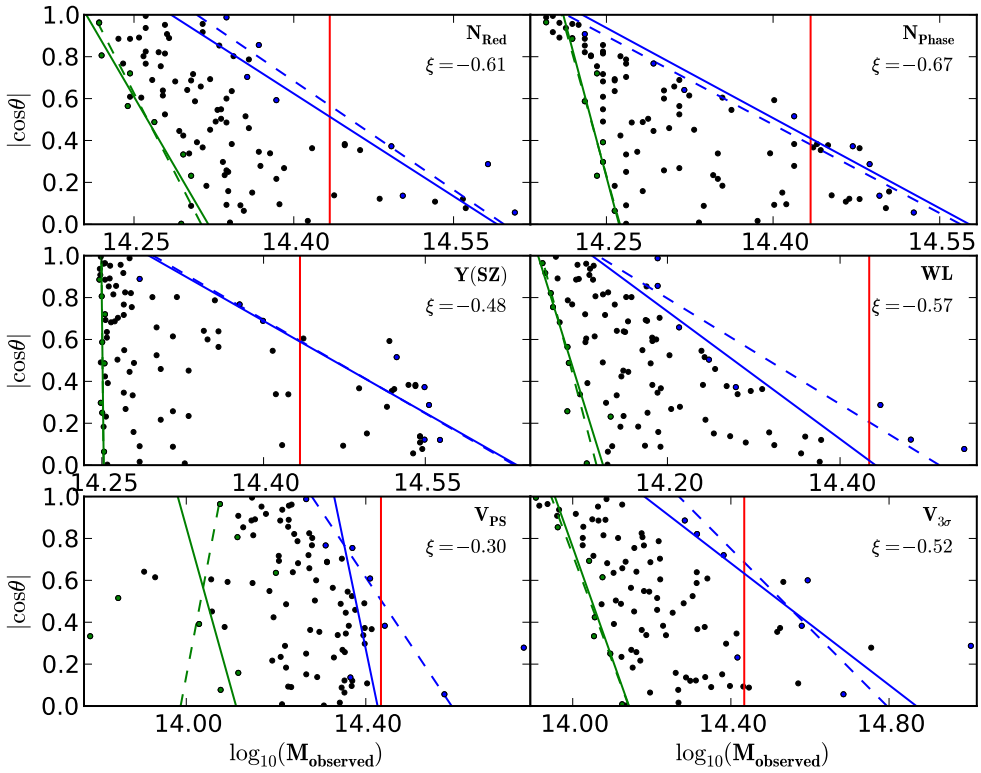

Figure 3.7: Example of mass scatter correlations: each point is a mass measurement for the same cluster along one of ~ 96 lines of sight, having angle θ with the normal of the connected filament plane. The vertical line gives the true mass. The mass measurements are based upon (left to right, top to bottom): red galaxy richness, (MaxBCG (Koester et al. 2007) algorithm, for color assignment description see text), phase space richness (galaxies "in" or "out" of cluster using criteria of Yang et al. (2008)), Compton decrement, weak lensing, phase based velocity dispersions and 3-σ clipping velocity dispersions. The mass axes for each measurement vary to cover the range of masses found for that technique, note the scales differ. Envelopes are fit to truncated sets of these points, both using a chi-squared fitting (dashed line) and a shortest perpendicular distance to the envelope (solid line), as described in the text. Where the two severely disagree (e.g. lower left hand box), one or both fits are bad. The correlation coefficients between $|\cos\theta|$ and $\log_{10} M/\mathrm{h}$ are shown at upper right, they are the smallest in absolute value of of those for all or truncated points., or the truncated points. The cluster has mass $2.7 \times 10^{14} M_\odot/h$, 9 filaments, and about 84% of its connected filament mass in the connected filament plane.

considerable noise.[13] The fraction of clusters having strong negative or positive correlations, split according to type of mass measurement, is shown in table 3.1, with ranges shown for the 5 choices of plane. The composite correlation of $\log M_{\rm true} - \log M_{\rm pred}$ for all the clusters with $|\cos\theta|$ followed similar trends, with a strongest correlation coefficient for both richnesses, then weak lensing; velocity dispersions and SZ are all similarly low. The amount of correlation between line of sight and normal to various planes is correlated to some extent with the fraction of mass or richness in these planes, as might be expected. There is also a correlation between the strength of correlations of $(\log M, |\cos\theta|)$ and the alignments between planes for each cluster (not surprisingly, this depends upon the pair of planes being considered and the plane used to defined θ). Considering multiwavelength measurements together for each cluster, ∼40-50% of the clusters have a strong negative correlation (i.e. the expected sign) for at least 3 observables.

For the planes, the correlation coefficient sometimes is low, even with a visible trend of measured mass versus $|\cos\theta|$. One apparent cause is the expected triangular envelope for the points described above. To identify this pattern, we considered slopes of approximate envelopes of the distributions, shown in Fig. 3.7. Points are binned in 8 approximately equally filled[14] $|\cos\theta|$ bins, in each bin ≤ 2 points are discarded at large or small $\log M$ if separated from their nearest neighbor by more than 6 times the median separation in mass in that bin (or the minimum separation if the median is zero). This threw out many of the notable outliers. It also sometimes threw out other points, in a binning dependent way, but the number these points is small and not a concern as we are interested in average overall properties. Points within 3σ of the median $\log M$ are then kept within each $|\cos\theta|$ bin. Straight line envelopes were then fit to both ends of each bin, either by minimizing perpendicular distance to the envelope or minimizing the chi-squared (note of $\log M(|\cos\theta|)$). Envelopes for both methods are shown in Fig. 3.7, the cases shown where they strongly disagree correspond to one or both envelopes having bad fits. From hereon we restrict to envelopes based upon minimizing the perpendicular distance to the envelope. The resulting right and left hand inverse slopes are correlated with the correlation coefficents of $(\log M, |\cos\theta|)$, their mean relation gives a correspondence between our correlation coefficient cutoff ± 0.25 and inverse slopes of the envelopes. We explored adding clusters to the negative (or positive) correlation sample which have inverse slopes less than (or more than) the mean value of inverse slope for our correlation coefficient cutoff ± 0.25; the small effect can be seen in table 3.1. (Sometimes the mean value had the wrong sign, e.g. for velocity dispersions for some choice of plane, which have large scatter, in this case the cutoff was set to zero.) We strove to be conservative

[13] Relative to the connected filament plane shown, all other planes have more strong negative correlations for the two richness based masses; for planes besides the plane perpendicular to then nearest filament (which is lower), there are more strong correlations for weak lensing and Compton decrement, and similar numbers for velocity dispersions. The plane perpendicular to the nearest filament has fewer negative correlations for weak lensing and Compton decrement and many fewer for velocity dispersions. For all 6 mass measurements, the median correlation for the plane perpendicular to the nearest filament is weaker (i.e. more positive) than for the other four planes, by more than the scatter between the median correlations for other four.

[14] As mentioned earlier, lines of sight where a more massive cluster is present within r_{180b} are discarded.

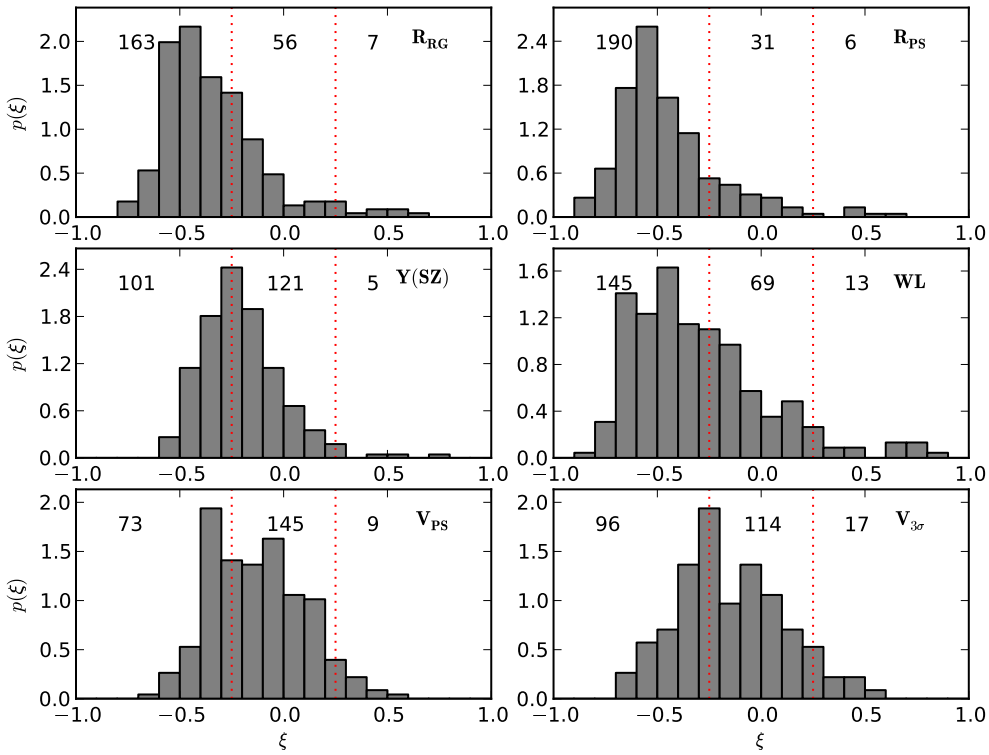

Figure 3.8: Distributions of correlations between measured mass and $|\cos\theta|$ for the 226 cluster nodes, for six observables. Here θ is the angle between the line of sight and the normal to the connected filament plane. The correlation for each cluster is taken to be the one which is minimum in absolute value for all points or the truncated (as described in the text) set of points. The mass measurement methods are as in Fig. 3.7, i.e., left, right, top to bottom are red galaxy richness, phase space richness, Compton decrement, weak lensing, velocity dispersion using spatial information and 3σ clipping velocity dispersion. Also printed for each method are (left) the number of clusters with correlation < -0.25, (middle) the number of clusters where the correlation's absolute value is less than 0.25 (and thus possibly noise), and (right) the number of clusters where the correlation is > 0.25, i.e. both positive and large, indicating a higher mass estimate as the line of sight becomes more perpendicular to the maximal plane. The dashed vertical lines separate these three regions.

property	red richness	phase rich	SZ	weak lensing	phase v	3σ v
corrln < -0.25	70-80%	85-90%	35-50%	55-75%	20-40%	25-40%
corrln < -0.25 or neg rh slope	75-85%	85-95%	40-55%	65-75%	25-40%	30-40%
inertia corrln <-0.25	80-85%	75-80%	40-50%	>90%	35-45%	55%
corrln > 0.25	≤3%	≤3%	≤2%	1-6%	1-5%	2-7%
corrln > 0.25 or large rh pos slope	$1-4\%$	$2-5\%$	$\leq 3\%$	4-10%	4-9%	2-7%
ill defined slopes	5%	~ 0	~ 0	~ 0	45-50%	50-60%

Table 3.1: Cluster fractions with strongly negative (expected, rounded to the nearest 5%) and positive (unexpected, not rounded) correlation coefficients between $|\cos\theta|$ and measured mass, by observable, for filament planes, and effect of also considering the inverse slope of the right hand ("rh") envelopes of the $(\log M, |\cos\theta|)$ relation, when either strongly negative (expected) or positive (unexpected). and for directions associated with cluster inertia tensor. The range of values encompass those for planes defined with connected filament mass, all filamentary mass within 10 Mpc h^{-1} sphere, all halo mass within 10 Mpc h^{-1} sphere, galaxy richness, and the plane whose normal is perpendicular to nearest filament to line of sight. Also shown for planes are fractions of clusters with badly defined envelopes ("ill-defined slopes"–suggesting no correlation). The range for strongly negative correlations with two directions of the inertia tensor of the cluster itself (long axis of cluster, using $\sin\theta$, or direction of eigenvector with largest eigenvalue) is also shown, see below in text.

in claiming a correlation, so that our estimates for the strength of these planar orientational effects tend to be lower bounds.

Most of the time the envelopes found by our algorithm are reasonable to the eye, but sometimes they fail catastrophically, and were caught by the goodness of fit estimator. The catastrophic failures seem to occur when no correlation is apparent between $|\cos\theta|$ and measured mass, as does an envelope close to vertical (inverse slope close to zero). The goodness of fits are the worst for the velocity dispersions, which have close to half of the clusters not allowing good fits for either the left or right envelopes, even when the goodness of fit passes threshold, the envelopes are often close to vertical: i.e. the minimum or maximum velocity dispersion mass is similar either perpendicular to the maximum plane or looking through it.

For the unexpected positive correlations, a positive inverse left envelope slope can be understood by looking down a filament near the perpendicular to the plane (small angle, large mass) and then catching a "gap" in the plane (large angle, small mass). It is more difficult to understand > 0.25 correlations or large positive right envelope inverse slopes (i.e. the largest measured mass closer to the perpendicular to the dominant plane). These do not dominate but are not uncommon: for any choice of plane, $\sim$10-20% of the clusters have at least one observable with strongly positive inverse right hand slope or correlation (almost half of these are due to velocity dispersions). This dropped to $< 5\%$ (down to 1% using the plane perpendicular to the nearest filament or richness) when requiring clusters to have at least 3 observables with either right hand positive slope or correlation (most often weak lensing and both dispersion measurements).

Restricting to correlations, which are a cleaner and more conservative measurement, there are 45 clusters with a positive correlation for at least one measurement (usually velocity dispersions). These clusters differ from the full sample in having, twice as often as the latter, high fractions of perpendicular mass to the connected filament plane and/or some pair of planes misaligned by 60 degrees or a recent merger (as defined earlier). They also slightly more often have another massive cluster within 10 Mpc h^{-1}, low mass or richness fraction in some plane, or are more flat (as measured by its inertia tensor, smallest axis/middle axis < 0.6). Fewer than a quarter of the clusters with a positive correlation for at least one measurement don't have one of these factors present, and some of these are close to our cutoffs, e.g. have more mass within 6 Mpc h^{-1} (rather than 3 Mpc h^{-1}) to the perpendicular to the connected filament plane than most clusters, or planes mismatching by almost 60 degrees. The "unexplained" strongly positive correlations occur for weak lensing and velocity dispersion mass measurements.[15] Given the complexity of the cosmic web, and the small region we use to characterize the cluster's environment, it is to be expected that our simple

[15] The fewest cases of strongly positive inverse slope or correlation occur for the plane defined using the perpendicular to the nearest filament to line of sight, suggesting that filaments close to the line of sight might be the cause of positive correlations, but again positive correlations did not always occur for these configurations. However, the plane perpendicular to the nearest filament also gives the fewest (except for richness) strongly negative correlations, i.e. its correlations are weaker in general.

cartoon description will not always correlate precisely with observables.

Similar correlations can be calculated using two axes defined from the inertia tensor for the cluster itself: the "long" axis of the cluster, corresponding to the eigenvector of the smallest eigenvalue of the inertia tensor, and the direction of the eigenvector for the largest eigenvalue of its inertia tensor (pointing orthogonal to the longest and middle axes of the cluster). As mentioned earlier, these directions are correlated with the planes, with the "long" cluster axis tending to lie within them and the latter direction tending to align with the plane normals. Compared to the five planes above, the median correlation for these two planes with mass scatter is stronger for red galaxy richness, weak lensing and the two velocity dispersions, is similar for SZ, and brackets that for phase richness (the long axis of the cluster always has the stronger correlation of the two). The strength of effect for the "long" axis of the cluster is likely due to not only a *plane* being compared to the line of sight, but a specific high density axis within that plane; almost 90% of the clusters have a strong negative correlation for at least 3 of the 6 observables. The fractions of strong negative correlations for these two directions determined by the cluster inertia tensor is also shown in table 3.1.

In summary, the mass scatter for richness, Compton decrement, weak lensing and velocity dispersion measures is often correlated with the angle to these planes (most for richnesses, and least for velocity dispersions). The correlations aren't perfect and can sometimes be weak, or even of the opposite sign than expected. In the latter case it is often also true that the different dominant planes (mass, connected or all filamentary halos, and richness) are not well aligned, or that a large filament extends perpendicular to the connected filament plane. Besides being correlated with each other, the planes and the mass scatters are also correlated with axes of the cluster's inertia tensor.

3.6 The geometry of the filamentary environment of galaxy clusters: Conclusion

After implementing a filament finder on an N-body simulation, we studied the resulting filamentary environment for the 226 nodes which are also clusters ($M \geq 10^{14} M_{\odot}/h$). Filaments tend to lie in sheets, presumably those from which they condensed, providing a highly anisotropic environment for the cluster at their center. Within a 10 Mpc h^{-1} sphere, we identified sheets of width 3 Mpc h^{-1}, centered on each cluster, which maximize either total mass, connected filament mass, all filamentary mass, or galaxy richness. The all filament and halo mass planes are most often closely aligned, while the connected filament plane tends to be within the pair of least aligned planes for the majority of clusters. The direction of the filamentary and mass planes persist slightly as the 10 Mpc h^{-1} spheres are extended to 20 Mpc h^{-1}.

We measured the correlation of mass measurement scatters with the direction of observation relative to these planes for mock observations of richness, Compton decrement, weak

lensing and velocity dispersions, via correlation coefficients and fits to the envelopes of the measurements. Often there is a strong correlation between measured mass and direction to the local plane, in spite of the relatively small region (10 Mpc h^{-1} radius) used to define the plane (again, this correlation might be overestimated for Compton decrement and weak lensing, which both can have strong scatter from distances larger than our box size). Strong correlations are least likely for velocity dispersions, and fitting envelopes to their distribution of $|\cos\theta|$ versus $\log M$ tend to fail badly. This is perhaps not surprising because our finder doesn't include dynamical information. Alignments of observational direction with two of the axes of the inertia tensor of the cluster also results in strong correlations with measured mass scatter.

How these planes and correlations with scatter extends to higher redshift depends upon how the finder extends to higher redshift. This is a subtle question as the finder of Zhang et al. (2009) has a built-in scale: a cutoff for minimum halo mass. A full analysis of appropriate generalizations is beyond the scope of this paper; two natural possibilities, however, are to leave the minimum mass alone, or to choose a minimum mass so that the ratio of the number of halos to the number of clusters (107 at $z = 0.5$, 25 at $z = 1.0$) remains the same, which gives a minimum mass of $8.2 \times 10^{10} h^{-1} M_\odot$ for $z = 0.5$ and $3.0 \times 10^{11} h^{-1} M_\odot$ for $z = 1.0$.[16] Choosing the latter case (and luminosity cut at $0.2L^*$), most of the trends persist to these higher redshifts, although the total number of filaments in the box decreases. For $z = 0.5$ and $z = 1.0$, the planar mass fractions around clusters are close to unchanged. For all 3 redshifts, there is a slight drop in richness fraction in the richness plane as redshift increases, and the halo mass fraction in planes around random points appears to grow, so that by $z = 1.0$ it is comparable to that around the 25 clusters in the box at $z = 1.0$. For correlations of plane directions with cluster observations, the statistics are very noisy for $z = 1.0$. For $z = 0.5$, the fractions of clusters with strong (expected) negative correlations of angle with plane and mass scatter[17], as in table 3.1, tend to either remain the same in range or slightly increase (velocity dispersions do decrease in one case). In addition, the number of clusters with at least three negative correlations are close to unchanged for three planes, dropping for the richness and nearest filament planes, and positive correlation fractions are about the same except for (an increase for) velocity dispersions. Large plane misalignments are less common, but clusters with misaligned planes still are more likely to have smaller mass fractions in the plane or more perpendicular mass than the full sample.

It would be interesting to determine whether this generalization to higher redshift is appropriate and then to understand the results in terms of the evolution of the filamentary neighborhood of the clusters and the clusters within them.

The correlations between mass scatter and angle of observation with the planes (and inertia tensor of the cluster) rely upon three dimensional information available to us as simulators. It would be very interesting to find a way to make this source of mass bias more

[16] We thank M. White for this suggestion.

[17] The model for colour assignments is valid only for $z = 0.1$, so we did not consider red galaxy richness at other z.

evident to observers, perhaps by using a filament finder based upon galaxies directly (amongst those mentioned earlier), and seeing how well they trace these planes, or by combining multiwavelength measurements. In depth studies underway of cluster environments such as Lubin et al. (2009) would be excellent datasets to apply and refine such methods.

Chapter 4

Disentangling correlated scatter in cluster mass measurements

The challenge of obtaining galaxy cluster masses is increasingly being addressed by multiwavelength measurements. As scatters in measured cluster masses are often sourced by properties of or around the clusters themselves, correlations between mass scatters are frequent and can be significant, with consequences for errors on mass estimates both directly and those obtained via stacking. Using a high resolution $250h^{-1}Mpc$ side N-body simulation, combined with proxies for observational cluster mass measurements, we obtain mass scatter correlations and covariances for 243 individual clusters along ~ 96 lines of sight each, both separately and together. Many of these scatters are quite large and highly correlated. We use principal component analysis (PCA) to characterize scatter trends and variations between clusters. PCA identifies combinations of scatters, or variations more generally, which are uncorrelated or non-covariant. The PCA combination of mass measurement techniques which dominates the mass scatter is similar for many clusters, and this combination is often present in a large amount when viewing the cluster along its long axis. We also correlate cluster mass scatter, environmental and intrinsic properties, and use PCA to find shared trends between these. For example, if the average measured richness, velocity dispersion and Compton decrement mass for a cluster along many lines of sight are high relative to its true mass, in our simulation the cluster's mass measurement scatters around this average are also high, its sphericity is high, and its triaxiality is low.

Our analysis is based upon estimated mass distributions for fixed true mass. Extensions to observational data would require further calibration from numerical simulations, tuned to specific observational survey selection functions and systematics. [1]

[1] This chapter has been previously published as Noh & Cohn (2012), and is reproduced with the permission of all coauthors and the copyright holder.

4.1 Disentangling correlated scatter in cluster mass measurements: Introduction

Although there is no question that galaxy clusters are the most massive virialized objects in the universe, identifying the mass of any particular cluster remains a challenge. A cluster's mass is however one of its core properties, important for using cluster samples statistically to constrain cosmological parameters, for understanding clusters as hosts for galaxy evolution, and for studying the growth and other properties of the clusters themselves. Recent reviews include Voit (2005); Borgani (2008); Myers et al. (2009); Allen et al. (2011).

In simulations, the cluster mass is simply the mass of the simulation particles making up the cluster, in whichever cluster mass definition is used (comparisons of some mass definitions are found in, e.g., White (2001, 2002); Hu & Kravtsov (2003); Cuesta et al. (2008); Lukić et al. (2009)). From a given cosmological set of parameters, simulations predict well defined and directly measurable masses, accurate to the extent that the simulation captures the required physics and has the requisite resolution. These theoretical mass definitions cannot be directly applied to observational data, as observations instead measure properties of galaxies both within the cluster and near the cluster, or gas within and sometimes near the cluster, or the bending of space by mass in and around the cluster. These observational mass proxies are converted, via physical modeling and assumptions, to mass measurements for comparison with theory. Improvements in the noisy mappings between observationally accessible cluster properties and theoretically calculable cluster properties is much sought after by both theorists and observers. Complications for observations include projection (and more generally the lack of three dimensional information[2]) and reliance of the mapping between mass and observational proxy upon simplifying assumptions such as hydrostatic equilibrium. The simulation based theoretical approaches, for their part, find it challenging to capture the directly observable baryonic physics, including galaxy properties.

In order to alleviate systematics and reduce errors in observationally obtained cluster masses, it is becoming common to combine measurements from different (often multiwavelength) observational techniques. The advantages of complementary information and cross-checks are unfortunately mitigated by the fact that scatters from different observational methods are often correlated. Essentially, as physical properties of the clusters themselves and their environments are often the causes of mass measurement scatters, more than one

[2]There is a long history, e.g. for optical cluster richness starting with Abell (1958) and continuing with, for example, Dalton et al. (1992); Lumsden et al. (1992); van Haarlem et al. (1997); White et al. (1999); Cohn et al. (2007); Cohn & White (2009); Rozo et al. (2011); Biesiadzinski et al. (2012), for cluster weak lensing, e.g., Reblinsky & Bartelmann (1999); Metzler et al. (2001); Hoekstra (2001); de Putter & White (2005); Meneghetti et al. (2010); Becker & Kravtsov (2011); Hoekstra et al. (2011), for cluster Sunyaev-Zel'dovich (Sunyaev & Zeldovich 1972, 1980) (SZ) flux measurements, e.g., White et al. (2002); Holder et al. (2007); Hallman et al. (2007); Shaw et al. (2008); Angulo et al. (2012) and for cluster velocity dispersions, e.g., Cen (1997); Tormen (1997); Kasun & Evrard (2005); Biviano et al. (2006); White et al. (2010); Saro et al. (2013)).

measurement technique can be affected. It is important include these correlations in order to properly estimate the errors in mass measurements of any individual cluster and to avoid a bias when stacking clusters on one property and measuring another. (For discussion see Rykoff et al. (2008); Cohn & White (2009); Stanek et al. (2010); White et al. (2010), additional simulated examples of correlated scatters using different observational methods include Meneghetti et al. (2010); Rasia et al. (2012); analyses are beginning to include these, e.g. Rozo et al. (2009); Mantz et al. (2010); Benson et al. (2013).). A recent application to an observational cluster sample, resolving some questions raised by earlier analyses is found in Angulo et al. (2012).)

Here we consider multiwavelength mass measurements for clusters "observed" in a cosmological dark matter simulation. Our primary focus is on mass scatters for individual clusters viewed along several different lines of sight. We measure and characterize the multiwavelength correlations and covariances, and study their relation to other cluster properties using both correlations and PCA, principal component analysis. This extends recent work using PCA to compare relationships between cluster (Skibba & Macciò 2011; Jeeson-Daniel et al. 2011) properties such as concentration, mass and ellipticity in simulations, and some supercluster counterparts, Einasto et al. (2011, 2012), in observations.[3]

The mass observables we simulate are red galaxy richness, phase space richness, velocity dispersions, Sunyaev-Zel'dovich decrement and weak lensing ζ statistic (Fahlman et al. 1994; Kaiser 1995), techniques in use or planned for large volume current and upcoming cluster surveys such as ACT [4], SPT[5], BCS[6], DES[7] and LSST.[8]

The mock simulation measurements, their scatters, and general information about PCA are in §2. (Much of §2 summarizes work on the same simulation detailed in White et al. (2010) (hereafter WCS), and further studied in Noh & Cohn (2011) and Cohn (2012).) In §3, mass scatters for each cluster, along ~ 96 lines of sight, are correlated, and their covariances are analyzed via PCA. Distributions of the scatter properties are considered, and, cluster by cluster, the PCA direction of largest scatters is compared to special physical cluster directions. In §4 cluster properties, including the individual cluster mass scatter distributions, and environmental and intrinsic properties, are intercompared using correlations and PCA. In §5 PCA is instead applied to mass scatter for the whole sample of clusters at once, to analyze scatter including both line of sight and cluster-to-cluster variation, with some discussion of possible extensions to observations. §6 discusses outliers and §7 summarizes.

While we were preparing this work for publication, Angulo et al. (2012) appeared. They consider correlated mass scatter in multiwavelength measurements, in a 4.1 Gpc side simu-

[3]Comparing cluster mass scatters to physical cluster properties has a long history, recent studies include Yang et al. (2010); Becker & Kravtsov (2011); Battaglia et al. (2012); Bahé et al. (2012), as well as papers mentioned above.

[4]www.physics.princeton.edu/act/

[5]pole.chicago.edu

[6]cosmology.uiuc.edu/BCS/

[7]www.darkenergysurvey.org

[8]www.lsst.org/

lation which also includes X-ray.

4.2 Disentangling correlated scatter in cluster mass measurements: Simulations and Methods

4.2.1 N-body data

Our simulation data are the outputs of an N-body simulation of M. White, described in detail in WCS. His TreePM (White 2002) code was run with 2048^3 particles in a periodic box with side length 250 $h^{-1}Mpc$. The 45 outputs are equally spaced in $\ln(a)$ from $z = 10$ to $z = 0$. Cosmological parameters were taken to be $(h, n, \Omega_m, \sigma_8) = (0.7, 0.95, 0.274, 0.8)$, consistent with a large number of cosmological observations. We focus here on mock observations at $z = 0.1$, where our methods have been most closely tuned to and tested with observational data, as reported in WCS. Halos are found via Friends of Friends (FoF) (Davis et al. 1985), with linking length $b = 0.168$ times the mean interparticle spacing (connecting regions with density at least roughly 100 times the mean background density). Clusters are halos with FoF masses $M \geq 10^{14}h^{-1}M_\odot$ (M hereon will mean this $b = 0.168$ FoF mass, we will also write this as $M_{\rm true}$ when comparing to estimates). There are 243 clusters in the box. Note that because we have a periodic box we do not need to worry about clusters located near the edge, similarly, because we are using FoF as a halo finder, every particle is uniquely assigned to a single halo.

Galaxies are taken to be resolved subhalos, which are found via Fof6d (Diemand et al. 2006), with the implementation as described in the appendix of WCS. Subhalos are tracked (see Wetzel et al. (2009); Wetzel & White (2010) for particular details) from their infall into their host halos in order to assign luminosities via subhalo abundance matching (Conroy et al. 2006). The resulting galaxy catalogue minimum luminosity at $z = 0.1$ is $0.2L_*$ (again see WCS for more discussion and validation tests of the catalogue galaxy properties with observations).

4.2.2 Cluster mass measurements and scatters

We consider five cluster mass measurement methods with this simulation (see WCS for specifics):

- $N_{\rm red}$: Richness using the Koester et al. (2007) MaxBCG algorithm based upon colors. Color assignments are estimated using the prescription of Skibba & Sheth (2009) with evolution of Conroy et al. (2009, 2010); Conroy & Gunn (2010). Galaxies are taken to be "red" if they have $g - r$ within 0.05 of the peak of the red galaxy $g - r$ distribution specified by Skibba & Sheth (2009) for their observed M_r, again see WCS for more detail.

- $N_{\rm ph}$: Richness based upon spectroscopy, with cluster membership assigned via the criteria of Yang et al. (2008).

- SZ: SZ flux (Compton decrement) is assigned to every particle by giving it a temperature based upon the mass of its halo. For every cluster, its measured SZ flux is then the flux within an annulus of radius r_{180b} (the radius within which the average mass is greater than or equal to 180 times background density), through the length of the box, apodized at the edges. This was shown in e.g. White et al. (2002) to well approximate hydrodynamic simulation results for SZ at the scales appropriate for two cluster surveys mentioned earlier, SPT and ACT.

- Vel: Velocity dispersions calculated via the method detailed in WCS, and based on den Hartog & Katgert (1996); Biviano et al. (2006); Wojtak et al. (2007). Phase space information is used to reject outliers and the mass estimate includes the harmonic radius (calculated as part of the outlier rejection, more details and definitions in WCS).

- WL: Weak lensing using an SIS or NFW model to assume a cluster lens profile and then fitting the projected mass, using the ζ statistic (Fahlman et al. 1994; Kaiser 1995), in a cylinder with radius r_{180b} and (apodized) length of the box (again WCS describes fitting models, etc.).

The red galaxy richness, phase space richness and velocity dispersions measured in our simulations are expected to include the majority of systematics that are present in real observations. The weak lensing and Compton decrement (SZ) observations however do not include all known systematics, such as miscentering, shape measurement and source redshift errors for lensing, and foreground and point source removal for Compton decrement. The relatively small box size (250 $h^{-1}Mpc$ on a side) also means that line of sight scatter is underestimated (e.g., White et al. (2002); Hallman et al. (2007); Holder et al. (2007); Cohn & White (2009); Angulo et al. (2012) for SZ and Reblinsky & Bartelmann (1999); Metzler et al. (2001); Hoekstra (2001); de Putter & White (2005); Meneghetti et al. (2010); Becker & Kravtsov (2011); Bahé et al. (2012); Hoekstra et al. (2011) for lensing).

We extend the cluster sample used in WCS to a lower mass range , $M \geq 10^{14}h^{-1}M_{\odot}$, as in Noh & Cohn (2011); Cohn (2012). The five observables listed above are found along 96 lines of sight for each cluster, each time placing the cluster at the center of the periodic box. Just as in WCS, lines of sight for clusters are removed for all measurement methods when a more massive cluster has its center within r_{180b} along the line of sight (this removes ~ 400 of the original $\sim$23000 lines of sight). In addition, to allow fair intercomparisons, only lines of sight which have reliable mass measurements for all methods are included; the ~ 90 lines of sight with fewer than 8 galaxies making the cut for a velocity dispersion estimate, or either richness < 1.1 are also removed. These cuts will have some effect on the scatters we consider but would be expected to be identifiable observationally.

We take the logarithm of these observables and that of the true mass M to find the mean relations for all clusters with $M \geq 10^{14}h^{-1}M_{\odot}$. We find relations for bins of M vs.

observables, because of the large scatter at low mass. The fits are done by throwing out 3 σ outliers for three iterations. This gives us our map between the observables and mass estimates $M_{N_{\rm red}}, M_{N_{\rm ph}}, M_{\rm SZ}, M_{\rm Vel}, M_{\rm WL}$.

The distribution of the fractional mass scatters, $(M_{\rm est} - M_{\rm true})/M_{\rm true}$, for the five mass measurement methods along $\sim$ 96 lines of sight for each of the 243 clusters, is shown in Fig. 4.1. The scatters range from $\sim$ 0.2-0.5, with the smallest mass scatters associated with Compton decrement[9] and $N_{\rm ph}$. Note that this work follows a theoretical approach where all the mass measurements are related to the known true mass, a quantity inaccessible in observations. In particular, the sample is cut on the unobservable value of $M_{\rm true}$ and the distributions we consider are $M_{\rm est}(M_{\rm true})$, not vice versa.[10] For an observational sample based upon some measurement $M_{\rm est}$, such as richness mass or weak lensing mass, often the quantity of interest is the scatter in $P(M_{\rm true}|M_{\rm est})$ (see also extended comments in §4.5).[11]

4.2.3 Filaments and Galaxy Subgroups

In section §4.4, cluster filament properties calculated in Noh & Cohn (2011) and cluster galaxy subgroup properties calculated in Cohn (2012) for this simulation are used. Detailed background can be found in those two papers, but we briefly summarize some key aspects here.

Filaments are found in Noh & Cohn (2011) using a modification of the dark matter halo based filament finder of Zhang et al. (2009).[12] This filament finder searches for bridges 10 $h^{-1}Mpc$ or smaller between halos above $3\times10^{10}h^{-1}M_{\odot}$, starting with the most massive halos as potential bridge endpoints. Some clusters (16/243) end up within filaments because of the finder, such as less massive clusters located between two close ($< 10h^{-1}Mpc$) massive clusters and clusters closer than $3h^{-1}Mpc$ to a larger cluster. The rest of the clusters each lie at the center of a filament map extending out to 10 $h^{-1}Mpc$. We found that filaments, halo mass

[9]Recall the caveats for both SZ and weak lensing measurements mentioned earlier, however.

[10]We thank E. Rozo for extremely helpful discussions on this.

[11]For example, the richness mass scatter in Fig. 4.1, looks essentially Gaussian, unlike the double peaked distribution found and studied in e.g. Cohn et al. (2007); Erickson et al. (2011). If looking at $P(M_{\rm true}|M_{\rm est})$, one will find clusters which are "blends", i.e. several halos which contribute to one apparent halo, often with a higher $M_{\rm est}$ than any of the contributing halos. These blends (see also e.g. Gerke et al. (2005) for discussion) are the source of the bimodal mass distribution reported and used in these other papers.

[12]Although the cosmic web was noted years ago (Zeldovich et al. 1982; Shandarin & Zeldovich 1983; Einasto et al. 1984; Bond et al. 1996), no unique filament finder exists. A variety of finders are in use, based on a wide range of dark matter, halo and/or galaxy properties, including for example Barrow et al. (1985); Mecke et al. (1994); Sahni et al. (1998); Schmalzing et al. (1999); Colombi et al. (2000); Sheth et al. (2003); Colberg et al. (2005); Pimbblet (2005a,b); Stoica et al. (2005); Novikov et al. (2006b); Aragón-Calvo et al. (2007a); Colberg (2007); Hahn et al. (2007b); van de Weygaert & Schaap (2007); Sousbie et al. (2008a); Stoica et al. (2010); Bond et al. (2010a); Forero-Romero et al. (2009); González & Padilla (2010); Pogosyan et al. (2009); Sousbie et al. (2009); Wu et al. (2009); Zhang et al. (2009); Aragon-Calvo et al. (2010); Aragón-Calvo et al. (2010); Bond et al. (2010b); Genovese et al. (2010); Murphy et al. (2011); Sousbie (2011); Way et al. (2011); Shandarin (2011); Shandarin et al. (2012); Smith et al. (2012); Jasche & Wandelt (2013).

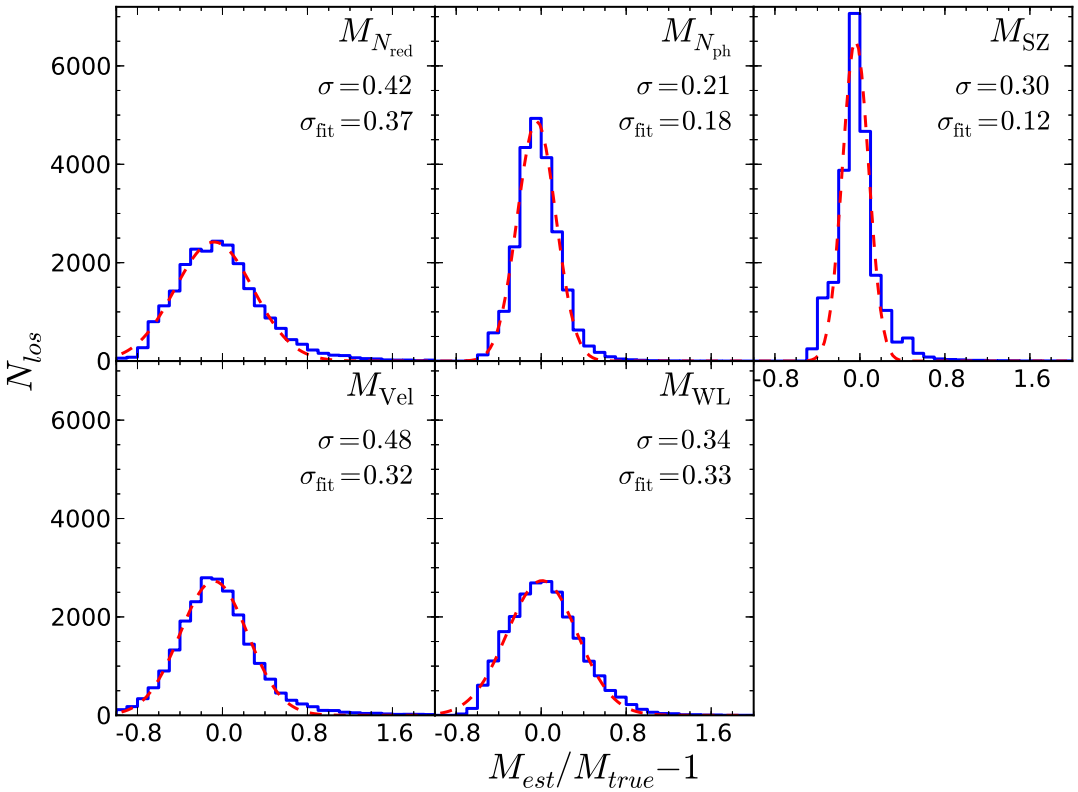

Figure 4.1: The fractional mass scatter, $M_{\rm est,i}/M_{\rm true} - 1$ for all 243 clusters along ∼96 lines of sight each, for the five mass measurement methods we consider. Solid lines are the masses estimated via $N_{\rm red}$,$N_{\rm ph}$, SZ (Compton decrement), velocity dispersion and WL (weak lensing) as described in the methods section. An approximately 0.2-0.5 standard deviation is found. The (for the most part difficult to distinguish) dashed line is a least squares Gaussian fit, giving $\sigma_{\rm fit}$, which is much smaller than the standard deviation for SZ. The WL and SZ mass scatter is expected to be strongly underestimated compared to true observations, as the 250 Mpc/h box size is too small to include all contributions to mass scatter along the line of sight to the observer, and in these two cases several known systematics are not included as well. See text for more information.

(halos with mass $\geq 3 \times 10^{10} h^{-1} M_{\odot}$) and galaxy richness all tended to lie in a planar region around each cluster. We characterized these regions by taking a fiducial 3 $h^{-1}Mpc$ high disk centered on the cluster which extends out to the edge of the radius 10 $h^{-1}Mpc$ sphere. We use the planes related to halo and filament mass below. For halo mass, we randomly sampled 10,000 orientations to maximize the halo mass fraction in the plane (relative to the halo mass in the 10 $h^{-1}Mpc$ sphere). For filaments, we considered planes spanned by the cluster and pairs of filament endpoints, and then took the plane which enclosed the most filament mass. This plane was not found for clusters lying within filaments. See Noh & Cohn (2011) for more details. We consider four quantities from this analysis below: $f_{M_{hplane}}$ (halo mass fraction in plane relative to that in 10 $h^{-1}M_{\odot}$ sphere), $f_{M_{fplane}}$ (cluster filament mass fraction in plane relative to sphere), and the respective plane normal directions $\hat{n}_{\rm mass}, \hat{n}_{\rm fil}$.

Galaxy subgroups were characterized in Cohn (2012) for this simulation. These are groups of galaxies that fell into a cluster as part of a shared halo at an earlier time. Within the clusters, they share some coherence in space and time which can remain for several Gyr. We will use for each cluster its largest (richest) galaxy subgroup, in particular its fractional richness relative to that of the cluster, $f_{R_{\rm sub}}$, its displacement relative to the cluster center, divided by the cluster long axis $f_{D_{\rm Sub}}$, and the directions of its position and average velocity relative to the cluster center, $\hat{r}_{\rm sub}, \hat{v}_{\rm sub}$.

4.2.4 Principal Component Analysis

For context and background, we summarize PCA and our notation here (see, e.g. Jolliffe (2002) for extensive discussion). PCA can be used when there are several correlated or covariant quantities. It is essentially a rotation of axes to find linearly independent bases (i.e. quantities which are not covariant or correlated), and is based on a model where some underlying average linear relation is present. We will apply PCA in a few different contexts.

Our starting application will be for individual clusters. For each individual cluster and line of sight, we have several different methods to estimate the true cluster mass. Each line of sight can thus be associated with five numbers, where each number is the mass measured in one method. These numbers can then be thought of as coordinates in some five dimensional abstract space, with each axis in this space corresponding to a different measurement method. All of the different lines of sight considered together then give a cloud of points in this space of measurement methods. PCA gives the properties of the "shape" of the mass scatters in this space, around their average values for the combined observations, for each cluster. We will consider these shapes and how they relate to other cluster properties. In addition, correspondences can be found between large mass scatters and physical properties or directions of the cluster. The PCA direction with smallest mass scatter is useful as well. Taking the ensemble of clusters, groups of properties which change together can be inferred by using PCA on the full set of correlations (this latter approach was pioneered by Jeeson-Daniel et al. (2011); Skibba & Macciò (2011); Einasto et al. (2011)).

There are other uses of PCA, and caveats as well. PCA is often used to find the minimum

set of variables needed to describe a system to some accuracy, for instance the dominant contributing basis vectors composing a galaxy spectrum. As far as caveats go, one concern is that if correlated variables are not scattered around a linear relation, a simple rotation of basis using PCA will not usefully separate them. For this reason, sometimes other functions are used besides the variables themselves, e.g. logarithms, when it is suspected that variables might be related by power laws.

For illustration, we take a set hypothetical measurements for two methods, as shown in Fig. 4.2. Each pair of measurements, by the two methods, is a position, i.e. a dot, in this plane labeled by two coordinates. We take one coordinate to be the shifted mass using red galaxy richness, $M^\alpha_{N_{\rm red}} = M^\alpha_{N_{red},est} - \langle M_{N_{red},est}\rangle$, and the other to be the shifted weak lensing mass, $M^\alpha_{\rm WL} = M^\alpha_{\rm WL,est} - \langle M_{\rm WL,est}\rangle$. Here, α denotes which particular point is being measured and the average is over all the points shown, all α values, i.e. $\langle M_{N_{red},est}\rangle = \frac{1}{N_\alpha}\sum_\alpha M^\alpha_{N_{red},est}$. The vector $\boldsymbol{M}^\alpha_{\rm obs}$ denotes $(M^\alpha_{N_{\rm red}}, M^\alpha_{\rm WL})$ and N_α is the number of measurements (points) indexed by α. For our first application below, all different values of α pertain to the same cluster, but label different lines of sight. The shift by the average over all the points (all α) guarantees that $\langle M_{\rm WL}\rangle = \langle M_{N_{\rm red}}\rangle = 0$.

Diagonalizing the covariance matrix for $(M_{N_{\rm red}}, M_{\rm WL})$, i.e. found by summing over all α, produces orthonormal eigenvectors $\hat{PC}_i$ (principal components) with eigenvalues λ_i. The eigenvectors are illustrated in Fig. 4.2 and are the axes of a new coordinate system in the space of measurement methods in which the measurements have zero covariance. The $\hat{PC}_i$ can be expressed in terms of the original basis directions,

$$\hat{PC}_i = \beta_{\rm red,\,i}\hat{e}_{\rm red} + \beta_{\rm WL,\,i}\hat{e}_{\rm WL}\ , \tag{4.1}$$

which identifies the mass scatters contributing most to each $\hat{PC}_i$. For example, if $\beta_{\rm red,\,0}$ is large, then most of the scatter in the direction of $\hat{PC}_0$ also lies in the direction of $\hat{e}_{\rm red}$. One also sees how different scatters are related. In this simple example the biggest scatters come from increases or decreases in both $M_{\rm red}, M_{\rm WL}$ simultaneously. This implies, in this case, that $\hat{PC}_0$ might be related to an average overall mass shift, amongst methods, as well. Note that the overall signs for the $\hat{PC}_i$ are arbitrary.

A point (or vector from origin, labeled by α) in the original space can then be rewritten in the basis spanned by $\hat{PC}_0, \hat{PC}_1$:

$$\boldsymbol{M}^\alpha = M^\alpha_{\rm red}\hat{e}_{\rm red} + M^\alpha_{\rm WL}\hat{e}_{\rm WL} = a^\alpha_0\hat{PC}_0 + a^\alpha_1\hat{PC}_1\ . \tag{4.2}$$

For example, the point marked by a star in Fig. 4.2 has coordinates $\boldsymbol{M}^\star = 10^{14}\hat{e}_{\rm red} + 10^{14}\hat{e}_{\rm WL} = \sqrt{2}\times 10^{14}\hat{PC}_0 + 0\ \hat{PC}_1$. That is, $(M^\star_{\rm red}, M^\star_{\rm WL}) = (1,1)\times 10^{14}$ (assuming measurements are in units of $h^{-1}M_\odot$) and $(a^\star_0, a^\star_1) = (\sqrt{2}, 0)\times 10^{14}$.

The variances in each of the new directions, associated with the coefficients a^α_i, are the eigenvalues of the principal components. Thus, λ_0 is the eigenvalue associated with $\hat{PC}_0$, etc. For all PCA eigensystems we consider here, we will order $i < j$ if $\lambda_i > \lambda_j$ and define $\sum\lambda = \sum_i \lambda_i$ and $\prod\lambda = \prod_i \lambda_i$. Generally, if there are $N_{\rm method}$ measurement methods, there

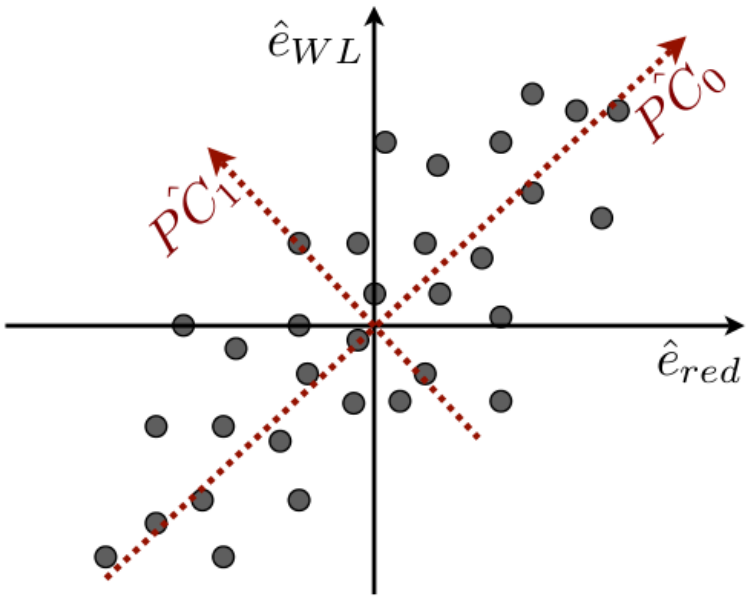

Figure 4.2: Principal component analysis takes a set of correlated measurements (using two methods shown as basis elements $\hat{e}_{\rm red}, \hat{e}_{WL}$) and rotates their coordinates to a new basis, shown as dotted lines, where the measurements are uncorrelated. For example, the point marked as a star (i.e. $\alpha = \star$) is $\boldsymbol{M}^\star = 10^{14}\hat{e}_{\rm red} + 10^{14}\hat{e}_{\rm WL} = \sqrt{2} \times 10^{14}\hat{PC}_0 + 0\ \hat{PC}_1$. The generalization to more measurement methods and thus a higher dimensional space is immediate. Amongst the orthonormal $\hat{PC}_i$, we choose $\hat{PC}_0$ to be along the direction of largest scatter (i.e. to correspond to the largest variance, λ_0), $\hat{PC}_1$ to be along the direction of second largest variance, etc., as described in the text.

are $N_{\rm method}$ $\hat{PC}_i$, spanning an $N_{\rm method}$ dimensional space. In Fig. 4.2, $N_{\rm method}$=2; when we consider the five different mass measurement methods below, for example, $N_{\rm method} = 5$. For PCA applied to different cluster properties, in §4.4.3 below, we have $N_{\rm method} = 24$. We will apply PCA to covariance and correlation matrices, using the Pearson covariance ${\rm Cov}(xy) = \frac{1}{N_\alpha - 1}\sum_{\alpha=1}^{N_\alpha}(x_\alpha - \bar{x})(y_\alpha - \bar{y})$ where $\bar{x}$ is the average of the N_α points x_α, etc., and ${\rm Cov}(x,y)/\sqrt{{\rm Cov}(x,x){\rm Cov}(y,y)}$ its associated correlation, for N_α measurements.[13]

The sum of the λ_i, $\sum\lambda$, is the sum of the variances of the measurement methods, their product, $\prod\lambda$, is related to the "volume" in this space of scatters, i.e. how the measurements are spread out in the space of measurement methods (specifically, for the example in Fig. 4.2, $\sqrt{\lambda_0\lambda_1}$ is proportional to the area of the ellipse). A small eigenvalue λ_i means that the scatter in the corresponding $\hat{PC}_i$ direction is small, i.e. that the volume of scatters is roughly confined to a lower dimension. In particular, if most of the scatter is due to λ_0, then there is a close to linear relation present. Such lower dimensionality was used in Einasto et al. (2011) to come up with scaling relations for superclusters. For PCA of correlations, a large λ_0 occurs if the initial measurements via different methods have strong correlations, for covariances, a large λ_0 can also occur if an individual measurement method has large scatter.

Measurement methods $M^\alpha_{{\rm obs},j}$ (in the example $M_{N_{\rm red}}, M_{\rm WL}$) with the largest correlation or covariance with a_i^α (their projection on $\hat{PC}_i$) can be thought of as those dominating the scatter in the direction of $\hat{PC}_i$. This covariance or correlation is not unrelated to the measurement method's contribution to $\hat{PC}_i$, ($\beta_{{\rm obs},j,i}$ in Eq. 4.1). The covariance or correlation is largest when $\beta_{{\rm obs},j,i}$ is large, and when the eigenvalue λ_i is large relative to the other $\beta_{{\rm obs},j}$'s and λ_i. (For PCA on correlations in particular, $\langle M_{{\rm obs},j}a_i\rangle/\sqrt{\langle M_{{\rm obs},j}M_{{\rm obs},j}\rangle\langle a_i a_i\rangle} \sim \beta_{{\rm obs},j,i}\lambda_i/\sqrt{\lambda_i\sum_k\lambda_k\beta^2_{{\rm obs},j,k}}$; if $\lambda_0, \beta_{{\rm obs}j,0}$ are large and a_0 is considered then this approaches 1.)

To summarize, PCA is a method taking a set of measurements via different methods which are correlated and separating them into uncorrelated combinations. In particular, if one denotes each set of measurements as a position in some space, along axes corresponding to each type of measurement method, then PCA is a rotation of coordinates in this space. The volume and shape traced out by the points representing the measurements are related to the PCA eigenvectors and eigenvalues, and the direction in the space corresponding to the largest PCA eigenvector is the combination of measurement methods with the largest scatter in its distribution.

[13] For the cluster mass scatters, as this covariance can be affected by outliers, we experimented with several outlier rejection schemes. As the resulting values were somewhat similar, and our analysis is in part just to provide an example, we use the untrimmmed Pearson covariances and correlations hereon. We also considered for some properties (as did some of the earlier cluster PCA work) the Spearman correlation. The Spearman correlation coefficient uses the ranking of the measurements rather than the raw measurements themselves. Trends were similar to the Pearson covariances and correlations.

4.3 Variations for a single cluster due to line of sight effects

As mentioned in the introduction, many of the mass measurement method scatters in Fig. 4.1 are comparable in size because they are due to similar properties of the cluster or its environment. Correlations between the scatters are thus expected, and as noted above, these correlations and their consequences become increasingly important as multiwavelength studies become more common.

We first consider each cluster and its line of sight mass scatters separately. In this way, the "true" object and its true mass remained fixed; all variations in scatters are due to changes in line of sight. Several examples of correlations for these scatters were already noted and illustrated in WCS[14], and correlations with various physical properties (discussed below) were further studied in Noh & Cohn (2011); Cohn (2012). Here we statistically describe these correlations and covariances. We characterize cluster to cluster trends and variations in line of sight mass scatters and predicted masses, and then apply PCA to these scatters.

4.3.1 Correlated mass scatters for different cluster observables

To give an idea of the correlations and covariances for our five different mass measurement methods, we start with an example: the 10 pairs of mass measurements for a single cluster ($M = 4.8 \times 10^{14} h^{-1} M_\odot$) shown in Fig. 4.3. Each panel shows a different pair of mass estimates along all lines of sight (i.e. $N_\alpha = 95$), and correlations and covariances are listed at the top of each. We use $M_{\rm est}/M_{\rm true} - 1$ to focus on fractional mass scatter. As can be seen, many of the correlations are large.

For all 243 clusters, the correlations for the same pairs of mass measurement methods are compiled in Fig. 4.4, with medians and averages given in Table 4.1. Strong correlations are frequent. For each cluster, at least one pair of mass measurement methods has correlation > 0.4, and the largest pair correlation is often larger, ~ 0.7. Within our cluster sample, the mass scatters for ($M_{N_{\rm red}}$, $M_{N_{\rm ph}}$) are most often the highest correlated pair. The other measurement method pairs which frequently have the highest correlation (but not as often as ($M_{N_{\rm red}}$, $M_{N_{\rm ph}}$)) are ($M_{N_{\rm red}}$, $M_{\rm SZ}$), ($M_{N_{\rm red}}$, $M_{\rm WL}$), ($M_{N_{\rm ph}}$, $M_{\rm SZ}$) and ($M_{N_{\rm ph}}$, $M_{\rm WL}$). The minimum correlation is between ($M_{\rm Vel}$, $M_{\rm WL}$) (closely followed by ($M_{\rm Vel}$, $M_{\rm SZ}$), and ($M_{\rm Vel}$, $M_{N_{\rm ph}}$)).

For our PCA analysis below, we will use covariances instead, shown in Fig. 4.5, with medians and averages given in Table 4.1. These are more relevant for understanding the actual mass scatters and how they change together, rather than, for example, how much a relatively large $M_{\rm SZ}$ mass scatter corresponds to a relatively large $M_{N_{\rm red}}$ mass scatter. As the fractional mass fluctuations (the σ values in Fig. 4.1) tend to be about 0.3, the covariance

[14] e.g. an example of correlations between velocity dispersion and weak lensing measurements are shown in WCS Fig. 14

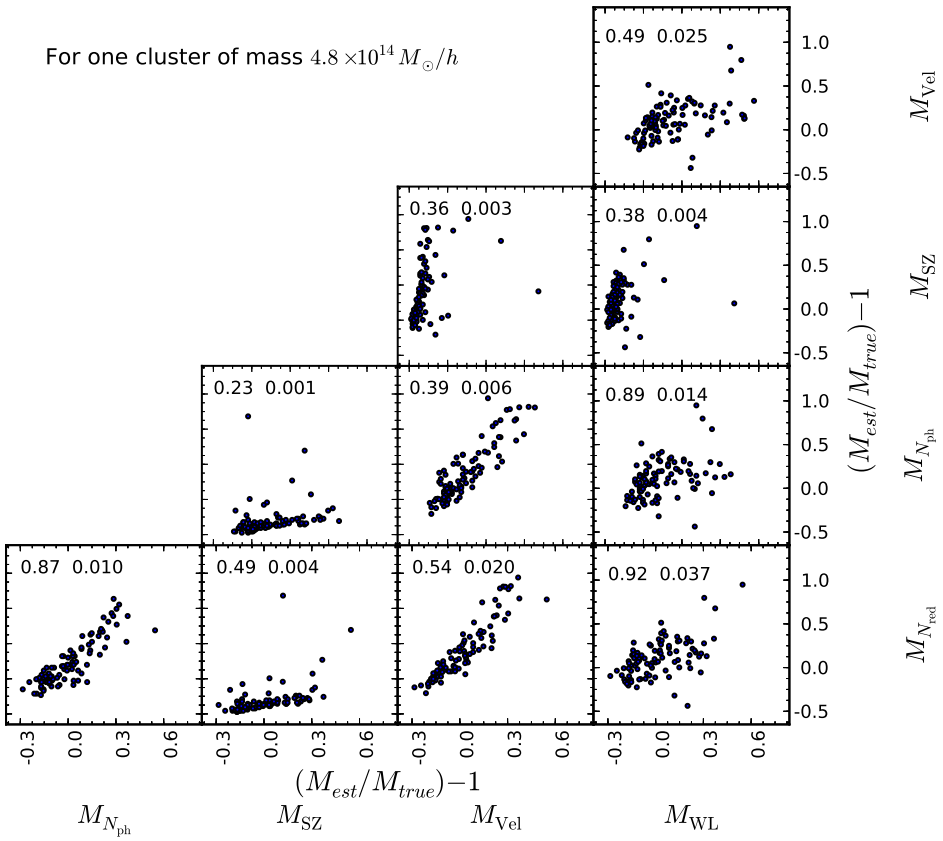

Figure 4.3: Cluster mass scatters ($M_{\rm est}/M_{\rm true} - 1$) for one cluster of mass $4.8 \times 10^{14} h^{-1} M_\odot$, along 95 lines of sight. The correlation and covariance for each mass measurement method pair is shown at the top of each panel (the y-axis is for a larger scale to allow room for these numbers). Large correlations are present for many pairs of mass measurement methods.

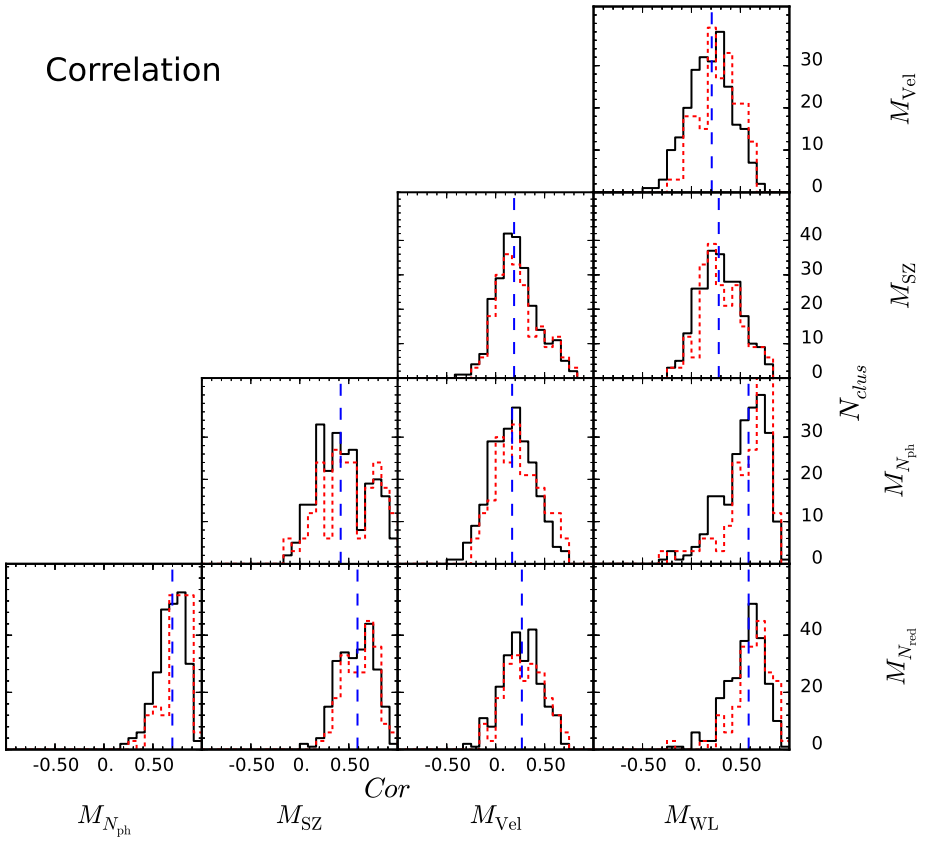

Figure 4.4: Correlations of $M_{\rm est}/M_{\rm true} - 1$ for pairs of mass measurement methods ($M_{N_{\rm red}}$, $M_{N_{\rm ph}}$, $M_{\rm SZ}$, $M_{\rm Vel}$, $M_{\rm WL}$).
The solid line is the distribution of cluster mass scatter correlations, for all clusters individually, for the same pairs as in Fig. 4.3. The dotted line corresponds to the 70 clusters with mass $\geq 2 \times 10^{14} h^{-1} M_{\odot}$. The vertical dashed lines are at the median values which are listed in Table 4.1, along with the average values. Note that the x-axis, the range of correlations, has a scale which varies widely between different types of measurement method pairs.

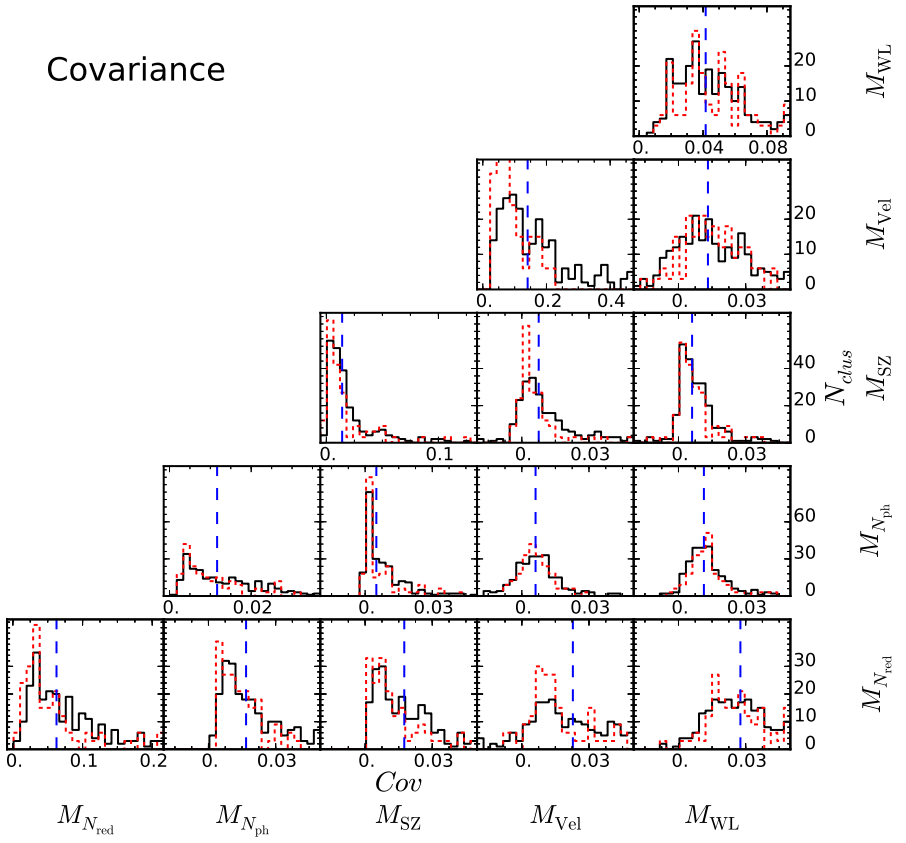

Figure 4.5: Covariances of $M_{\rm est}/M_{\rm true} - 1$ for pairs of mass measurement methods $(M_{N_{\rm red}}, M_{N_{\rm ph}}, M_{\rm SZ}, M_{\rm Vel}, M_{\rm WL})$.
The solid line shows the distribution of cluster mass scatter covariances, for all clusters individually, and the same mass observation pairs as in Figs. 4.3,4.4. The dotted line restricts to the 70 clusters with mass $\geq 2 \times 10^{14} h^{-1} M_{\odot}$. As the characteristic mass scatter for most clusters is about 0.3, the range for covariances shown is ± 0.05. The vertical dashed lines are at the median values, which are also listed in Table 4.1. Note that the x-axis, the range of covariances, has a scale which varies with types of mass measurement method pairs.

Pair	Ave Cor	Med Cor	Ave Cov	Med Cov
$M_{N_{\rm red}} - M_{N_{\rm ph}}$	0.68	0.70	0.025	0.017
$M_{N_{\rm red}} - M_{\rm SZ}$	0.58	0.59	0.037	0.017
$M_{N_{\rm red}} - M_{\rm Vel}$	0.26	0.27	0.031	0.023
$M_{N_{\rm red}} - M_{\rm WL}$	0.55	0.58	0.031	0.028
$M_{N_{\rm ph}} - M_{\rm SZ}$	0.44	0.42	0.012	0.005
$M_{N_{\rm ph}} - M_{\rm Vel}$	0.17	0.17	0.007	0.006
$M_{N_{\rm ph}} - M_{\rm WL}$	0.53	0.58	0.013	0.011
$M_{\rm SZ} - M_{\rm Vel}$	0.22	0.19	0.018	0.008
$M_{\rm SZ} - M_{\rm WL}$	0.29	0.28	0.008	0.006
$M_{\rm Vel} - M_{\rm WL}$	0.19	0.21	0.016	0.013
$M_{N_{\rm red}} - M_{N_{\rm red}}$	–	–	0.084	0.062
$M_{N_{\rm ph}} - M_{N_{\rm ph}}$	–	–	0.015	0.012
$M_{\rm SZ} - M_{\rm SZ}$	–	–	0.070	0.014
$M_{\rm Vel} - M_{\rm Vel}$	–	–	0.205	0.142
$M_{\rm WL} - M_{\rm WL}$	–	–	0.045	0.041

Table 4.1: Average and median values for the distribution (for 243 clusters) of pairs of mass measurement method correlations shown in Fig. 4.4 and covariances shown Fig. 4.5.

sizes should be compared to ∼0.09. The largest covariances are between ($M_{N_{\rm red}}$, $M_{\rm WL}$ and $M_{\rm Vel}$). Each cluster has at least one covariance ≥ 0.01. In contrast, the minimum covariance between measurement methods tends to be between the pair ($M_{N_{\rm ph}}$, $M_{\rm SZ}$).[15]

Some of these correlation and covariance trends are understandable (larger covariances tend to go with quantities with larger scatter more generally and vice versa), but others rely upon the interplay between different measurement methods and the causes of the scatter. The relative importance of different contributions to these were not a priori obvious to us, although reasons could be found for trends. For instance, the two richnesses often are the most correlated mass measurement pair. This is perhaps because both use the same objects (galaxy counts), so that an enhancement or decrement of $M_{N_{\rm ph}}$ (galaxies making the spectroscopic cut) might be more likely accompanied by a similar change in $M_{N_{\rm red}}$ (galaxies making the red sequence cut), than by changes in the mass measurements by other methods. Other mass measurement methods are correlated with richness less directly (for $M_{\rm SZ}$ and $M_{\rm WL}$ the measurements and thus presumably the scatter are more directly tied to the dark matter distribution rather than the biased galaxies, $M_{\rm Vel}$ just seems to be weakly correlated with most things). In section §4.3.3 we compare the PCA results (scatters which occur

[15] If the abovementioned neglected weak lensing and SZ scatter is uncorrelated with local properties of the cluster, as expected, when this scatter is included the majority of the covariances will not change (except possibly the one between weak lensing and SZ, as they can possibly have correlated changes in their scatter due to structure outside the box). However, the correlations will change as they are divided by the correlations of SZ with itself or weak lensing with itself.

together) with physical cluster directions to get some idea of which properties might be driving covariant mass measurement method scatters.

4.3.2 PCA for individual clusters

We now apply PCA to the covariances for $\boldsymbol{M}_{\rm obs}/M_{\rm true}$ for each individual cluster, to get a new basis,

$$\frac{\boldsymbol{M}_{\rm obs}}{M_{\rm true}} = \frac{\boldsymbol{M}^{\alpha}_{\rm est}}{M_{\rm true}} - \frac{\boldsymbol{M}_{\rm ave}}{M_{\rm true}} = \sum_i a_i^{\alpha} \hat{PC}_{i,M} \ . \tag{4.3}$$

The subtracted offset $\boldsymbol{M}_{\rm ave} \equiv \langle \boldsymbol{M}_{\rm est} \rangle$, where the average is over all the lines of sight for each cluster of interest, i.e., there is a different $\boldsymbol{M}_{\rm ave}$ for each cluster. The median (and rms around zero) values for the ensemble of clusters, for $|\boldsymbol{M}_{\rm ave}/M_{\rm true}-1|$ are (0.21 (0.32), 0.11 (0.17), 0.08 (0.15), 0.11 (0.18), 0.18 (0.27)) for $M_{N_{\rm red}}, M_{N_{\rm ph}}, M_{\rm SZ}, M_{\rm Vel}, M_{\rm WL}$ respectively. The relative sizes of the line of sight scatters around the average mass, $\boldsymbol{M}_{\rm obs}/M_{\rm true}-\boldsymbol{M}_{\rm ave}/M_{\rm true}$ compared to the line of sight averaged mass around the true mass $\boldsymbol{M}_{\rm ave}/M_{\rm true}-1$ varies widely cluster to cluster. Except for velocity dispersions, the rms scatters of $(\boldsymbol{M}_{\rm obs}/M_{\rm true} - \boldsymbol{M}_{\rm ave}/M_{\rm true})$ is $\geq |\boldsymbol{M}_{\rm ave}/M_{\rm true}-1|$ for 0.5-0.6 of the clusters and the median value of $|\boldsymbol{M}_{\rm obs}/M_{\rm true}-\boldsymbol{M}_{\rm ave}/M_{\rm true}|$ is $\geq |\boldsymbol{M}_{\rm ave}/M_{\rm true} - 1|$ for about 30-40 percent of the clusters, for velocity dispersions the numbers are closer to 90 and 70 percent respectively.

As in section §4.2.4, and by the definition in Eq. 4.3, $M_{\rm obs}$ refers to mass measurements which have zero average when summed over the sample of interest. Any vector in this space can of course be written in terms of the orthonormal basis $\hat{PC}_{i,M}$, what is special for $\boldsymbol{M}_{\rm obs}$ is that the variances of the a_i^{α} are equal to λ_i for gaussian scatter. Because there are five mass scatters, there are five PCA vectors $\hat{PC}_{i,M}$ per cluster, with eigenvalues $\lambda_{i,M}$, again ordered $\lambda_{0,M} > \lambda_{1,M} > \lambda_{2,M}$ and so on. We use the subscript M to distinguish these PCA vectors from others which will be considered in section 4.5, and take $M_{{\rm obs},i}$, with $i = 0, 1, 2, 3, 4$, to correspond to $(M_{N_{\rm red}}, M_{N_{\rm ph}}, M_{\rm SZ}, M_{\rm Vel}, M_{\rm WL})$ and similarly for $\hat{e}_{{\rm obs},i}$. We also have, as in Eq. 4.1,

$$\hat{PC}_{i,M} = \sum_{{\rm obs},j=0}^{4} \beta_{{\rm obs},j,i} \hat{e}_{{\rm obs},j} \ . \tag{4.4}$$

We first consider the PCA eigenvalues, the $\lambda_{i,M}$. There are some trends: the fractional scatter in the largest direction $(\frac{\lambda_{0,M}}{\sum \lambda}) \sim 0.7$, but can vary from 0.4 to ~ 1, as shown in Fig. 4.6. The relatively large contribution from $\lambda_{0,M}$ means that the variance is strongly dominated by the single combination of mass scatters in the direction of $\hat{PC}_{0,M}$. As seen in Fig. 4.6, bottom, $\lambda_{0,M}, \lambda_{1,M}, \lambda_{2,M}$ together comprise almost all the variance for most clusters. The presence of some mass measurement methods with small scatter suggests that there are some directions of the combined measurement methods which would also have small scatter and thus small $\lambda_{i,M}$, and this is seen in the much smaller values of $\lambda_{4,M}$ and sometimes $\lambda_{3,M}$. The distribution of covariance matrices shown in Fig. 4.5 determine the $\lambda_{i,M}$ when combined

with the relation of the covariances to each other, cluster by cluster. The combination of measurement methods in $\hat{PC}_{4,M}$ which has the smallest variance, $\lambda_{4,M}$ in our case, is also interesting, we return to this in §4.5.

The sum and product of the $\lambda_{i,M}$ for all clusters are shown on a logarithmic plot in Fig. 4.7. The sum of scatters can vary by a factor of ~ 30 from cluster to cluster, and tends to be dominated by $\lambda_{0,M}$, while the product of the $\lambda_{i,M}$ can be made very small (its size varies by over 10^7) if some directions, especially $\hat{PC}_{4,M}$, have very little scatter. In §4.4 below, these scalar properties of the cluster mass scatter will be compared to physical cluster properties such as triaxiality and mass.

Turning to the PCA vectors, many clusters have similar $\hat{PC}_{0,M}$ (i.e. the combination of mass scatters that dominates is similar for many of the clusters). To quantify this more generally, we took $\hat{PC}_{i,M,minsq}$ as the direction which minimizes $(\hat{PC}_{i,M}\cdot\hat{PC}_{i,M,minsq})^2$ for the full ensemble of 243 clusters ($\hat{PC}_{0,M,minsq}$ is shown in the first line of Table 4.2). Fewer than 20 percent of the clusters have their $\hat{PC}_{0,M}$ pointing more than 45° away from $\hat{PC}_{0,M,minsq}$; about 25 percent have their $\hat{PC}_{1,M}$ pointing more than 45° away from $\hat{PC}_{1,M,minsq}$. We found that for almost all the clusters the projection upon $\hat{PC}_{1,M,minsq}$ is close in size to the projection on $\hat{PC}_{0,M,minsq}$, (i.e. 0.62 correlation). Continuing to $\hat{PC}_{4,M}$, the direction of least scatter, ~ 0.7 of the clusters are within 45° of $\hat{PC}_{4,M,minsq}$ given in Table 4.2. This minimum scatter direction is (not surprisingly) dominated by the $\hat{e}_{\rm N_{ph}}, \hat{e}_{\rm SZ}$ directions, since these are the mass measurement methods with the smallest scatter in our sample.[16] The similar forms of the $\hat{PC}_i$ suggest that the mass scatter combinations they correspond to might have similar physical origins. For 75 percent of the clusters, the coefficients of $\hat{PC}_{0,M}$ are also all the same sign, that is that the dominant combination of scatter also has all the scatters increasing together relative to their average values, but 16/243 have large (< -0.1) opposite sign coefficients for some mass measurement methods. As a large fraction of the variance is captured by $\hat{PC}_{0,M}$, as seen in the large values of $\lambda_{0,M}/\sum\lambda$, the coefficient of $\hat{PC}_{0,M}$ for the any given line of sight is indicative of the size of scatter from the average along that line of sight.

The correlations of the five mass measurement methods $M_{{\rm obs},i}$ with the $\hat{PC}_j$ coefficients a_j^α, for all clusters, are shown in Fig. 4.8. For the ensemble of cluster measurements, the largest correlation with a_0^α, i.e. with the coefficient of $\hat{PC}_{0,M}$, is for velocity dispersions (in part because most of the scatter is due to velocity dispersions). Correlations of a_0^α with the other mass measurement methods are relatively smaller, and of similar size to each other. Taking instead the fraction of the mass scatter vector due to $\hat{PC}_0$, i.e., $a_0^\alpha/\sqrt{\sum_i (a_i^\alpha)^2}$, the correlations are weaker. In addition, weaker correlations arise with the coefficients of $\hat{PC}_{1,M}$, and for the direction with the smallest direction of scatter, $\hat{PC}_{4,M}$, only $M_{N_{\rm ph}}$ has a noticeable correlation on average.

The direction of $\hat{PC}_{0,M}$ can also be compared to that of $\boldsymbol{M}_{\rm ave}/M_{\rm true}$: the average inner

[16] Again recall these particular coefficients do not carry over directly to observations, most importantly because they are based on scatter in $P(M_{\rm est}|M_{\rm true})$ and not vice versa.

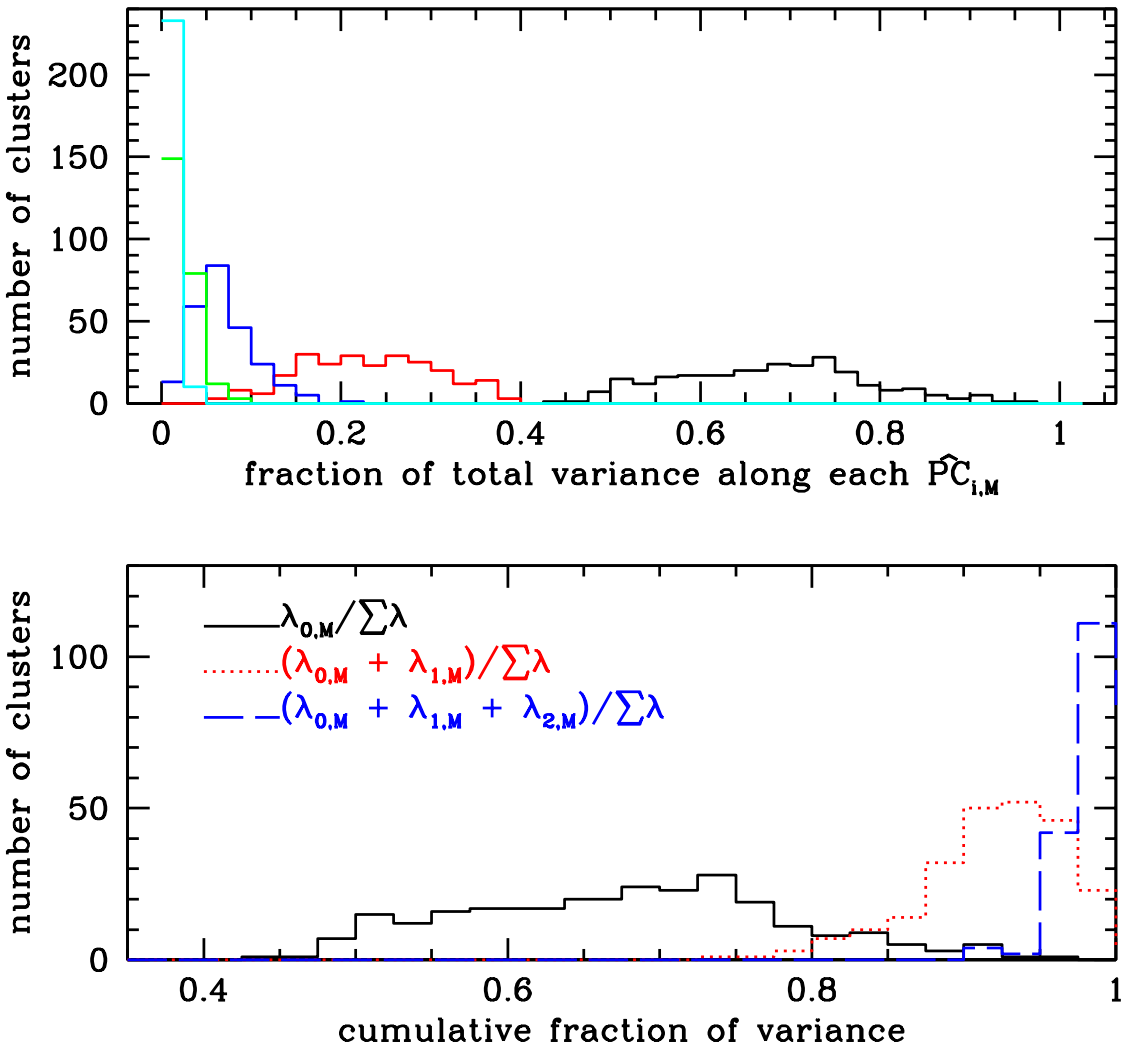

Figure 4.6: (Top) Peaks from right to left: fraction of covariance (i.e. scatter) $\frac{\lambda_{0,M}}{\sum\lambda}$, $\frac{\lambda_{1,M}}{\sum\lambda}$, $\frac{\lambda_{2,M}}{\sum\lambda}$, etc. On average $\frac{\lambda_{0,M}}{\sum\lambda} \sim 0.7$. (Bottom) Peaks from left to right: fraction of covariance from scatter in direction of $\hat{PC}_{0,M}, \hat{PC}_{0,M}$or $\hat{PC}_{1,M}$, etc. Most of the scatter is in the directions spanned by $\hat{PC}_{0,M}, \hat{PC}_{1,M}, \hat{PC}_{2,M}$, with a substantial fraction in the direction of the largest scatter.

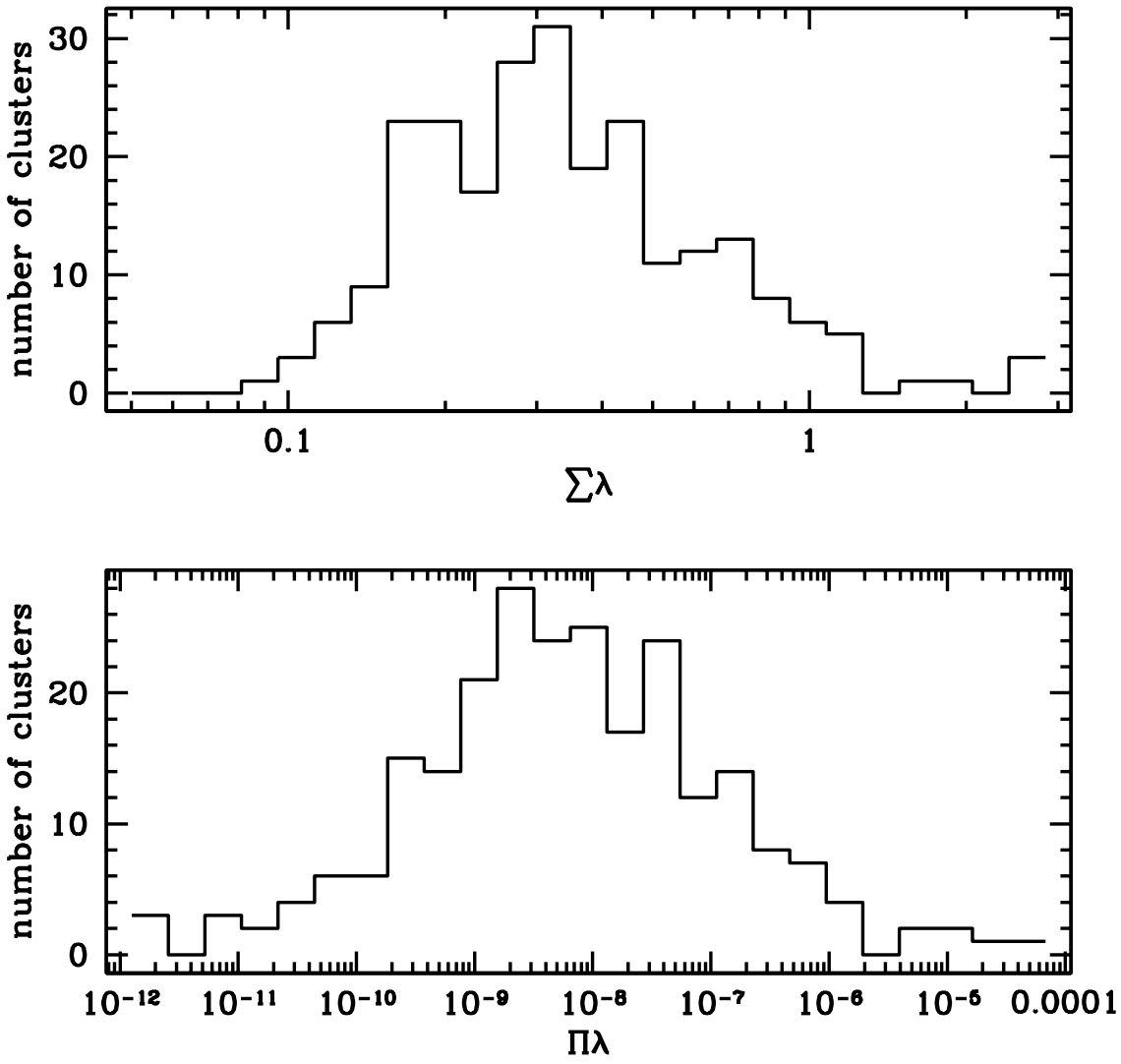

Figure 4.7: Distributions of sum and product of covariances for all clusters: the sum is dominated by the eigenvalue in the direction of largest scatter, $\lambda_{0,M}$, while the product, related to the volume in the space of scatters, can be made very small by small values of e.g. $\lambda_{4,M}$. The sum of eigenvalues peaks at ~ 0.3, the product peaks around 10^{-8}.

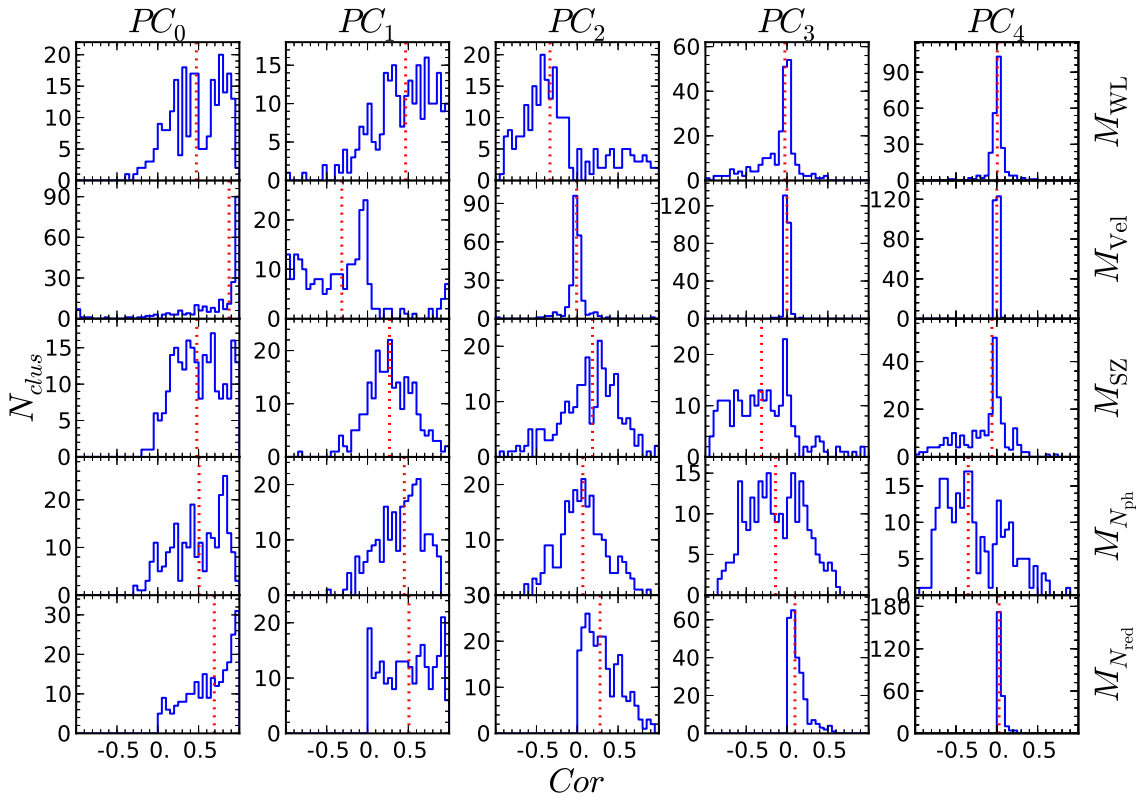

Figure 4.8: The correlations between the observed mass scatters and their projected values on $\hat{PC}_{i,M}$. Velocity dispersions are very strongly correlated with the direction of the largest scatter, $\hat{PC}_{0,M}$ in part because the component of $\hat{PC}_{0,M}$ in the velocity dispersion direction, $\beta_{vel,\,0}$, tends to be large. The dotted line marks the median value of the correlations. Note that the y-axis scale varies with mass measurement method and $\hat{PC}_i$, the x-axis does not.

direction	$\hat{e}_{\rm N_{red}}$	$\hat{e}_{\rm N_{ph}}$	$\hat{e}_{\rm SZ}$	$\hat{e}_{\rm vel}$	$\hat{e}_{\rm WL}$
$\hat{PC}_0$					
$\hat{PC}_{0,M,minsq}$	0.42	0.14	0.19	0.83	0.29
$\hat{PC}_{0,M,total}$	0.52	0.21	0.31	0.69	0.34
$\hat{PC}_{0,M,total,massive}$	0.54	0.25	0.38	0.51	0.49
$\hat{PC}_4$					
$\hat{PC}_{4,M,minsq}$	0.15	-0.96	0.2	-0.01	0.15
$\hat{PC}_{4,M,total}$	0.32	-0.94	-0.02	0.006	0.098
$\hat{PC}_{4,M,total,massive}$	0.34	-0.94	0.03	0.02	0.06

Table 4.2: Different characteristic directions in the space of mass scatters, ($\hat{e}_{\rm N_{red}}$, $\hat{e}_{\rm N_{ph}}$, $\hat{e}_{\rm SZ}$, $\hat{e}_{\rm vel}$, $\hat{e}_{\rm WL}$) defined in this section and sections below, listed together for comparison. The direction which minimizes the dot product squared with $\hat{PC}_{i,M}$ of all 243 clusters is $\hat{PC}_{i,M,minsq}$. $\hat{PC}_{i,M,total}$ are the vectors found by PCA analysis of all observed cluster masses (normalized by $M_{\rm true}$) and all lines of sight, jointly, discussed in §4.5, $\hat{PC}_{i,M,total,massive}$ restricts to the 70 clusters with $M \geq 2\times10^{14}h^{-1}M_\odot$. These vectors are derived from our estimates of $M_{\rm est}(M_{\rm true})$, which as mentioned earlier, neglects some systematics for WL and SZ and relies upon our simulation calibrated mass definitions in terms of observables.

product ~ 0.7, but the peak is closer to 0.8, and there is a broad range of values. (The rest of the vector $\frac{\boldsymbol{M}_{\rm ave}}{M_{\rm true}}$ seems to lie in the $\hat{PC}_{1,M}, \hat{PC}_{2,M}$ plane). That is, the direction of largest mass measured is close to that of largest scatter; presumably this is because this direction has large scatters generally.

We now compare the above quantities to line of sight dependent cluster properties. We will follow this in section §4.4 with properties depending on the entire cluster rather than a given line of sight.

4.3.3 Relation to cluster line of sight properties

To get more understanding of the PCA decomposition, we compare values of PCA quantities along lines of sight to cluster properties along those lines of sight. The PCA line of sight dependent properties we consider are the coefficients a_i^α of the $\hat{PC}_{i,M}$, $a_i^\alpha/\sqrt{\sum_j (a_j^\alpha)^2}$ (the fraction of scatter in different $\hat{PC}_i$ directions, i and j each run from 0 to 4), and the total scatter for a given line of sight ($\sum_i (a_i^\alpha)^2/\lambda_{i,M}$). We correlate these with the angle $\theta_{\rm obs}$ between the line of sight and six specific physical cluster directions, listed below.

Previously, for this simulated data set, increased mass scatter was found by observing along certain physical cluster directions by WCS; Noh & Cohn (2011); Cohn (2012). Our extension using PCA includes six physical directions: the long axis $\hat{\ell}$ of the cluster, calculated using the dark matter particles in the simulation with a FoF finder as mentioned above, the plane normal containing the most halo mass $\hat{n}_{\rm mass}$, or connected filament mass $\hat{n}_{\rm fil}$ centered

	$\hat{PC}_{0,M}$	$\hat{PC}_{1,M}$	$\hat{PC}_{2,M}$	$\hat{PC}_{3,M}$	$\hat{PC}_{4,M}$
$\hat{r}_{sub}$	0.35(0.31)	0.18(0.19)	0.01(0.02)	0.02(0.03)	0.03(0.04)
$\hat{v}_{sub}$	0.21(0.22)	0.08(0.10)	0.00(0.01)	0.02(0.02)	0.01(0.01)
$\hat{r}_{fil}$	0.28(0.24)	0.16(0.15)	0.03(0.04)	0.00(0.01)	0.00(0.00)
$\hat{n}_{fil}$	-0.37(-0.29)	-0.22(-0.21)	-0.08(-0.08)	-0.06(-0.04)	0.01(0.02)
$\hat{n}_{mass}$	-0.38(-0.32)	-0.24(-0.21)	-0.07(-0.07)	-0.04(-0.04)	0.03(0.02)
$\hat{l}_1$	0.56(0.50)	0.34(0.33)	-0.01(0.02)	0.04(0.06)	0.05(0.05)

Table 4.3: The median of correlation coefficients between the fraction of the line of sight mass scatter covariance in each $\hat{PC}_{i,M}$ direction and $|\cos\theta_{obs}|$. The average is shown in the parenthesis. The full distribution is shown in Fig. 4.9.

on the cluster (see §4.2.3 and Noh & Cohn (2011) for more details), the direction of the largest subgroup of galaxies $\hat{r}_{\rm sub}$ which originated from the same infall host halo (see §4.2.3), and the velocity direction $\hat{v}_{\rm sub}$ of this largest subgroup.[17] Many of these special cluster directions are similar to each other, e.g. Kasun & Evrard (2005); White et al. (2010); Cohn (2012), as expected.

The correlation of $a_i^\alpha/\sqrt{\sum_j (a_j^\alpha)^2}$ (the fraction of the mass scatter in the $\hat{PC}_{i,M}$ direction, for the line of sight indexed by α) with $|\cos\theta_{obs}|$ for each observation is shown in Fig. 4.9. The largest average correlations of angles with the physical cluster axes are with $\hat{PC}_{0,M}$, the direction of the combination of mass scatters that dominates the scatter. The average correlations with $\hat{PC}_{1,M}$ are slightly smaller, for the rest of the $\hat{PC}_{i,M}$ the average correlations tend to zero (as can be seen, the individual clusters can have larger correlations). For $\hat{PC}_{0,M}$, the largest correlation is with the direction of the cluster long axis $\hat{\ell}$. The next largest signals are with the direction of the mass plane normal $\hat{n}_{\rm mass}$, and filament plane normal $\hat{n}_{\rm fil}$, and the direction of the largest substructure $\hat{r}_{\rm sub}$. The velocity of the largest substructure $\hat{v}_{\rm sub}$ and the direction of the most massive filament $\hat{r}_{\rm fil}$ are more weakly correlated. That is, scatter dominated by the mass scatter combination in $\hat{PC}_{0,M}$ tends to occur more often when the direction of observation is more aligned with the long axis of the cluster. (As the other cluster directions are not linearly independent, strong correlations with them are possible and seen as well.) As most of the scatter occurs along $\hat{PC}_{0,M}$ and $\hat{PC}_{1,M}$, both of which are most correlated with looking along the long axis, it suggests that most of the scatter is due to looking along the long axis $\hat{\ell}$.

The correlation with a_0^α, the full contribution from $\hat{PC}_{0,M}$, rather than the fractional contribution above, was much weaker.

One other line of sight quantity, $\sum_i (a_i^\alpha)^2/\lambda_{i,M}$ (the weighted scatter of $M_{\rm obs}^\alpha$), also tends

[17] We also measured correlations with another direction dependent quantity, the amount of substructure found via the Dressler-Schectman (Dressler & Shectman 1988) test, as described in White et al. (2010); Cohn (2012), however, the correlations with $\hat{PC}_{0,M}$ were much weaker with this directional dependent quantity than with the ones reported here.

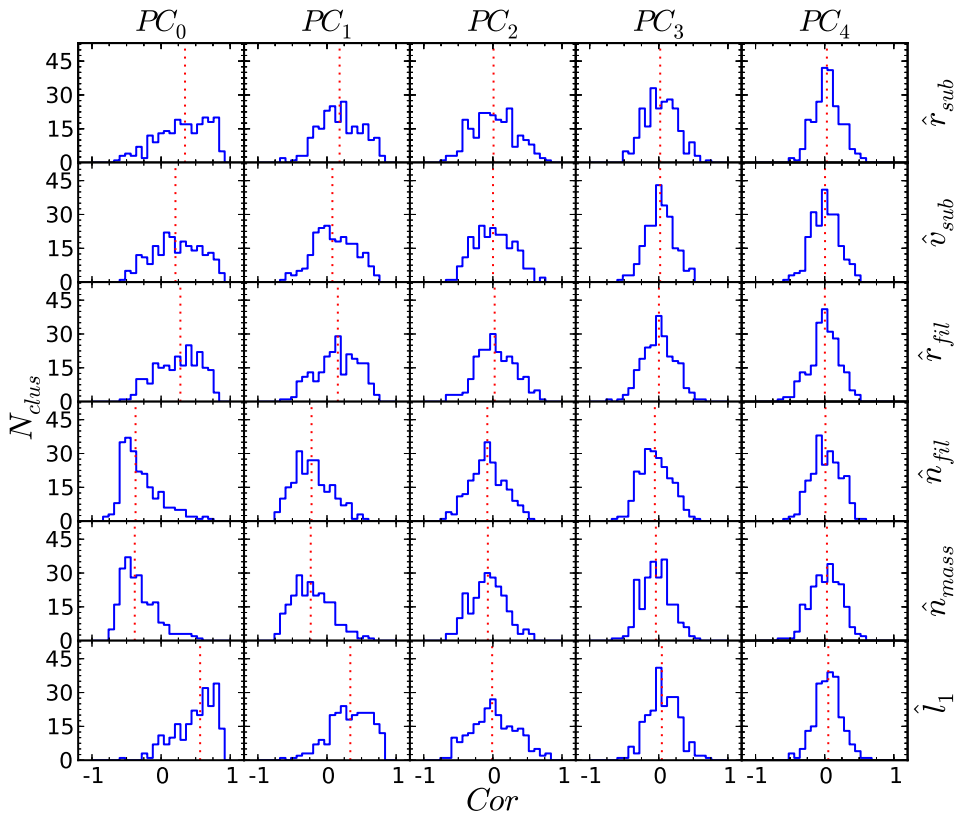

Figure 4.9: Correlations between the fraction of the line of sight mass scatter in the $\hat{PC}_{0,M}$ direction and $|\cos\theta_{obs}|$. The cluster physical directions are $\hat{\ell}$, the long axis of the cluster, $\hat{n}_{\rm mass}$, the direction perpendicular to the mass disk with radius 10 $h^{-1}Mpc$ and width 3 $h^{-1}Mpc$ centered on the cluster, containing the majority of the mass in halos, $\hat{n}_{\rm fil}$, similar to $\hat{n}_{\rm mass}$ in shape and volume, but oriented to contain the majority of the filamentary mass ending on the cluster, $\hat{r}_{\rm fil}$, the direction to the most massive halo filament surrounding the cluster, and $\hat{v}_{\rm sub}, \hat{r}_{\rm sub}$, the relative velocity and direction of the largest galaxy subgroup in the cluster. See text and §4.2.3 for more detailed definitions. Only the 227 clusters which are filament endpoints are included in the comparisons concerning filament planes. Vertical dotted lines denote medians, and the averages and medians are shown in Table 4.3. The largest contributions to $\hat{PC}_0$, for most clusters, seem to come when observing along the long axis of the cluster, but there is a wide scatter. The correlations with the mass and filament planes are maximized for observations along the planes, i.e. perpendicular to the normal vectors $\hat{n}_{\rm mass}, \hat{n}_{\rm fil}$, as expected.

to have correlations with special cluster directions as seen in Fig. 4.10. The largest fraction of clusters with correlations > 0.20 occurs with the long axis.[18]

To summarize this section, each cluster's line of sight mass scatter variations and correlations were analyzed and characterized separately using PCA. Both similarities (similar large scatter directions) and differences (raw size of scatter, amount of variation with line of sight) were found. The scatter was usually dominated (large $\lambda_{0,M}/\sum\lambda$) by one combination of mass scatters, which also tended to become an increasing component of the total mass scatter as the angle of observation became more aligned along the cluster's long axis.

4.4 Cluster to cluster variations

Now we turn to line-of-sight independent properties, PCA related or otherwise. The scatters of each cluster are also characterized by several numbers, i.e. scalars, which are not dependent upon the line of sight of observation (e.g. λ_0). Here we take some characteristic mass scatter scalars for each cluster and compare them with other cluster properties, intrinsic to the cluster or due to its environment, 24 in total. We make use of several quantities obtained previously (WCS; Noh & Cohn (2011); Cohn (2012)) for this simulation and described in §4.2.3. We use correlations rather than covariances, to take out the dimensional dependence. After considering properties of the pairwise correlations in §4.4.2, we consider the full ensemble of correlations using PCA in §4.4.3.

4.4.1 Cluster quantities

For each cluster we consider the following (note that mass scatters are for $\boldsymbol{M}_{\rm obs} = \boldsymbol{M}_{\rm est} - \langle \boldsymbol{M}_{\rm est}\rangle = \boldsymbol{M}_{\rm est} - \boldsymbol{M}_{\rm ave}$):

- $\Delta M_i \equiv (M_{ave,i} - M_{\rm true})/M_{\rm true}$, observed average mass offsets for each of the five observables considered earlier: red galaxy richness, phase richness, SZ, velocity dispersions and weak lensing respectively. Note that these correlations are identical to those of $M_{ave,i}/M_{\rm true}$.

- $|\cos\theta_{0,minsq}|$, i.e. $|\hat{PC}_{0,M}\cdot\hat{PC}_{0,M,minsq}|$, the angle between the largest mass scatter direction for each cluster, $\hat{PC}_{0,M}$, and the direction $\hat{PC}_{0,M,minsq}$, given in Table 4.2,

[18] Correlations with the cluster long axis and external filaments or nearby clusters, both possible causes of mass scatters, have been seen in many other works too, e.g. van de Weygaert & Bertschinger (1996); Splinter et al. (1997); Colberg et al. (1999); Chambers et al. (2000); Onuora & Thomas (2000); Faltenbacher et al. (2002); van de Weygaert (2002); Hopkins et al. (2005); Bailin & Steinmetz (2005); Faltenbacher et al. (2005); Kasun & Evrard (2005); Basilakos et al. (2006); Lee & Evrard (2007); Lee et al. (2008); Paz et al. (2008); Pereira et al. (2008); Ragone-Figueroa & Plionis (2007); Costa-Duarte et al. (2011); Ceccarelli et al. (2011); Paz et al. (2011), correlations with the long axis and mass scatters specifically have been discussed recently in, e.g., Becker & Kravtsov (2011); Marrone et al. (2012); Battaglia et al. (2012); Bahé et al. (2012); Feroz & Hobson (2012).

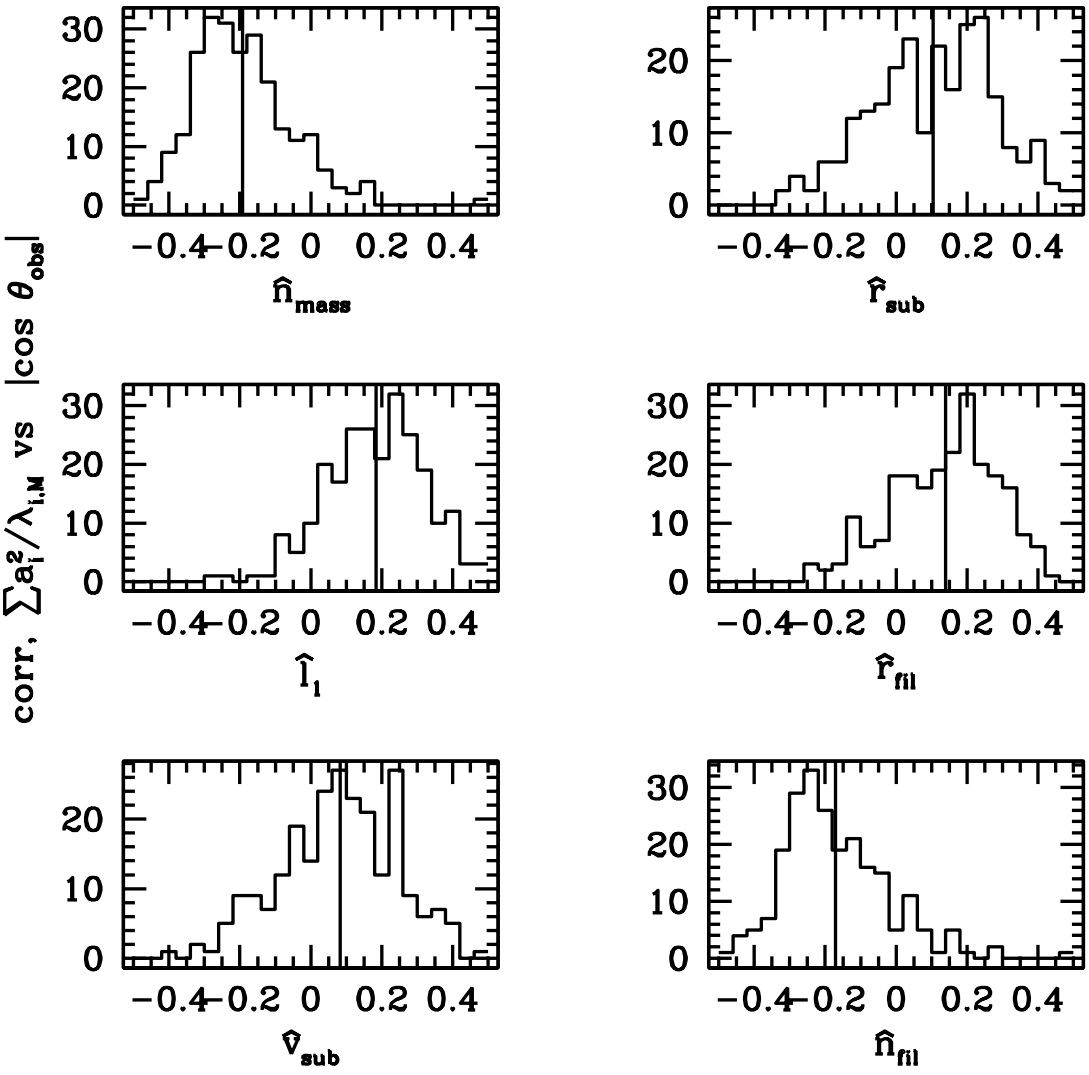

Figure 4.10: Correlations of $\sum_i (a_i^\alpha)^2/\lambda_{i,M}$ (the weighted scatter of $M^\alpha_{\rm obs}$) with angle between line of sight and various cluster axes, as described in the text and in Fig. 4.9. Vertical lines are at average value.

which minimizes the dot product with $\hat{PC}_{0,M}$ for all the clusters.

- $\sum \lambda$, the sum of the cluster's mass scatters in §4.3.2.
- $\prod \lambda$, the product of the cluster's scatters in §4.3.2.
- $\frac{\lambda_{0,M}}{\sum \lambda}$ fraction of total (mass scatter) variance along direction of largest variance in §4.3.2.
- $\lambda_{1,M}$, variance along the direction with second largest mass scatter variance in §4.3.2.
- $\lambda_{4,M}$, variance along the direction with smallest mass scatter variance in §4.3.2.
- $T = \frac{l_1^2 - l_2^2}{l_1^2 - l_3^2}$, triaxiality, where the l's are the axes of cluster, calculated using the dark matter particles in the FoF halo.
- $S = \frac{l_3}{l_1} \quad (l_1 > l_2 > l_3)$, sphericity.
- $f_{M_{\rm fplane}}$, the fractional connected filamentary mass in the local plane around clusters defined in §4.2.3.
- $f_{M_{\rm hplane}}$, the fractional halo mass in the local plane around clusters, see §4.2.3.
- $M_{\rm sphere}$, the mass in halos above $5 \times 10^{13} h^{-1} M_\odot$ within a 10 $h^{-1}Mpc$ radius sphere of the cluster. We used the sum of large halo masses in a 10 $h^{-1}Mpc$ radius sphere around the central cluster rather than the total mass because the former is already known to be correlated with the mass of the central halo (e.g., Noh & Cohn (2011)).
- $M_{\rm true}$, the cluster (FoF $b = 0.168$) mass (also called M).
- $f_{R_{\rm sub}}$, the fractional richness of the largest galaxy subgroup (see §4.2.3).
- $f_{D_{\rm sub}}$, the ratio of the distance to the largest galaxy subgroup in the cluster to the length of the longest cluster axis (see §4.2.3).
- $c_{\rm vir}$, the concentration (not scatter from mean concentration of a given mass), from fitting all of the Friends of Friends halo particles to an NFW (Navarro et al. 1997) profile. This was found to be very important in the previous studies (Jeeson-Daniel et al. 2011; Skibba & Macciò 2011; Einasto et al. 2011) inspiring this work.
- $t_{1:3}$, the time of most recent ≥1:3 merger (often taken as the threshold for a merger-driven starbust)
- $t_{1:10}$, the time of most recent ≥1:10 merger (often taken as a threshold for merger-driven AGN feeding)

- $x_{\rm off}$, the distance between the central galaxy position and the average of the galaxy positions. This is similar to the "relaxedness" considered by Skibba & Macciò (2011), but in that case they use the offset between the most bound particle and the halo center of mass. We also considered scaling by $M^{1/3}$, the results did not change significantly.

- $\cos\theta_{\Delta,0}$, the cosine of the angle between $\hat{PC}_0$ and $\boldsymbol{M}_{\rm ave}$, i.e., the largest mass scatter direction vs. the average mass offset direction.

We thus have a space of dimension $N_{\rm method} = 24$ for the correlation and PCA analysis below. Several of these quantities might be expected to be related. For instance, sphericity and triaxiality both characterize departures from perfect spheres, but triaxiality measures prolateness and oblateness while sphericity is sensitive to flatness. Similarly the sum and product of the eigenvalues probe the size of the largest eigenvalue and in principle how the largest and smallest eigenvalue change together, respectively. A priori, it isn't clear which of our large set of quantities have the strongest or most illuminating relations to each other, so we start with a large set.

4.4.2 Correlations

Fig. 4.11 summarizes the pairwise correlations. For simplicity, only correlations which have absolute value > 0.2, in six ranges, $\pm 0.2, 0.35, 0.5$, are shown. The correlations of measurements with themselves are omitted. Filled dark (open red) symbols are positive (negative) correlations. Properties in the list are grouped by type: offsets of cluster average mass measurements from their true mass ("ΔM", defined in §4.4.1), PCA related scalars for each cluster from §4.3.2 ("λ_M"), cluster environment or shape ("phys1"), cluster history ("phys2"), and $|\cos\theta_{\Delta,0}|$. Relations between measurements of the same sort (e.g. concentration and time of last merger, etc.) can be seen in the diagonal boxes.

The off-diagonal boxes thus correlate different sorts of cluster properties. We concentrate on these. The first thing to notice is that many large correlations are visible. We start with correlations with $\Delta\boldsymbol{M}$, each cluster's five average fractional mass measurement offsets, corresponding to the five measurement methods. The different components of $\Delta\boldsymbol{M}$ often have similar correlations with other quantities. In particular, they are all strongly correlated with sphericity, most are anticorrelated with triaxiality and all are anticorrelated with the offset of the average galaxy position. All but the weak lensing mass offset are also correlated with the smallest mass variance $\lambda_{4,M}$, that is, when the average mass offsets ΔM_i are large, the variance in the direction of minimum scatter around the average measured value tends to be large as well: the line of sight averaged scatter often is increasing for clusters with larger mass scatters around these averages. There is also a trend of these average mass offsets being anticorrelated with signatures of relaxedness (fractional richness of the largest subgroup, offset of the average galaxy position relative to the galaxy center, etc.).

Turning to other correlations with the mass scatter variances, an increase in the mass in halos around the cluster tends to be accompanied by an increase many of the measures of

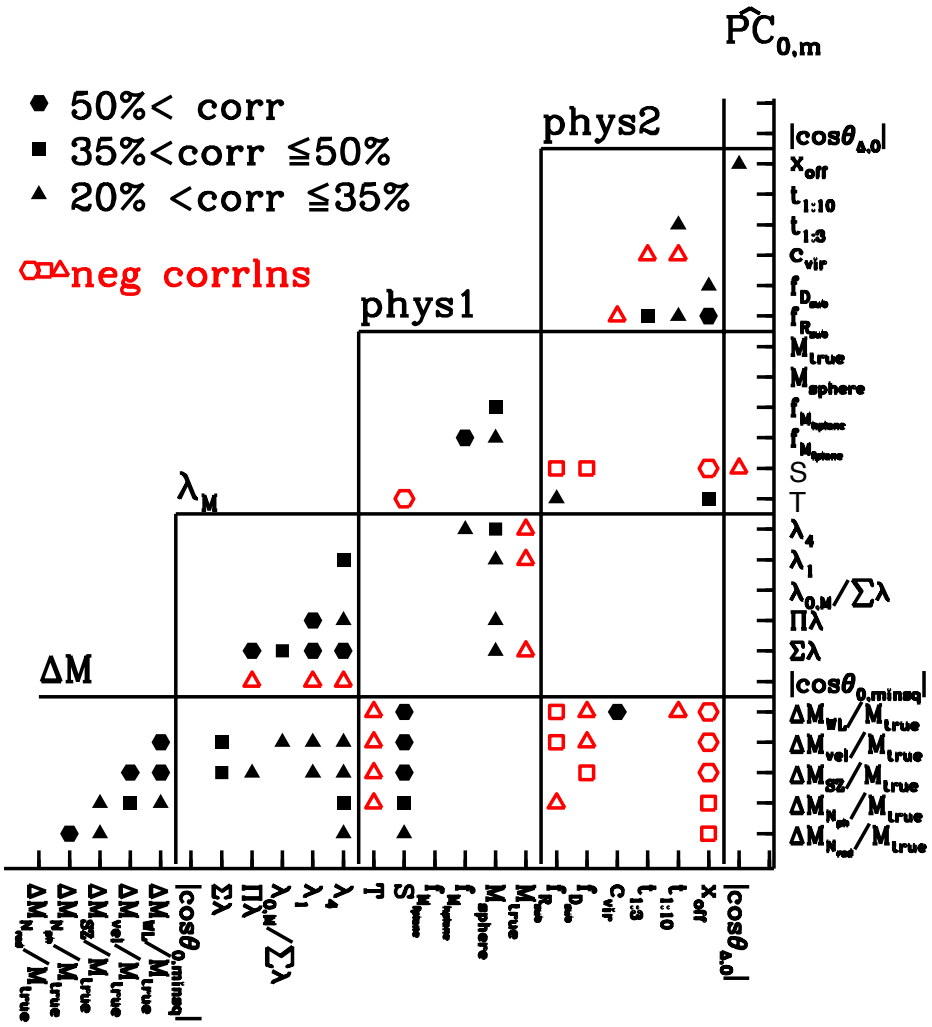

Figure 4.11: Correlations between cluster properties: $0.5 < corr$ (filled hexagons), $0.35 < corr \leq 0.5$ (filled squares), $0.2 < corr \leq 0.35$(filled triangles), opposite signs are open versions of the same symbols, i.e. $corr < -0.5$ (open hexagon), etc. Auto-correlations are not shown. Cluster properties are described in section 4.4.1. A blank space means that a correlation has absolute value ≤ 0.2. The horizontal and vertical lines distinguish the types of cluster properties. ΔM labels the five components of $\Delta \boldsymbol{M}$. λ_M refers to measurements for that cluster's mass scatter correlations. "phys1" refers to cluster properties which are environmental or shape related. "phys2" refers to cluster properties more related to substructure or merging (concentration, distance to largest substructure, etc.), λ_0 refers to dot product or correlation with $\hat{PC}_{0,M}$. Only half of the correlations are shown, as they are symmetric across the diagonal axis.

mass scatter, i.e. properties associated with the $\lambda_{i,M}$. This might indicate the presence of a supercluster. The size of the smallest mass scatter variance $\lambda_{4,M}$ also seems to increase with increasing fractional halo mass in the plane of the cluster, $f_{M_{hplane}}$.

Lastly, triaxiality is correlated with indicators of substructure, (the offset of the galaxy average position from the central galaxy and the fractional richness of the largest galaxy subgroup), while in contrast sphericity is anticorrelated with these, as well with the fractional distance of the largest galaxy subgroup from the cluster center. Physically, one might expect a rich subgroup in the cluster to lie along the long axis of the cluster (e.g. coming from a filament feeding matter into the cluster) and be correlated with a lengthed (more triaxial) cluster as a result.

4.4.3 PCA

By using PCA on these pairwise correlations, more general groupings can be investigated. This application of PCA to our sample is an extension of PCA analysis of several cluster properties studied by Jeeson-Daniel et al. (2011); Skibba & Macciò (2011) and by Einasto et al. (2011) for superclusters, which inspired this study. Properties correlated by Jeeson-Daniel et al. (2011); Skibba & Macciò (2011) included virial mass, concentration, age, relaxedness, sphericity, triaxiality, substructure, spin, "relaxedness" and environment. Jeeson-Daniel et al. (2011) used 1867 halos from several boxes with masses ranging from $\sim 10^{11}h^{-1}M_{\odot}$ up and found that the dominant PC vector was most correlated with halo concentration. Skibba & Macciò (2011) used several boxes with halos with masses $\geq 10^{10}h^{-1}M_{\odot}$, and also found halo concentration to be important, as well as halo mass and degree of relaxedness, for clusters.[19] Our sample is closest to the high mass tail of these samples.

The 24 PCA eigenvalues[20] are $\lambda_i/\sum\lambda$=(0.22, 0.12, 0.09, 0.08, 0.07, 0.05 (3 times), 0.04, 0.03 (4 times), 0.02 (3 times), 0.01 (6 times), < 0.005 (2 times)). Unlike the case of mass scatter, where $\lambda_{0,M}$ is relatively large, (on average $\lambda_{1,M}/\lambda_{0,M} < 0.4$), here $\lambda_1/\lambda_0 \sim 0.6$, and $(\lambda_1, \lambda_2, \lambda_3, \lambda_4) = (5.23, 3.00, 2.07, 1.95)$, fairly close to each other. This makes interpretation less straightforward. However, subsets of properties with strong correlations with individual $\hat{PC}_i$ may indicate these properties change together. To better identify relations, one can take these subsets and do PCA on the correlations within this subset alone. An example is given below. The expansion coefficients of the $\hat{PC}_i$ for the different measured quantities, the β_i in Eq. 4.1, are given by the correlations divided by the eigenvalues. (For example, the expansion coefficients of the $\hat{PC}_0$ in the order listed in §4.4.1 are (0.19, 0.26, 0.34, 0.35,

[19]For superclusters in SDSS DR7, Einasto et al. (2011) considered weighted luminosity, volume, diameter, density of the highest density peak of galaxies and the number of galaxies, as well as shape parameters, and used the two largest $\hat{PC}_i$ to find scaling relations. They divided up the sample into two sets of superclusters based upon where they lay in the planes spanned by pairs of $\hat{PC}_0, \hat{PC}_1, \hat{PC}_2$.

[20]Some of the previous analyses consider logarithms of the scalar quantities, we redid the analysis taking logarithms of $\sum\lambda$, $\prod\lambda$, $\lambda_{1,M}$, $\lambda_{4,M}$, $f_{M_{\rm fplane}}$, $f_{M_{hplane}}$, $f_{R\rm sub}$, $f_{D_{\rm sub}}$, c, $M_{\rm sphere}$, M and found very similar results for correlations with the first 2 $\hat{PC}_i$ as below, for $\hat{PC}_2$, correlations roughly increased for the merger related quantities, and decreased for the $M_{\rm sphere}$ and plane environment quantities.

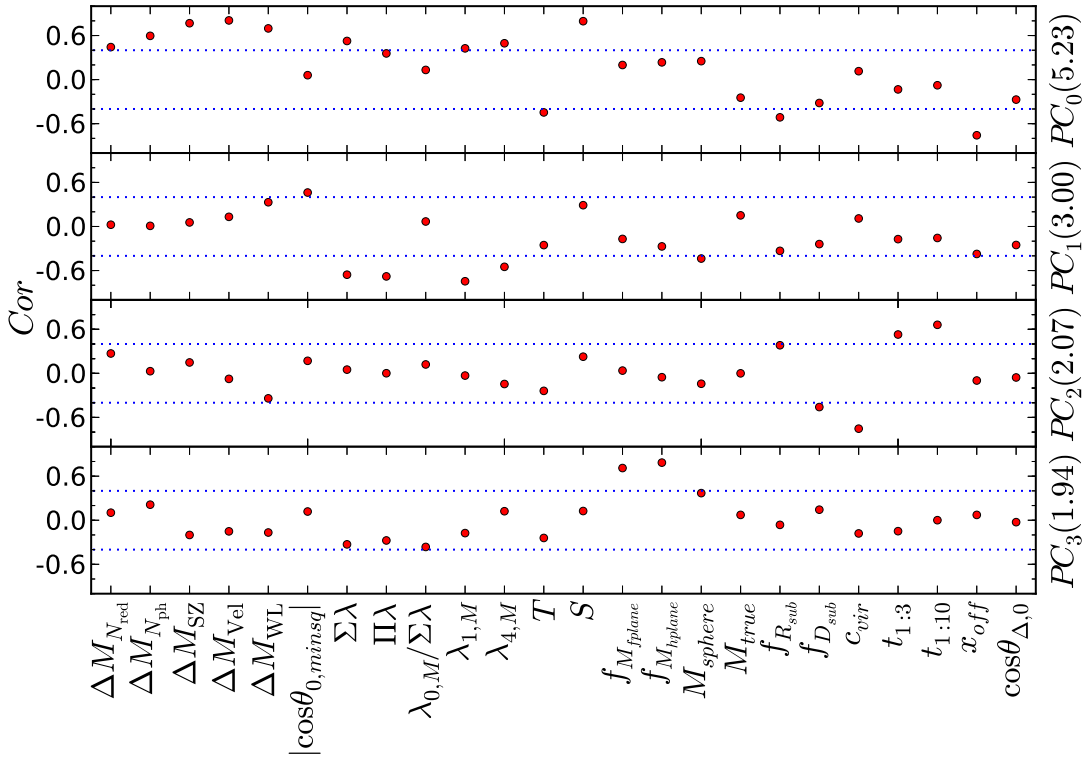

Figure 4.12: Correlation coefficients between the cluster properties listed in §4.4.1 and their projection on the first four principal components. Horizontal dotted lines at ±0.4 are to guide the eye to larger positive or negative correlations. The top box is for $\hat{PC}_0$, the second is for $\hat{PC}_1$ and so on; the expansion of the $\hat{PC}_i$ vectors is given by these correlations divided by the λ_i eigenvalues, 5.23, 3.0, 2.07, 1.94 respectively for $\hat{PC}_0, \hat{PC}_1, \hat{PC}_2, \hat{PC}_3$.

0.30, 0.03, 0.23, 0.16, 0.06, 0.19, 0.22, -0.20, 0.35, 0.09, 0.10, 0.11, -0.11, -0.22, -0.14, 0.05, -0.06, -0.03, -0.33, -0.12).)

The strongest correlation is between the velocity dispersion mass offset $\Delta M_{\rm Vel}$ and $\hat{PC}_0$ ($\sim$0.8), 9 other properties have correlations with absolute value above or equal to 0.7 with at least one of the $\hat{PC}_i$ ($i \leq 6$). Considering smaller correlations, 21/24 of the properties have at least one correlation of absolute value ≥ 0.5 with one of the $\hat{PC}_i$, $i \leq 11$, and all properties have at least one correlation ≥ 0.4 with at least one $\hat{PC}_i$. The correlations of the first four principal component vectors with the 24 properties are shown in Fig. 4.12. Lines are drawn at $\pm$0.4 to guide the eye to the larger correlations. The sign of the correlations with the eigenvectors depends upon the overall sign of the eigenvectors, which is arbitrary, but the relative signs of the correlations of the different properties with each eigenvector are not arbitrary.

We begin with $\hat{PC}_0$, the direction of largest variation. The ΔM_i's, the sum of the mass scatter variances $\sum\lambda$, the individual mass scatter variances $\lambda_{1,M}, \lambda_{4,M}$ and sphericity S all have large correlations (≥ 0.4) with their projections onto $\hat{PC}_0$. These correlations are in the opposite sense of those of T, $f_{R_{sub}}$ and x_{off} (these latter three might indicate less relaxed halos). A relation between large triaxiality and an increased offset in the average galaxy position or the presence a rich subgroup is somewhat intuitive, but the sign of the relation to the average mass measured for the cluster is surprising. One interpretation of the relation between ΔM_i and T seen both here and in the correlations is that clusters which are more triaxial have fewer lines of sight along the elongated and presumably large measured mass direction, so that fewer lines of sight result in a large $\boldsymbol{M}_{\rm est}/M_{\rm true} - 1$. See also related discussion in Rasia et al. (2012).[21]

To go further, we considered the subset of properties which correlate strongly with $\hat{PC}_0$: (ΔM_i,S,T, $f_{R_{sub}}$,x_{off},$\sum\lambda$, $\lambda_{1,M}$,$\lambda_{4,M}$) and applied PCA analysis to their intercorrelations. The trends with $\hat{PC}_0$ for these quantities appear as well with the direction $\hat{PC}_{0,\rm subset}$. In this case, however, $\lambda_{0,\rm subset}$ is relatively larger, $\lambda_{0,\rm subset}/\sum\lambda = 0.39$. To help in understanding, we took three groups of properties (1): ΔM_i (except $\Delta M_{\rm WL}$), (2): the mass scatter measures $\sum\lambda, \lambda_{1,M}, \lambda_{4,M}$, and (3): T,$f_{R_{Sub}}$,x_{off}, S, $\Delta M_{\rm WL}$. The properties in (1) and (2) have large same sign correlations with $\hat{PC}_0$. For (3), sphericity S and average weak lensing mass offset $\Delta M_{\rm WL}$ have this sign correlation as well, while T, $f_{R_{Sub}}$,x_{off} have the opposite sign. These three groups (roughly) can be seen in correlations with $\hat{PC}_{1,\rm subset}$ (0.17 of the sum of eigenvalues), but in this case the relative behavior between properties in (2) and (3) reverses (i.e. increased mass scatter now has the opposite correlation with $\hat{PC}_1$ as increased sphericity does), and changes in (1) all have correlations < 0.07 with $\hat{PC}_{1,\rm subset}$. (Note that the general orthogonality of the $\hat{PC}_i$ means relations between properties, i.e. relative sizes and signs of correlations, do have to change from $\hat{PC}_i$ vector to $\hat{PC}_i$ vector.) The correlation strengths change as well, going from $\hat{PC}_0$ to $\hat{PC}_1$, increasing for (2) and decreasing (below 0.4) for (3). Considering the trends in broad brush, for a given cluster, large measured average (over

[21] We thank E. Rasia for discussions about this.

lines of sight) mass offsets from true mass, aside from weak lensing, seem to tend to come with high sphericity and large mass measurement scatters, and low triaxiality, $f_{R_{sub}}, x_{off}$. That is, when a cluster's mass offsets are very large, there is a tendency for the vector of all its properties to be lying far along $\hat{PC}_{0,\rm subset}$, implying trends for the other properties. When average mass offsets (besides $\Delta M_{\rm WL}$) are small, it is not clear whether a given cluster's variations are lying along $\hat{PC}_{0,\rm subset}$ or $\hat{PC}_{1,\rm subset}$ or some other direction. As the relation between large sphericity (and small triaxiality, $f_{R_{sub}}, x_{off}$), i.e., (3), and the size of mass measurement scatters, i.e., (2), reverses between these two PCA vectors, small mass offsets makes it difficult to estimate the relation between them (i.e., between (2) and (3)).

Continuing with the full set of 24 properties, and considering correlations with $\hat{PC}_1$, the large sphericity/small triaxiality, (relatively) small richness in biggest subgroup, (relatively) small distance of largest subgroup from center and small offset of average galaxy positions with central galaxy position relation trends are also seen, but more weakly. Fluctuations in the direction of $\hat{PC}_1$ have an increase in $|\hat{PC}_{0,M} \cdot \hat{PC}_{0,M,minsq}|$ tied to a decrease in overall mass scatter ($\sum\lambda, \prod\lambda, \lambda_{1,M}, \lambda_{4,M}$) and a decrease in mass in nearby large halos $M_{\rm sphere}$. This last perhaps indicates that the alignment of $\hat{PC}_{0,M}$ is better, and the mass scatter smaller, when the cluster is not in a supercluster. Low concentration and relative distance of largest subgroup from the cluster center tend to happen more often if major mergers are more to the past, for changes along $\hat{PC}_2$. The fraction of mass in the filament and mass planes seem to change together for changes along $\hat{PC}_3$, along with the amount of mass in nearby large halos. Again, these last 3 properties can be studied alone via PCA. In this case the associated $\lambda_{0,\rm subset}/\sum\lambda = 0.65$. Note this is a different subset of PCA vectors than considered earlier, and corresponds to all three quantities, normalized by covariance, changing by about the same amount with the same sign. This may imply that clusters which are in a richer environment, that is, with more nearby halos, may have the mass around them distributed in a more planar shape.

We experimented with a larger set of properties than shown here, including for example the quantities shown in the first column of Fig. 4.9 for each cluster, i.e. the correlations with projections on $\hat{PC}_{0,M}$ and physical directions. In this case the correlations with $\hat{PC}_0$ for the other quantities remained essentially as shown in the top line of Fig. 4.12 but the $\hat{PC}_{0,M}$-long axis projections and the $\hat{PC}_{0,M}$-direction of largest subgroup projections had large correlations with $\hat{PC}_0$ in the same sense as T, cluster triaxiality.

4.5 An ensemble of clusters

The previous sections considered cluster directional mass scatters and variations in properties, cluster to cluster. One can also consider the joint ensemble of mass measurements of all the simulated clusters and all their lines of sight, for all five methods. A comparison is interesting between the PCA vectors of the individual clusters, for many lines of sight, and those for all the clusters together.

	$M_{N_{\rm red}}/M_{\rm true}$	$M_{N_{\rm ph}}/M_{\rm true}$	$M_{\rm SZ}/M_{\rm true}$	$M_{\rm Vel}/M_{\rm true}$	$M_{\rm WL}/M_{\rm true}$
$M_{N_{\rm red}}/M_{\rm true}$	0.18 (0.08)	0.06 (0.02)	0.05 (0.04)	0.04 (0.03)	0.04 (0.03)
$M_{N_{\rm ph}}/M_{\rm true}$	0.06 (0.02)	0.04 (0.02)	0.02 (0.01)	0.02 (0.01)	0.02 (0.01)
$M_{\rm SZ}/M_{\rm true}$	0.05 (0.04)	0.02 (0.01)	0.09 (0.07)	0.04 (0.02)	0.04 (0.01)
$M_{\rm Vel}/M_{\rm true}$	0.04 (0.03)	0.02 (0.01)	0.04 (0.02)	0.24 (0.20)	0.05 (0.02)
$M_{\rm WL}/M_{\rm true}$	0.04 (0.03)	0.02 (0.01)	0.04 (0.01)	0.05 (0.02)	0.11 (0.05)

Table 4.4: Covariance matrix for full set of measurements $\boldsymbol{M}_{\rm obs}/M_{\rm true}$, for all clusters, and, in parentheses, the average of the individual cluster covariances in Fig. 4.4. The median values for the the individual cluster covariances tend to be smaller than the average values. The covariances for the full sample tend to be larger than the averages cluster to cluster.

4.5.1 Trends for all clusters considered together

We take the union of the estimated masses of all clusters and all lines of sight (aside from those discarded as discussed in §2) and repeat the analysis of §3. Now $\boldsymbol{M}_{\rm obs}/M_{\rm true} = \boldsymbol{M}_{\rm est}/M_{\rm true} - \langle \boldsymbol{M}_{\rm est}/M_{\rm true}\rangle$. The average $\langle \boldsymbol{M}_{\rm est}/M_{\rm true}\rangle$ is over all clusters and lines of sight, and for our case is within a few percent of 1. The resulting covariance matrix for these mass scatters is shown in Table 4.4. The covariances for the combined sample are larger than the averages for individual clusters, the latter are shown in Table 4.4 in parentheses for comparison, and were plotted individually in Fig. 4.5. The increased scatter is not unexpected as it is a combination of scatters from objects which are all themselves scattered around different central values. The corresponding PCA eigenvalues are $\lambda_{i,M,total}$=(0.31, 0.18, 0.094, 0.061, 0.022). The direction of largest scatter has $\lambda_{0,M,total}/\sum\lambda$ ∼0.47, compared to the average of 0.66 for individual clusters shown in Fig. 4.6. The total mass scatter variance $\sum\lambda = 0.67$, which is relatively high compared to the average for individual clusters; the product $\prod\lambda$ is also relatively larger (7×10^{-6}), as to be expected from the increased covariances in Table 4.4. [22] The directions of largest scatters are similar to those for the clusters considered separately (Table 4.2), although $\hat{PC}_{4,M,total}$ has a much smaller SZ component than $\hat{PC}_{4,M,minsq}$. The correlations with $\hat{PC}_{0,M,total}$ of the projections of the different mass observables ($M_{N_{\rm red}}$, $M_{N_{\rm ph}}$, $M_{\rm SZ}$, $M_{\rm Vel}$, $M_{\rm WL}$) are (0.69, 0.57, 0.57, 0.79, 0.57), similar to the median of their individual cluster counterparts, (0.69, 0.51, 0.48, 0.87, 0.47), shown in Fig. 4.8. The correlations are fairly large for the other $\hat{PC}_i$ components, but these by definition contribute less to the total mass scatter. $\hat{PC}_{0,M,total}$ and $\Delta\boldsymbol{M}$ are 23° apart, similar to their counterparts for the individual clusters. Again, just as for individual clusters, the closer one is to the long axis of the cluster, the larger the fraction of scatter due to $\hat{PC}_{0,M,total}$ (∼0.4 correlated). The next leading correlations of $\hat{PC}_{0,M,total}$ are with the position of the largest subgroup and the direction perpendicular to the cluster's dominant

[22] For the 70 clusters with mass $\geq 2\times10^{14}h^{-1}M_\odot$, the total scatter $\sum\lambda$ goes down (to 0.44 from 0.67 for the sample with $M \geq 10^{14}h^{-1}M_\odot$), and the direction of the $\hat{PC}_{0,M,total}$ slightly rotates as seen in Table 4.2. The fraction of variance in $\lambda_{0,M}$ increases, i.e. the direction of the largest scatter has more of the scatter.

filamentary plane or mass plane. These trends were very close to those found for clusters individually. These relations are still however based on the estimated mass as a function of true mass, and thus not immediately applicable to observational samples, as we now discuss.

4.5.2 Future extensions to observational samples

One can also consider using some variant of our PCA analysis for an observational sample, which would have some range of true cluster masses and some observations, as we do in our box. However, our implementation of PCA doesn't directly carry over, and our measurement sample in hand is not appropriate. We discuss these limitations and possible ways forward here.

Observations are concerned with $M_{\rm true}$ as a function of estimated mass, $M_{\rm true}(M_{\rm est})$. An observer does not have $M_{\rm true}$. We have instead been calculating $M_{\rm est}(M_{\rm true})$ and in addition dividing by $M_{\rm true}$. Applying PCA in a way useful to observations (so that one can take 5 methods to measure mass of one cluster and compare to the PCA vectors calculated in simulation) requires PCA vectors calculated, from simulation, for a representative range of $M_{\rm est}$ and $M_{\rm true}$, and a proxy for the unobservable $M_{\rm true}$.[23] As a proxy for $M_{\rm true}$, one possibility is the likelihood mass. This would come from simulations, which are already required to calibrate covariances and offsets. Another possible mass proxy uses the principal component vectors directly, in principle encoding similar information. That is, one has from the definition of PCA vectors,

$$\frac{\boldsymbol{M}^\alpha_{\rm obs}}{M_{\rm true}} = \frac{\boldsymbol{M}^\alpha_{\rm est}}{M_{\rm true}} - \left\langle \frac{\boldsymbol{M}_{\rm est}}{M_{\rm true}} \right\rangle = \sum_i a_i^\alpha \hat{PC}_{i,M} \ . \tag{4.5}$$

The quantities aside from $M_{\rm true}$ are either measured , e.g., $\boldsymbol{M}^\alpha_{\rm est}$, or calculated from simulations, e.g., $\langle \boldsymbol{M}_{\rm est}/M_{\rm true}\rangle, \hat{PC}_{i,M}$. In particular, we have

$$\hat{PC}_{4,M,total} \cdot \left(\frac{\boldsymbol{M}^\alpha_{\rm est}}{M_{\rm true}} - \left\langle \frac{\boldsymbol{M}_{\rm est}}{M_{\rm true}} \right\rangle \right) = a_4^\alpha \tag{4.6}$$

but the variance of a_4 is given by $\lambda_{4,M,total}$. If $\lambda_{4,M,total}$ is very small then we can try the

[23] Using no proxy for $M_{\rm true}$, i.e. doing PCA on $M_{\rm est}$ alone, differently weights the scatter of high and low mass clusters. In our sample, caveats below, most of the scatter then corresponds to all mass estimates increasing or decreasing together in equal amounts. Projections on this combination of mass scatters are weakly correlated with observations along the long axis of the cluster, and less correlated with other directions.

approximation $a_4 \sim 0$, so that projecting on $\hat{PC}_{4,M,total}$ gives the approximation[24]

$$M_4 \sim \frac{\hat{PC}_{4,M,total} \cdot \boldsymbol{M}^{\alpha}_{\rm est}}{\hat{PC}_{4,M,total} \cdot \langle \frac{\boldsymbol{M}_{\rm est}}{M_{\rm true}} \rangle} \ . \tag{4.7}$$

The general use of this approach depends upon the size of $\lambda_{4,M,total}$ for the system; the smaller $\lambda_{4,M,total}$ is, the better it appears this approximation should work. As there tend to be some minus signs in $\hat{PC}_4$, some catastrophic failures will occur where $M_4 \ll M_{\rm est,i}$, for all i.

However, the relevance of testing these possible $M_{\rm true}$ proxies on our sample seems limited. In particular, the $P(M_{\rm est}|M_{\rm true})$ for our sample (all $M \geq 10^{14}h^{-1}M_{\odot}$ halos observed along ~ 96 lines of sight each) is not representative of any expected observed sample, nor is our $P(M_{\rm true})$, which is required for likelihoods. Observing our few high mass clusters along many lines of sight is not a good approximation to observing many clusters along one line of sight: the few high mass clusters observed along many lines of sight in particular do not well sample the realistic population of high mass clusters. There are no clusters appearing fewer than ~ 96 times, in particular, rare high mass clusters which would be expected from the number of lower mass clusters "present", are missing. Halos with the same $M_{\rm est}$ (the only observable) but a lower $M_{\rm true}$ will also occur in an observational sample, and might contribute differently to the scatter as well. It would also be important to include the neglected, in our simulation, line of sight larger scale scatter for SZ and weak lensing and the systematics mentioned above. These would be very interesting directions to pursue in future work.

In summary, in this section we considered all the clusters in the box, along all lines of sight, to see how cluster-to-cluster variation altered mass scatter relations found in earlier sections for individual clusters; the trends remained but changed in strength. In particular, the dominant mass scatter combination, similar in form to that for many of the individual clusters, still seems to be more prevalent when looking down the long axis of the cluster or perpendicular to the mass or filament plane of the cluster. In the second subsection, we mentioned two possible methods for extending our analysis which do not require prior knowledge of $M_{\rm true}$, replacing it with the likelihood mass or a mass derived from $\hat{PC}_4$. These would be interesting to apply to an observational sample, but would need a very closely matched simulation. It would be interesting to see if the resulting PCA vectors and projections on them by estimated mass measurement methods have correlations with cluster orientation or perhaps $M_{\rm proxy}/M_{\rm true}$.

[24] An extreme and unphysical limit of this case would be if one measurement method had tiny scatter and no correlation with the other measurement methods. In this case $\hat{PC}_{4,M,total}$ would be proportional to a measurement via this one method, and the last equation would basically give that the estimated mass in this method is the true mass, up to any overall biases that might exist, an unbiased mass estimator would make the denominator 1.

4.6 Outliers

We have focussed on general trends above, but not all clusters (or all lines of sight) fell on the general trends. We searched for properties of outliers or tails in the distributions of the various quantities related to $\lambda_{i,M}$, outliers in average cluster measured mass vs. true cluster mass, clusters with different maximum or minimum covariance mass measurement method pairs than the majority of clusters, and clusters where $\hat{PC}_{0,M}$ had at least one opposite sign coefficient with absolute value ≥ 0.1 (i.e. largest direction of scatter not corresponding to all mass scatters increasing together, mentioned earlier).

The various outliers did not seem to follow any pattern. Some outliers were common to a cluster, e.g. sometimes a large $\lambda_{4,M}$ outlier occurred with a large $\prod \lambda$, as might be expected, as $\lambda_{4,M}$ is the smallest of the $\lambda_{i,M}$. Some of the clusters which had $\hat{PC}_{0,M}$ not aligned with the most likely $\hat{PC}_{0,M,minsq}$ had much larger contributions to mass scatter from Compton decrement than the average cluster, often due to close massive halos, and $\lambda_{0,M}/\sum \lambda$ tending to be smaller than for the usual cluster. The clusters having different correlations of lines-of-sight properties with mass measurement methods don't seem to have a clear relation to the outliers in mass scatter properties.

4.7 Disentangling correlated scatter in cluster mass measurements: Summary and Discussion

The scatters between estimated and true cluster masses, for different observational methods, are often correlated. Understanding these correlations is becoming more and more important as reliance on multiwavelength measurements increases. For instance, correlations and covariances in scatters affect both error estimates in multiple measurements of individual clusters and produce a bias in measurements of stacked objects (Rykoff et al. 2008; Stanek et al. 2010; White et al. 2010; Angulo et al. 2012), see these papers for detailed discussion. (Using the full covariance matrices has been done in some cluster analyses, e.g. by Rozo et al. (2009); Mantz et al. (2010); Benson et al. (2013).) We characterized the scatter and correlations of clusters in two ways.

We started by considering clusters individually, to identify mass scatter properties due to line of sight effects, for 243 clusters in an N-body simulation, each along ~ 96 lines of sight. We used five observational mass proxies: red galaxy richness, phase space galaxy richness, Sunyaev-Zel'dovich flux, velocity dispersions and weak lensing. It would also be very interesting to include X-ray observation as well, but our attempt at a proxy, based on assigning fractional X-ray flux to cluster galaxy subgroups, was not illuminating. These are employed to find cluster masses in current and upcoming large scale cluster surveys.

For each cluster, we characterized the "shape" and "volume" of the mass scatters of $M_{\rm est}$ calculated as a function of $M_{\rm true}$, using PCA, or Principal Component Analysis, to obtain a set of non-covariant measurements. Most clusters had one combination of observational

mass scatters contributing the majority of the mass scatter, and this combination was similar for many of the clusters, i.e. they had a similar largest principal component $\hat{PC}_{0,M}$. This scatter combination was a larger fraction of the total line of sight mass scatter when the cluster was observed along the long axis of the cluster. Weaker relations with observations along other cluster intrinsic and environmental axes were seen. Identifying the long axis of course requires the clusters to have non-spherical shapes. In our case the cluster member dark matter particles were determined using the FoF finder with linking length $b = 0.168$.

Individual cluster mass scatter properties due to line of sight effects were then compared to several intrinsic and environmental cluster properties, including triaxiality, planarity of filament or halo mass in the immediate neighborhood of the cluster and relative richness of largest galaxy subgroup within the cluster. For example, pairwise correlations, and their combined effects using PCA, showed that clusters with average mass measurements (over lines of sight) which are large tend to also have large mass scatter around their average, relatively high sphericity and small triaxiality, richness in the largest subgroup, and offset of the galaxy position average from the cluster center. Relations were also seen for other quantities such as concentration, recent major merger time and fraction of halo mass near the cluster within a 3 $h^{-1}Mpc$ plane.

Finally, instead of considering each cluster individually, we considered the sample of all clusters and all lines of sight together, and found that most of the trends for the analysis of $\boldsymbol{M}_{\rm est}/M_{\rm true}$ remained, albeit at different strengths. The projection on the direction of largest scatter was more weakly correlated with the observation angle relative to the cluster long axis.

It is interesting to think about applying these methods directly to observation. One would need more information, in particular estimates of $M_{\rm true}(M_{\rm est})$, rather than the opposite which we have here. This requires calibrations from simulations which better sample an expected observational sample at the high mass end, and which also include estimated masses from lower mass halos (as well as faithfully reproducing the observational systematics and selection function). Such a simulation would provide correlations and covariances and predicted likelihood masses $M_{\rm like}$ (and a variant, M_4 considered above, based on a narrow direction of scatter in our sample). PCA could then be applied to $M_{\rm est}/M_{\rm like}$ or $M_{\rm est}/M_4$, rather than $M_{\rm est}/M_{\rm true}$ as we did here. It would be interesting to see if these PCA vectors also had relations to cluster orientation such as we found, or perhaps other quantities such as $M_{\rm like}/M_{\rm true}$. They might also give some idea of which follow up mass measurement methods would together provide the most constraining power. One could for example identify the measurement method with potentially the least covariance with measurements already in hand. More generally one could design a combination of measurement methods with smaller covariant scatter (and hopefully smaller scatter as well) using calculated PCA vectors as a guide, if the simulations are faithful enough. Efforts to accurately capture the systematics and selection function of observational surveys with numerical simulations is a major challenge. Another technical issue is to improve estimates of the correlations and covariances, so that sets of inconsistent measurements can be more easily recognized. It would be very

interesting to do such analyses on a larger box, and/or with other measurement methods.

Bibliography

Abell, G. O. 1958, ApJS, 3, 211
Allen, S. W., Evrard, A. E., & Mantz, A. B. 2011, ARA&A, 49, 409
Allen, S. W., Rapetti, D. A., Schmidt, R. W., et al. 2008, MNRAS, 383, 879
Altay, G., Colberg, J. M., & Croft, R. A. C. 2006, MNRAS, 370, 1422
Anderson, L., Aubourg, E., Bailey, S., et al. 2013, ArXiv e-prints, arXiv:1303.4666 [astro-ph.CO]
Angulo, R. E., Springel, V., White, S. D. M., et al. 2012, MNRAS, 426, 2046
Aragón-Calvo, M. A., Jones, B. J. T., van de Weygaert, R., & van der Hulst, J. M. 2007a, A&A, 474, 315
Aragon-Calvo, M. A., Shandarin, S. F., & Szalay, A. 2010, ArXiv e-prints, arXiv:1006.4178 [astro-ph.CO]
Aragón-Calvo, M. A., van de Weygaert, R., & Jones, B. J. T. 2010, MNRAS, 408, 2163
Aragón-Calvo, M. A., van de Weygaert, R., Jones, B. J. T., & van der Hulst, J. M. 2007b, ApJ, 655, L5
Bahé, Y. M., McCarthy, I. G., & King, L. J. 2012, MNRAS, 421, 1073
Bailin, J., & Steinmetz, M. 2005, ApJ, 627, 647
Balaguera-Antolínez, A., Sánchez, A. G., Böhringer, H., et al. 2011, MNRAS, 413, 386
Bardeen, J. M., Bond, J. R., Kaiser, N., & Szalay, A. S. 1986, ApJ, 304, 15
Barrow, J. D., Bhavsar, S. P., & Sonoda, D. H. 1985, MNRAS, 216, 17
Basilakos, S., Plionis, M., Yepes, G., Gottlöber, S., & Turchaninov, V. 2006, MNRAS, 365, 539
Battaglia, N., Bond, J. R., Pfrommer, C., & Sievers, J. L. 2012, ApJ, 758, 74
Becker, M. R., & Kravtsov, A. V. 2011, ApJ, 740, 25
Benson, B. A., de Haan, T., Dudley, J. P., et al. 2013, ApJ, 763, 147
Betancort-Rijo, J. E., & Trujillo, I. 2009, ArXiv e-prints, arXiv:0912.1051 [astro-ph.CO]
Bharadwaj, S. 1996, ApJ, 472, 1
Bharadwaj, S., Bhavsar, S. P., & Sheth, J. V. 2004, ApJ, 606, 25
Bharadwaj, S., Sahni, V., Sathyaprakash, B. S., Shandarin, S. F., & Yess, C. 2000, ApJ, 528, 21
Biesiadzinski, T., McMahon, J., Miller, C. J., Nord, B., & Shaw, L. 2012, ApJ, 757, 1
Binney, J., & Tremaine, S. 1987, Galactic dynamics (Princeton University Press)
Biviano, A., Murante, G., Borgani, S., et al. 2006, A&A, 456, 23

Blake, C., Kazin, E. A., Beutler, F., et al. 2011, MNRAS, 418, 1707
Bond, J. R., Cole, S., Efstathiou, G., & Kaiser, N. 1991, ApJ, 379, 440
Bond, J. R., Kofman, L., & Pogosyan, D. 1996, Nature, 380, 603
Bond, N. A., Strauss, M. A., & Cen, R. 2010a, MNRAS, 406, 1609
—. 2010b, MNRAS, 409, 156
Borgani, S. 2008, in Lecture Notes in Physics, Berlin Springer Verlag, Vol. 740, A Pan-Chromatic View of Clusters of Galaxies and the Large-Scale Structure, ed. M. Plionis, O. López-Cruz, & D. Hughes, 287
Bouchet, F. R., Colombi, S., Hivon, E., & Juszkiewicz, R. 1995, A&A, 296, 575
Bryan, G. L., & Norman, M. L. 1998, ApJ, 495, 80
Buchert, T. 1989, A&A, 223, 9
Carlson, J., White, M., & Padmanabhan, N. 2009, Phys. Rev. D, 80, 043531
Ceccarelli, L., Paz, D. J., Padilla, N., & Lambas, D. G. 2011, MNRAS, 412, 1778
Cen, R. 1997, ApJ, 485, 39
Cen, R., & Ostriker, J. P. 1999, ApJ, 514, 1
Chambers, S. W., Melott, A. L., & Miller, C. J. 2000, ApJ, 544, 104
Choi, E., Bond, N. A., Strauss, M. A., et al. 2010, MNRAS, 406, 320
Cohn, J. D. 2012, MNRAS, 419, 1017
Cohn, J. D., Evrard, A. E., White, M., Croton, D., & Ellingson, E. 2007, MNRAS, 382, 1738
Cohn, J. D., & White, M. 2009, MNRAS, 393, 393
Colberg, J. M. 2007, MNRAS, 375, 337
Colberg, J. M., Krughoff, K. S., & Connolly, A. J. 2005, MNRAS, 359, 272
Colberg, J. M., White, S. D. M., Jenkins, A., & Pearce, F. R. 1999, MNRAS, 308, 593
Colombi, S., Pogosyan, D., & Souradeep, T. 2000, Physical Review Letters, 85, 5515
Conroy, C., & Gunn, J. E. 2010, ApJ, 712, 833
Conroy, C., Gunn, J. E., & White, M. 2009, ApJ, 699, 486
Conroy, C., Wechsler, R. H., & Kravtsov, A. V. 2006, ApJ, 647, 201
Conroy, C., White, M., & Gunn, J. E. 2010, ApJ, 708, 58
Costa-Duarte, M. V., Sodré, Jr., L., & Durret, F. 2011, MNRAS, 411, 1716
Crocce, M., & Scoccimarro, R. 2008, Phys. Rev. D, 77, 023533
Cuesta, A. J., Prada, F., Klypin, A., & Moles, M. 2008, MNRAS, 389, 385
Dalton, G. B., Efstathiou, G., Maddox, S. J., & Sutherland, W. J. 1992, ApJ, 390, L1
Davis, M., Efstathiou, G., Frenk, C. S., & White, S. D. M. 1985, ApJ, 292, 371
Dawson, K. S., Schlegel, D. J., Ahn, C. P., et al. 2013, AJ, 145, 10
de Putter, R., & White, M. 2005, New A, 10, 676
de Simone, A., Maggiore, M., & Riotto, A. 2011, MNRAS, 412, 2587
Dekel, A., Birnboim, Y., Engel, G., et al. 2009, Nature, 457, 451
den Hartog, R., & Katgert, P. 1996, MNRAS, 279, 349
Diaferio, A., & Geller, M. J. 1997, ApJ, 481, 633
Diemand, J., Kuhlen, M., & Madau, P. 2006, ApJ, 649, 1
Dietrich, J. P., Werner, N., Clowe, D., et al. 2012, Nature, 487, 202

Dolag, K., Meneghetti, M., Moscardini, L., Rasia, E., & Bonaldi, A. 2006, MNRAS, 370, 656
Doroshkevich, A. G., Zel'dovich, Y. B., & Syunyaev, R. A. 1978, Soviet Ast., 22, 523
Dressler, A., & Shectman, S. A. 1988, AJ, 95, 985
Einasto, J., Klypin, A. A., Saar, E., & Shandarin, S. F. 1984, MNRAS, 206, 529
Einasto, M., Liivamägi, L. J., Saar, E., et al. 2011, A&A, 535, A36
Einasto, M., Liivamägi, L. J., Tempel, E., et al. 2012, A&A, 542, A36
Eisenstein, D. J., & Hu, W. 1998, ApJ, 496, 605
Eisenstein, D. J., Seo, H.-J., Sirko, E., & Spergel, D. N. 2007a, ApJ, 664, 675
Eisenstein, D. J., Seo, H.-J., & White, M. 2007b, ApJ, 664, 660
Eisenstein, D. J., Zehavi, I., Hogg, D. W., et al. 2005, ApJ, 633, 560
Erickson, B. M. S., Cunha, C. E., & Evrard, A. E. 2011, Phys. Rev. D, 84, 103506
Estrada, J., Sefusatti, E., & Frieman, J. A. 2009, ApJ, 692, 265
Ettori, S. 2003, MNRAS, 344, L13
Ettori, S., Morandi, A., Tozzi, P., et al. 2009, A&A, 501, 61
Fahlman, G., Kaiser, N., Squires, G., & Woods, D. 1994, ApJ, 437, 56
Faltenbacher, A., Allgood, B., Gottlöber, S., Yepes, G., & Hoffman, Y. 2005, MNRAS, 362, 1099
Faltenbacher, A., Gottlöber, S., Kerscher, M., & Müller, V. 2002, A&A, 395, 1
Faltenbacher, A., Li, C., Mao, S., et al. 2007, ApJ, 662, L71
Feix, M., Xu, D., Shan, H., et al. 2008, ApJ, 682, 711
Feroz, F., & Hobson, M. P. 2012, MNRAS, 420, 596
Forero-Romero, J. E., Hoffman, Y., Gottlöber, S., Klypin, A., & Yepes, G. 2009, MNRAS, 396, 1815
Frieman, J. A., Turner, M. S., & Huterer, D. 2008, ARA&A, 46, 385
Gal, R. R., Lemaux, B. C., Lubin, L. M., Kocevski, D., & Squires, G. K. 2008, ApJ, 684, 933
Gay, C., Pichon, C., Le Borgne, D., et al. 2010, MNRAS, 404, 1801
Genovese, C. R., Perone-Pacifico, M., Verdinelli, I., & Wasserman, L. 2010, ArXiv e-prints, arXiv:1003.5536 [math.ST]
Gerke, B. F., Newman, J. A., Davis, M., et al. 2005, ApJ, 625, 6
González, R. E., & Padilla, N. D. 2010, MNRAS, 407, 1449
Green, J., Schechter, P., Baltay, C., et al. 2012, ArXiv e-prints, arXiv:1208.4012 [astro-ph.IM]
Gunn, J. E., & Gott, III, J. R. 1972, ApJ, 176, 1
Hahn, O., Carollo, C. M., Porciani, C., & Dekel, A. 2007a, MNRAS, 381, 41
Hahn, O., Porciani, C., Carollo, C. M., & Dekel, A. 2007b, MNRAS, 375, 489
Hahn, O., Teyssier, R., & Carollo, C. M. 2010, MNRAS, 405, 274
Hallman, E. J., O'Shea, B. W., Burns, J. O., et al. 2007, ApJ, 671, 27
Hansen, S. M., McKay, T. A., Wechsler, R. H., et al. 2005, ApJ, 633, 122
Hill, G. J., MacQueen, P. J., Palunas, P., et al. 2006, New A Rev., 50, 378
Hivon, E., Bouchet, F. R., Colombi, S., & Juszkiewicz, R. 1995, A&A, 298, 643

Hockney, R. W., & Eastwood, J. W. 1988, Computer simulation using particles
Hoekstra, H. 2001, A&A, 370, 743
—. 2007, MNRAS, 379, 317
Hoekstra, H., Hartlap, J., Hilbert, S., & van Uitert, E. 2011, MNRAS, 412, 2095
Holder, G. P., McCarthy, I. G., & Babul, A. 2007, MNRAS, 382, 1697
Hopkins, P. F., Bahcall, N. A., & Bode, P. 2005, ApJ, 618, 1
Hu, W., & Kravtsov, A. V. 2003, ApJ, 584, 702
Huff, E., Schulz, A. E., White, M., Schlegel, D. J., & Warren, M. S. 2007, Astroparticle Physics, 26, 351
Jasche, J., & Wandelt, B. D. 2013, MNRAS, 432, 894
Jeeson-Daniel, A., Dalla Vecchia, C., Haas, M. R., & Schaye, J. 2011, MNRAS, 415, L69
Jenkins, A., Frenk, C. S., White, S. D. M., et al. 2001, MNRAS, 321, 372
Jing, Y. P., & Suto, Y. 2002, ApJ, 574, 538
Jolliffe, I. T. 2002, Springer Series in Statistics: Principal Component Analysis, 2nd Edition
Jones, B. J. T., van de Weygaert, R., & Aragón-Calvo, M. A. 2010, MNRAS, 408, 897
Kaiser, N. 1987, MNRAS, 227, 1
—. 1995, ApJ, 439, L1
Kartaltepe, J. S., Ebeling, H., Ma, C. J., & Donovan, D. 2008, MNRAS, 389, 1240
Kasun, S. F., & Evrard, A. E. 2005, ApJ, 629, 781
Kereš, D., Katz, N., Fardal, M., Davé, R., & Weinberg, D. H. 2009, MNRAS, 395, 160
Kereš, D., Katz, N., Weinberg, D. H., & Davé, R. 2005, MNRAS, 363, 2
Koester, B. P., McKay, T. A., Annis, J., et al. 2007, ApJ, 660, 221
Kravtsov, A. V., & Borgani, S. 2012, ARA&A, 50, 353
Laureijs, R., Amiaux, J., Arduini, S., et al. 2011, ArXiv e-prints, arXiv:1110.3193 [astro-ph.CO]
Lee, J. 2004, ApJ, 614, L1
Lee, J., & Evrard, A. E. 2007, ApJ, 657, 30
Lee, J., & Springel, V. 2010, J. Cosmology Astropart. Phys., 5, 31
Lee, J., Springel, V., Pen, U.-L., & Lemson, G. 2008, MNRAS, 389, 1266
Lubin, L. M., Gal, R. R., Lemaux, B. C., Kocevski, D. D., & Squires, G. K. 2009, AJ, 137, 4867
Lukić, Z., Heitmann, K., Habib, S., Bashinsky, S., & Ricker, P. M. 2007, ApJ, 671, 1160
Lukić, Z., Reed, D., Habib, S., & Heitmann, K. 2009, ApJ, 692, 217
Lumsden, S. L., Nichol, R. C., Collins, C. A., & Guzzo, L. 1992, MNRAS, 258, 1
Mana, A., Giannantonio, T., Weller, J., et al. 2013, MNRAS, 434, 684
Mantz, A., Allen, S. W., Ebeling, H., Rapetti, D., & Drlica-Wagner, A. 2010, MNRAS, 406, 1773
Marrone, D. P., Smith, G. P., Okabe, N., et al. 2012, ApJ, 754, 119
Matsubara, T. 2008a, Phys. Rev. D, 78, 083519
—. 2008b, Phys. Rev. D, 77, 063530
Mead, J. M. G., King, L. J., & McCarthy, I. G. 2010, MNRAS, 401, 2257

Mecke, K. R., Buchert, T., & Wagner, H. 1994, A&A, 288, 697
Meiksin, A., White, M., & Peacock, J. A. 1999, MNRAS, 304, 851
Meneghetti, M., Fedeli, C., Pace, F., Gottlöber, S., & Yepes, G. 2010, A&A, 519, A90
Metzler, C. A., White, M., & Loken, C. 2001, ApJ, 547, 560
Moutarde, F., Alimi, J.-M., Bouchet, F. R., Pellat, R., & Ramani, A. 1991, ApJ, 382, 377
Murphy, D. N. A., Eke, V. R., & Frenk, C. S. 2011, MNRAS, 413, 2288
Myers, S. T., Pfrommer, C., Aguirre, J., et al. 2009, in Astronomy, Vol. 2010, astro2010: The Astronomy and Astrophysics Decadal Survey, 218
Navarro, J. F., Frenk, C. S., & White, S. D. M. 1997, ApJ, 490, 493
Noh, Y., & Cohn, J. D. 2011, MNRAS, 413, 301
—. 2012, MNRAS, 426, 1829
Noh, Y., White, M., & Padmanabhan, N. 2009, Phys. Rev. D, 80, 123501
Novikov, D., Colombi, S., & Doré, O. 2006a, MNRAS, 366, 1201
—. 2006b, MNRAS, 366, 1201
Onuora, L. I., & Thomas, P. A. 2000, MNRAS, 319, 614
Padmanabhan, N., & White, M. 2009, Phys. Rev. D, 80, 063508
Padmanabhan, N., White, M., & Cohn, J. D. 2009, Phys. Rev. D, 79, 063523
Pandey, B., & Bharadwaj, S. 2006, MNRAS, 372, 827
Paz, D. J., Sgró, M. A., Merchán, M., & Padilla, N. 2011, MNRAS, 414, 2029
Paz, D. J., Stasyszyn, F., & Padilla, N. D. 2008, MNRAS, 389, 1127
Peebles, P. J. E., & Yu, J. T. 1970, ApJ, 162, 815
Percival, W. J., & Schäfer, B. M. 2008, MNRAS, 385, L78
Pereira, M. J., Bryan, G. L., & Gill, S. P. D. 2008, ApJ, 672, 825
Perlmutter, S., Aldering, G., Goldhaber, G., et al. 1999, ApJ, 517, 565
Peterson, J. B., Bandura, K., & Pen, U. L. 2006, ArXiv Astrophysics e-prints, arXiv:astro-ph/0606104
Pimbblet, K. A. 2005a, MNRAS, 358, 256
—. 2005b, PASA, 22, 136
Pimbblet, K. A., Drinkwater, M. J., & Hawkrigg, M. C. 2004, MNRAS, 354, L61
Planck Collaboration, Ade, P. A. R., Aghanim, N., et al. 2013a, ArXiv e-prints, arXiv:1303.5076 [astro-ph.CO]
—. 2013b, A&A, 550, A134
Plionis, M., Benoist, C., Maurogordato, S., Ferrari, C., & Basilakos, S. 2003, ApJ, 594, 144
Poggianti, B. M., De Lucia, G., Varela, J., et al. 2010, MNRAS, 405, 995
Pogosyan, D., Pichon, C., Gay, C., et al. 2009, MNRAS, 396, 635
Porter, S. C., & Raychaudhury, S. 2005, MNRAS, 364, 1387
—. 2007, MNRAS, 375, 1409
Porter, S. C., Raychaudhury, S., Pimbblet, K. A., & Drinkwater, M. J. 2008, MNRAS, 388, 1152
Press, W. H., & Schechter, P. 1974, ApJ, 187, 425
Ragone-Figueroa, C., & Plionis, M. 2007, MNRAS, 377, 1785

Rasia, E., Meneghetti, M., Martino, R., et al. 2012, New Journal of Physics, 14, 055018
Reblinsky, K., & Bartelmann, M. 1999, A&A, 345, 1
Riess, A. G., Filippenko, A. V., Challis, P., et al. 1998, AJ, 116, 1009
Rozo, E., Rykoff, E., Koester, B., et al. 2011, ApJ, 740, 53
Rozo, E., Rykoff, E. S., Evrard, A., et al. 2009, ApJ, 699, 768
Rykoff, E. S., Evrard, A. E., McKay, T. A., et al. 2008, MNRAS, 387, L28
Sahni, V., Sathyaprakash, B. S., & Shandarin, S. F. 1998, ApJ, 495, L5
Saro, A., Mohr, J. J., Bazin, G., & Dolag, K. 2013, ApJ, 772, 47
Schaap, W. E., & van de Weygaert, R. 2000, A&A, 363, L29
Schäfer, B. M. 2009, International Journal of Modern Physics D, 18, 173
Schmalzing, J. 1998, in Large Scale Structure: Tracks and Traces, ed. V. Mueller, S. Gottloeber, J. P. Muecket, & J. Wambsganss, 195
Schmalzing, J., Buchert, T., Melott, A. L., et al. 1999, ApJ, 526, 568
Seo, H.-J., Siegel, E. R., Eisenstein, D. J., & White, M. 2008, ApJ, 686, 13
Shandarin, S., Habib, S., & Heitmann, K. 2012, Phys. Rev. D, 85, 083005
Shandarin, S. F. 2004, in IAU Colloq. 195: Outskirts of Galaxy Clusters: Intense Life in the Suburbs, ed. A. Diaferio, 45
Shandarin, S. F. 2011, J. Cosmology Astropart. Phys., 5, 15
Shandarin, S. F., Sheth, J. V., & Sahni, V. 2004, MNRAS, 353, 162
Shandarin, S. F., & Zeldovich, I. B. 1983, Comments on Astrophysics, 10, 33
Shaw, L. D., Holder, G. P., & Bode, P. 2008, ApJ, 686, 206
Shen, J., Abel, T., Mo, H. J., & Sheth, R. K. 2006, ApJ, 645, 783
Sheth, J. V., Sahni, V., Shandarin, S. F., & Sathyaprakash, B. S. 2003, MNRAS, 343, 22
Sheth, R. K., & Tormen, G. 1999, MNRAS, 308, 119
Silk, J. 1968, ApJ, 151, 459
Skibba, R. A., & Macciò, A. V. 2011, MNRAS, 416, 2388
Skibba, R. A., & Sheth, R. K. 2009, MNRAS, 392, 1080
Smith, A. G., Hopkins, A. M., Hunstead, R. W., & Pimbblet, K. A. 2012, MNRAS, 422, 25
Song, H., & Lee, J. 2011, ApJ, 736, 27
Sousbie, T. 2011, MNRAS, 414, 350
Sousbie, T., Colombi, S., & Pichon, C. 2009, MNRAS, 393, 457
Sousbie, T., Pichon, C., Colombi, S., Novikov, D., & Pogosyan, D. 2008a, MNRAS, 383, 1655
Sousbie, T., Pichon, C., Courtois, H., Colombi, S., & Novikov, D. 2008b, ApJ, 672, L1
Sousbie, T., Pichon, C., & Kawahara, H. 2011, MNRAS, 414, 384
Splinter, R. J., Melott, A. L., Linn, A. M., Buck, C., & Tinker, J. 1997, ApJ, 479, 632
Springel, V., White, S. D. M., Jenkins, A., et al. 2005, Nature, 435, 629
Stanek, R., Rasia, E., Evrard, A. E., Pearce, F., & Gazzola, L. 2010, ApJ, 715, 1508
Stoica, R. S., Martínez, V. J., Mateu, J., & Saar, E. 2005, A&A, 434, 423
Stoica, R. S., Martínez, V. J., & Saar, E. 2010, A&A, 510, A38
Struble, M. F., & Peebles, P. J. E. 1985, AJ, 90, 582

Sunyaev, R. A., & Zeldovich, I. B. 1980, ARA&A, 18, 537
Sunyaev, R. A., & Zeldovich, Y. B. 1970, Ap&SS, 7, 3
—. 1972, Comments on Astrophysics and Space Physics, 4, 173
Tanaka, M., Finoguenov, A., Kodama, T., et al. 2009, A&A, 505, L9
Taylor, A. N., & Hamilton, A. J. S. 1996, MNRAS, 282, 767
Tinker, J., Kravtsov, A. V., Klypin, A., et al. 2008, ApJ, 688, 709
Tormen, G. 1997, MNRAS, 290, 411
van de Weygaert, R. 2002, ArXiv Astrophysics e-prints, arXiv:astro-ph/0206381
—. 2006, ArXiv Astrophysics e-prints, arXiv:astro-ph/0607539
van de Weygaert, R., & Bertschinger, E. 1996, MNRAS, 281, 84
van de Weygaert, R., & Schaap, W. 2007, ArXiv e-prints, arXiv:0708.1441
van de Weygaert, R., Vegter, G., Platen, E., Eldering, B., & Kruithof, N. 2010, ArXiv e-prints, arXiv:1006.2765 [astro-ph.CO]
van Haarlem, M., & van de Weygaert, R. 1993, ApJ, 418, 544
van Haarlem, M. P., Frenk, C. S., & White, S. D. M. 1997, MNRAS, 287, 817
Vikhlinin, A., Kravtsov, A. V., Burenin, R. A., et al. 2009, ApJ, 692, 1060
Voit, G. M. 2005, Reviews of Modern Physics, 77, 207
Wagner, C., Müller, V., & Steinmetz, M. 2008, A&A, 487, 63
Wang, H., Mo, H. J., Jing, Y. P., et al. 2009, MNRAS, 394, 398
Wang, H., Mo, H. J., Jing, Y. P., Yang, X., & Wang, Y. 2011, MNRAS, 413, 1973
Way, M. J., Gazis, P. R., & Scargle, J. D. 2011, ApJ, 727, 48
Weinberg, D. H., Mortonson, M. J., Eisenstein, D. J., et al. 2012, ArXiv e-prints, arXiv:1201.2434 [astro-ph.CO]
Werner, N., Finoguenov, A., Kaastra, J. S., et al. 2008, A&A, 482, L29
Wetzel, A. R., Cohn, J. D., & White, M. 2009, MNRAS, 395, 1376
Wetzel, A. R., & White, M. 2010, MNRAS, 403, 1072
White, M. 2001, A&A, 367, 27
—. 2002, ApJS, 143, 241
White, M., Cohn, J. D., & Smit, R. 2010, MNRAS, 408, 1818
White, M., Hernquist, L., & Springel, V. 2002, ApJ, 579, 16
White, R. A., Bliton, M., Bhavsar, S. P., et al. 1999, AJ, 118, 2014
White, S. D. M., & Silk, J. 1979, ApJ, 231, 1
Wojtak, R., Łokas, E. L., Mamon, G. A., et al. 2007, A&A, 466, 437
Wray, J. J., Bahcall, N. A., Bode, P., Boettiger, C., & Hopkins, P. F. 2006, ApJ, 652, 907
Wu, Y., Batuski, D. J., & Khalil, A. 2009, ApJ, 707, 1160
Yang, H.-Y. K., Bhattacharya, S., & Ricker, P. M. 2010, ApJ, 725, 1124
Yang, X., Mo, H. J., & van den Bosch, F. C. 2008, ApJ, 676, 248
Zeldovich, I. B., Einasto, J., & Shandarin, S. F. 1982, Nature, 300, 407
Zel'dovich, Y. B. 1970, A&A, 5, 84
Zhang, Y., Yang, X., Faltenbacher, A., et al. 2009, ApJ, 706, 747
Zwicky, F. 1937, ApJ, 86, 217